Effect of non-axisymmetric tokamak plasmas on the coupling performance of ion cyclotron wave antennas

Guillermo Suárez López

München 2020

Effect of non-axisymmetric tokamak plasmas on the coupling performance of ion cyclotron wave antennas

Guillermo Suárez López

Dissertation
an der Fakultät für Physik
der Ludwig–Maximilians–Universität
München

vorgelegt von
Guillermo Suárez López
aus Ourense, Spanien

München, den 20.02.2020

Erstgutachter: Prof. Dr. Hartmut Zohm
Zweitgutachter: Prof. Dr. Gregor Morfill
Tag der mündlichen Prüfung: 18.06.2020

Zusammenfassung

Ionenzyklotronwellen (IC-Wellen, oder häufig *ion cyclotron range of frequencies*, ICRF-Wellen) sind eine weit verbreitete Methode für Plasmaheizung und Stromantrieb, die in experimentellen Fusionsreaktoren mit magnetischem Einschluss wie Tokamaks und Stellaratoren verwendet wird. Das Arbeitsprinzip beruht auf der Anregung der schnellen Mode im magnetisierten Plasma, oder kurz, der schnellen Welle. Dies geschieht durch eine Antenne und bei einer Frequenz nahe der Zyklotronfrequenz[1] einer bestimmten Ionenspezies im Plasmakern, an der die Welle resonant gedämpft wird. Die schnelle Welle ist aufgrund der niedrigen Dichte in der Plasmarandschicht, in der sich die Antenne befindet, häufig evaneszente an der Stelle, an der sie angeregt wird. Aus diesem Grund, muss die Welle erst den Wellen-"cutoff" erreichen, in dem die Plasmadichte hoch genug wird, bevor sie sich regulär ausbreiten kann. Die Menge an ICRF-Leistung, die bei einem gegebenen Strom in den Antennenleitern durch das evaneszente Volumen (Kopplungsregion) gekoppelt werden kann, ist eine Funktion der optischen Eigenschaften dieses Mediums. Diese werden von der Plasmadichte, der Spezieszusammensetzung, dem Magnetfeld, der Wellenfrequenz und dem Antennenstromspektrum charakterisiert.

In einem Tokamak-Plasma, der von grenzverformenden magnetohydrodynamischen (MHD) Instabilitäten wie externe "kink" Moden oder "edge localized" Moden (ELM) betroffen ist, erhält dieser Kopplungsregion eine 3D-Geometrie, wobei die Plasmadichte und das Magnetfeld in jeder Richtung variieren. Gleiches gilt für Fusionsreaktoren deren Einschlussprinzip intrinsisch keine toroidale Symmetrie besitzt, wie zum Beispiel Stellaratoren. Unter diesen Bedingungen wird die Vorhersage der ICRF-Leistungskopplung unsicher, da die meisten experimentellen und numerischen Studien, die bevor der vorliegenden Arbeit durchgeführt wurden, auf 1D-Näherungen des Problems beruhen. In dieser Arbeit wurde eine Reihe von Experimenten und Simulationen durchgeführt, mit dem Ziel eine Brücke zu schlagen, vom dem gut erforschtem Gebiet der ICRF-Kopplung in achsensymmetrischen Konfigurationen, wo die 1D-Näherung häufig gut geeignet ist, zu dem viel weniger verstandenem Problem in der 3D-Geometrie. Die Radiofrequenzeigenschaften der vier im ASDEX Upgrade-Tokamak installierten ICRF-Antennen wurden experimentell durch Plasmaentladungen mit einem von außen angelegten magnetischen Störfeld (MP-Feld) charakterisiert. Dieses ermöglicht das Anlegen einer bekannten, einstellbaren, nicht-achsensymmetrischen externen Störung. Darüber hinaus vermittelt es praktisches Kenntnisse über den Einfluss von MP-Feldern auf die ICRF-Kopplung. Dies ist von besonderer Bedeutung, da diese für die ELM-Kontrolle in Fusionsexperimente der nächsten Generation wie ITER geplant sind, bei denen die ICRF-Leistung zur Heizung des Plasmas verwendet wird. Die starre toroidale Rotation des angelegten MP-Feldes und eine Variation des Spektrums der Poloidalmodenzahl ermöglichen die Untersuchung von: (i) der nicht-achsensymmetrischen Plasmaantwort auf das MP-Feld, (ii) die dadurch hervorgerufene

[1] Oder einer ihrer Harmonischen.

Störung der Plasmaranddichte und (iii) dessen Einfluss auf die ICRF-Kopplung. Plasma- und Radiofrequenzdiagnostiken dienen dazu, die Verformung der Wellen-cutoff mit der Änderung der Antennenkopplungseigenschaften zu korrelieren. Wir stellen fest, dass der Antennenwiderstand durch das resultierende nicht-achsensymmetrische Dichteprofil kohärent modifiziert wird. Ihre Beziehung weicht deutlich von dem ab, was man bei radialen Bewegungen eines achsensymmetrischen Plasmas erwarten würde. Dies zeigt wie bedeutend die 3D-Plasmageometrie für die Kopplung ist. Diese Abweichung wird weiter durch 1D "Full-wave"simulationen bestätigt, welche die Messungen in 3D-Szenarien nicht erklären können, aber sehr gut mit experimentellen Radialabtastungen von achsensymmetrischen Plasmen übereinstimmen. Es wurde ein numerischer Arbeitsablauf entwickelt, mit dem erstmals 3D-MHD-Gleichgewichte, die dazugehörigen 3D-Dichteprofile und 3D-Full-wave-randsimulationen behandelt werden können. Dies wird mithilfe des PARVMEC-Codes, des EMC3-EIRENE-Codes und eines verbesserten 3D-RAPLICASOL-Codes implementiert. Die durchgeführten Simulationen erzeugen korrekt 3D-Dichteprofile, die mit den verfügbaren Messungen übereinstimmen. Diese werden in 3D-Full-wave-RAPLICASOL-Simulationen verwendet, die durch eine Verbesserung des ICRF-Antennenmodells das Problem in realistischer Geometrie behandeln. Die berechnete Änderung der Kopplungsleistung stimmt, im Gegensatz zu den 1D-Simulationen, mit der in MP-Experimenten gemessenen überein.

Daher liefert diese Doktorarbeit den ersten eindeutigen experimentellen und numerischen Beweis für die Relevanz der 3D-Plasmageometrie für die Kopplungsleistung von ICRF-Antennen. Es zeigt zweifelsfrei, dass 1D-Näherungen das gefundene experimentelle Verhalten nicht reproduzieren können, während die neu entwickelten 3D-Simulationen es quantitativ reproduzieren können. Darüber hinaus bietet diese Arbeit eine logische Erklärung der beteiligten Physik und ihrer theoretischen Grundlagen. Es stellt auch ein neuartiges Simulationswerkzeug, das für reaktorrelevanten Plasmaszenarien erfolgreich getestet wurde und effektiv zur Verbesserung der Vorhersagen für zukünftige ICRF-Systeme verwendet werden kann.

Abstract

Ion cyclotron waves (IC waves, or often *ion cyclotron range of frequencies*, ICRF waves) are a widespread method for plasma heating and current-drive used in experimental magnetic confinement fusion reactors, such as tokamaks and stellarators. The working principle relies on the excitation by an antenna of the magnetized plasma fast mode, the fast wave. This is performed at a frequency matching the cyclotron frequency[2] of a given ionic species in the plasma core, such that resonant damping can occur. The fast wave, however, displays evanescence from where it is excited due to the low-density conditions at the plasma edge, where the antenna is often located. It must first reach the cutoff region, where the plasma density becomes high enough, before it starts propagating. The amount of ICRF power that can be coupled through the evanescent volume (*coupling region*) at a given current in the antenna conductors is a function of the optical properties of this medium. These are characterized by plasma density, species composition, magnetic field, wave frequency and the antenna currents' spectrum, determined by their periodicity in toroidal and poloidal directions.

In a tokamak plasma affected by boundary-deforming magnetohydrodynamic (MHD) instabilities, such as external kink modes or edge localized modes (ELM), this coupling region acquires 3D geometry, with varying plasma density and magnetic field in every direction. The same is true for 3D intrinsic machines, such as stellarators. Under these conditions, prediction of ICRF power coupling becomes uncertain, because most experimental and numerical studies performed prior to this work assumed a 1D approximation to the problem. In order to bridge the well-understood knowledge of ICRF coupling in axisymmetric configurations, where a 1D assumption is often well suited, and the much less understood problem in 3D geometry, experiments and simulations have been carried out in this thesis. The radio frequency properties of the four ICRF antennas installed in the ASDEX Upgrade tokamak are experimentally characterized in discharges with an externally applied magnetic perturbation (MP) field. This allows imposing a well known, tunable, non-axisymmetric external perturbation that endows the coupling region with 3D geometry. It furthermore provides practical knowledge of the impact of MP fields on ICRF coupling. This is of special importance, as these are envisaged for ELM control in next-step fusion devices, such as ITER, where ICRF power will be used to externally heat the plasma. Rigid toroidal rotation of the applied MP field and a scan over its poloidal mode number spectrum allow to study: (i) the non-axisymmetric plasma response to the MP field, (ii) the scrape-off layer density perturbation arising from such plasma response and (iii) its impact on ICRF coupling. Plasma and radio frequency diagnostics serve to correlate the wave cutoff layer deformation to the change in antenna coupling characteristics. We find the antenna loading resistance to be coherently modified by the resulting non-axisymmetric density profile. It is also found that their relation clearly diverges from that obtained when an unperturbed plasma,

[2] Or one of its harmonics.

with no MP field, is radially moved away/towards the antenna. This finding highlights the contrasting impact of 3D plasma geometry on antenna performance. Such disagreement is further exposed by 1D full-wave simulations, which cannot account for the measurements in 3D scenarios, but agree very well with experimental radial scans of axisymmetric plasmas. A numerical workflow is devised, which allows for the first time to treat 3D MHD equilibrium, 3D density profile reconstruction and 3D full-wave edge simulations altogether. This is implemented using the PARVMEC code, the EMC3-EIRENE code and an improved 3D RAPLICASOL code. The performed simulations correctly produce 3D density profiles that are in agreement with the available measurements. These are used in 3D full-wave RAPLICASOL simulations, to which an improvement of the ICRF antenna model was performed, thus allowing to treat the problem in realistic curved geometry. The computed change in coupling performance is found to be in agreement with that measured in MP experiments, unlike that obtained with the 1D simulations.

Therefore, the work presented in this Ph.D thesis, offers the first clear experimental and numerical proof of the relevance of 3D plasma geometry on the coupling performance of ICRF antennas. It exposes beyond doubt, that 1D approximations fail to reproduce the found experimental behavior, while the newly developed 3D simulations can quantitatively reproduce it. Furthermore, this work offers a clear explanation of the involved physics, and their theoretical foundation. It also provides a novel numerical scheme that has been successfully benchmarked in reactor-relevant plasma scenarios and can be effectively used to improve predictions for future ICRF systems.

Contents

Motivation for this thesis

Even at the first stages in the development of magnetic confinement nuclear fusion around the 1950s, it was clear that confined ions with very large temperatures ($\geqslant$ 10 keV) would be required in order to attain a significant gain of thermonuclear power from a burning plasma. One of the few methods that exists for direct ionic heating is Ion Cyclotron Resonant Heating, or ICRH[3] for short. At first, the method seems straightforward. An antenna with current-carrying conductors is embedded inside the toroidal machine and fed by a generator to produce a plasma wave (fast wave). This wave oscillates with a precise frequency, which matches the cyclotron frequency of the ions that one desires to heat. Resonant damping occurs at the layer where $\omega_{\text{wave}} = n\omega_{ci}$[4], $\forall n \in \mathbb{N}$. Three main difficulties arise, however, from this method. The first one, is that the fast wave polarization is opposite to that of the gyrating ions (right-hand polarized instead of left-hand), so no fundamental damping can occur. The second one, is the fact that the fast wave is evanescent for low plasma densities, like the ones that exist close to the vessel wall where the antenna is placed. This implies that the wave must be *coupled* (tunneled) through the evanescent layer before propagation in the denser core region can occur. The third one is the simultaneous excitation of a spurious mode (the slow wave) by the antenna. Its electric field has a component aligned to the background magnetic field and tends to accelerate ions towards limiting structures, producing impurities via sputtering.

Despite these difficulties, ICRH soon proved to be an effective tool, and its usage became widespread in many tokamak devices and stellarators. The first problem is usually overcome resorting to special heating scenarios (minority heating, multi-harmonic, etc.). The second and third ones were minor for smaller-than-present carbon-wall machines, where the antenna could be positioned close to the denser plasma region. However, as devices grew larger, confinement time increased, and temperatures rose, plasma loads to the first wall became more acute. This meant that the gap between the outer wall and the separatrix needed to increase in order to better isolate facing materials from heat loads. In turn, this meant a larger gap needed to be tunneled by the fast wave for accessibility to the core, and larger current amplitudes in the antenna conductors have to be excited in order to couple the same amount of ICRH power. At this stage, machines also transitioned from carbon walls, easily sputtered and prone to tritium retention, to metal walls, often tungsten. Impurities produced by the spurious slow wave likewise transitioned from a low-Z character to a high-Z one[5], which meant radiative cooling often led to discharge termination. It is now when the study of antenna near fields and plasma edge - wave

[3] Often also called Ion Cyclotron Range of Frequencies, ICRF, in the literature, in order to stress its functionality for other tasks, such as current-drive and wall-conditioning.

[4] Neglecting Doppler shift.

[5] Z being the atomic number. For carbon impurities with $Z = 6$, radiative cooling via collisions with particle species is much less effective than for high-Z impurities, like W, where a large amount of electronic transitions can be excited.

interactions becomes of great importance. Fundamental theoretical and experimental progress is made in the $\sim$ 1990s - 2010s decades. Solutions to impurity production arise from the better understanding of the underlying physical mechanism driving the sputtering (i.e. slow wave sheath rectification), such that improved antenna designs can be implemented. These include field-aligned antennas, such as the one in Alcator C-mod, and current-compensating antennas, such as the 3-strap antenna in ASDEX Upgrade. The fast wave coupling through a larger gap issue has been addressed by fine-tuning the $k_{\parallel}$ spectrum of antennas, the fundamental study of arc prevention, and SOL gas puff techniques for edge density tailoring. It is in this latter context that this Ph.D. thesis is motivated. It is often the case that this coupling region, usually assumed of 1D-character, i.e., density, temperature and magnetic field variation only exists radially away from the antenna, departs drastically from this behavior. When gas is puffed to increase the edge density, a 3D cloud of neutrals is ionized non-homogeneously, producing anisotropic 3D density profiles. Likewise, plasma instabilities such as external kink modes, edge localized modes, etc., and externally applied magnetic perturbation (MP) 3D fields, produce non-axisymmetric plasma kinetic profiles. In stellarators, the intrinsic non-axisymmetry of the machine makes the coupling region explicitly of 3D nature. It is thus of uttermost importance to develop an understanding of how ICRH coupling is changed under these circumstances.

This thesis addresses experimentally, theoretically and numerically the behavior of ICRH antennas coupling to non-axisymmetric plasmas. Experiments have been carried out in the ASDEX Upgrade tokamak, where the influence of applied 3D MP fields on the radio frequency (RF) characteristics of ICRH antennas has been studied. In particular, the following questions were addressed:

1. How are the radiation impedance and loading resistance of an ICRH antenna modified by non-axisymmetric plasma configurations?

2. Do 1D scaling laws and 1D analytically-derived formulas still hold under these conditions?

3. What is the expected impact on the RF properties of an antenna arising from the conjoint operation of ICRH and MPs in current and future machines?

4. Are 1D antenna codes able to capture the 3D physics, or are 3D simulation tools required in order to reproduce the experimental behavior?

The experimental results are analyzed in detail and further compared to theory-based and empirical scalings. Suitable explanations for the observed behavior are found. Full-wave numerical simulations are carried out in 1D and 3D fashion, and the predictive capabilities of the used tools are assessed.

Overall, this thesis provides a further step in the understanding and characterization of the RF properties of ICRH antennas. Particularly, it explores the rather new domain of non-axisymmetric tokamak plasmas. The resulting findings will contribute to the improvement of antenna design and controller strategy in existing and next-step fusion devices. It also provides an interesting point of comparison with intrinsic 3D machines, such as stellarators.

Chapter 1

Physics background relevant to this thesis

1.1 Nuclear fission and nuclear fusion

In order to extract kinetic energy from a nuclear reaction, a negative *mass defect* [1] between reactants and products must exist. That is, the products must be lighter than the sum of masses at rest of the reactants. This *mass defect*, δ_m, is transformed into kinetic energy of the products (or radiation, i.e. photons) by Einstein's famous relation $E = \delta_m c^2$.

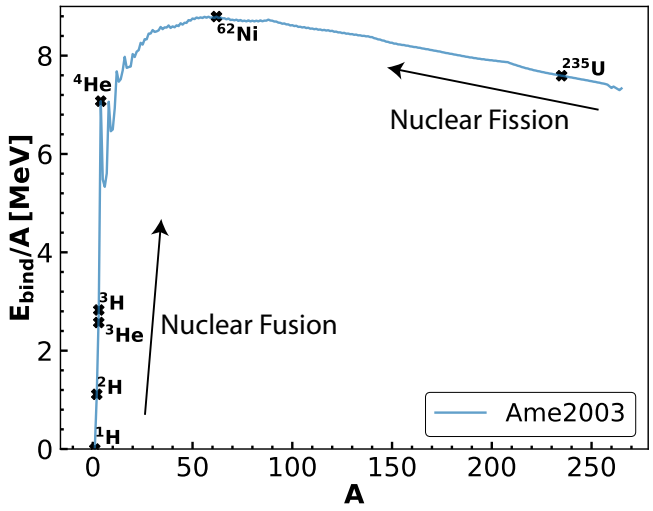

Figure 1.1: Average nucleon binding energy for a few stable elements.

The cumulative released energy in each nuclear process is, naturally, the same amount of energy one needs to supply to a given nucleus in order to split it back onto its main components (nucleons: protons and neutrons), namely the *nucleon binding energy*. An evaluation of the atomic masses for a large database of elements can be found in the *Atomic Mass Evaluation (AME)* of 2003 [2] and the resultant experimental data for such average nucleon binding energy has been graphed in **figure 1.1**. From this curve, we notice that exothermic nuclear reaction are possible in two directions, which distinguishes fusion processes from fission ones: either going from light elements such as ^{1}H, deuterium (D = ^{2}H), tritium (T = ^{3}H), etc. into heavier elements such as ^{4}He via fusion reactions, or going from very heavy elements such as ^{235}U into lighter ones via fission reactions. An understanding of the origin of this curve can be given through the *liquid drop model* of the atomic nucleus postulated by Weizsäcker, Bohr and Wheeler in the 1930s [3]. For the sake of brevity, we will simply state that nucleons achieve a more stable configuration when combined together, thus the general trend on energy release as we go from H to ^{62}Ni. From there on, however, heavier elements possess smaller average nucleon binding energies. In a nucleus, a competition between the strong interaction and the Coulomb repulsion from protons happens. In the absence of these interactions, the most stable nucleus configuration contains the same

number of protons and neutrons, due to the Pauli exclusion principle. The strong interaction decays rapidly with distance, while the Coulomb interaction is described by an inverse distance square law. Due to this, heavier nuclei tend to be in a less stable configuration than lighter ones, which is also the reason why more neutrons are needed for a given number of protons in order to stabilize the nucleus. Lighter elements such as He, Li, C, etc., are naturally present in the environment due to stellar nucleosynthesis, whereas heavier nuclei than ^{62}Ni require an energy expenditure, that is, the reaction is endothermic, and thus are only made available in small quantities during supernovae events.
In this thesis, we are concerned only with nuclear fusion processes, and so we will introduce from now on some basic notions of how fusion reactions occur and how we can take advantage of them in order to produce energy in a reactor.

1.1.1 Fusion reactions' cross-sections

Nuclear reactions between two particles depend on the given particle channel cross-section σ. The cross-section determines the likelihood of a given reaction to occur. For a fusion reaction to happen, particles must have enough energy as to overcome the Coulomb barrier potential. This is eased by the tunneling effect, and thus the cross-section is proportional to the Gamow penetrability factor $\sigma_{\text{fus}} \sim e^{-B_G/\sqrt{E}}$, where E is the energy in the particles' center of mass. Quantum mechanics also dictates that the cross-section is proportional to a geometrical factor determined by the de Broglie wavelength of the system $\pi\lambda_{dB}^2 \sim 1/E$. Lastly, nuclear physics also intervenes in the cross-section through S-wave resonances of the compound system. Thus, the fusion cross-section has been commonly factorized as [4]:

$$\sigma_{\text{fus}} \sim S(E)\frac{1}{E}e^{-B_G/\sqrt{E}} \tag{1.1}$$

With $B_G = \pi\alpha Z_1 Z_2\sqrt{2m_r c^2}$ the Gamow constant, $\alpha = e^2/\hbar c$ the fine structure constant and m_r the reduced mass of the particles. The S-function, $S(E)$, represents more clearly the nuclear part of the cross-section, for instance, the fact that $\mathbf{D}(\mathbf{T},\mathbf{n})\alpha$ exhibits a strong near-threshold S-wave resonance at about E ∼ 64 keV. This resonance makes D-T reactions the most-likely ones in this energy range. At these high energies, a collection of atoms would be found in a plasma state, in which electrons are no longer bound to the nuclei in their orbitals, but rather behave independently, only susceptible to electromagnetic and collective effects. Since a plasma in the ∼ keV energy range can be enclosed within a magnetic confinement fusion reactor, it is thus seen in the short-term as the most promising reaction for a future power plant, yielding [5]:

$$^2_1\text{D} + ^3_1\text{T} \rightarrow ^4_2\text{He}\,(3.5\,\text{MeV}) + ^1_0\text{n}\,(14.1\,\text{MeV}) \tag{1.2}$$

Another good candidate fusion reaction is the $\mathbf{D}(^3\mathbf{He},\mathbf{p})\alpha$ one, which releases about 18.3 MeV. However, this reaction releases a proton, instead of a neutron. Protons are confined in the magnetic field of the reactor, and do not escape it right away as in the neutron case. Since the current approach to energy harvest from a fusion reactor relies on the neutrons to carry their kinetic energy, impinge in the walls, and convert it into thermal energy, proton-producing reactions are dismissed. In the future, however, a neutron-less reaction could be very beneficial. Neutrons are nowadays the main energy extraction method, but also the main contributors to power plant wear and wall material activation. A power plant able to convert more efficiently the fusion products into electric energy, and thus work with a neutron-less reaction, would be

ideal. It needs to be said, however, than in a D-^{3}He fuel mixture, D-D reactions would occur. D-D reactions contain two branches: $\mathbf{D(D,n)\,^3He}$ and $\mathbf{D(D,p)T}$, such that one produces one neutron, and the other T, which would produce D-T reactions and thus release an additional neutron. Nevertheless, in the E $\sim$ 120 keV energy range, D-^{3}He is more likely than D-D, which would represent a more beneficial situation than simply using D-T. On the other hand, there is the question of fuel availability. Deuterium and tritium can be extracted from marine water and lithium respectively, whereas ^{3}He is more scarce. There are, however, studies that point out the feasibility of ^{3}He extraction from the Moon's regolith [6].
In order to assess the efficiency of a fusion reactor, whatever fuel mixture is chosen, we introduce the fusion reactivity $\langle\sigma_{\text{fus}}v\rangle$, which defines the number of fusion reactions, $\mathcal{R}$, per volume and second. This is the quantity that really determines the optimum exploitation conditions of a given channel. If we consider a two-species reaction with distribution functions $f_i(\vec{v}_1)$, $f_j(\vec{v}_2)$, we can integrate σ_{fus} over velocity space, such that:

$$\mathcal{R}_{ij} = \iint f_i(\vec{v}_1) f_j(\vec{v}_2)\, \sigma^{ij}_{\text{fus}}(|\vec{v}_1 - \vec{v}_2|)\, |\vec{v}_1 - \vec{v}_2|\, \mathrm{d}^3v_1 \mathrm{d}^3v_2 = \frac{n_i n_j}{1+\delta_{ij}} \langle \sigma^{ij}_{\text{fus}} v \rangle \tag{1.3}$$

With n_i, n_j the species densities, which are taken out of the integral under the assumption of a thermal plasma following Maxwell-Boltzmann distribution. The Kronecker delta, δ_{ij}, avoids repeated counting if there is only one species. The definition of the fusion reactivity also hints to the importance of heating methods able to alter the velocity distribution functions, i.e. NBI or ICRF can create fast-ion tails which may have a positive impact on the fusion reactivity. Cross-sections and reactivities are presented in **figure 1.2** for the energy range of interest.

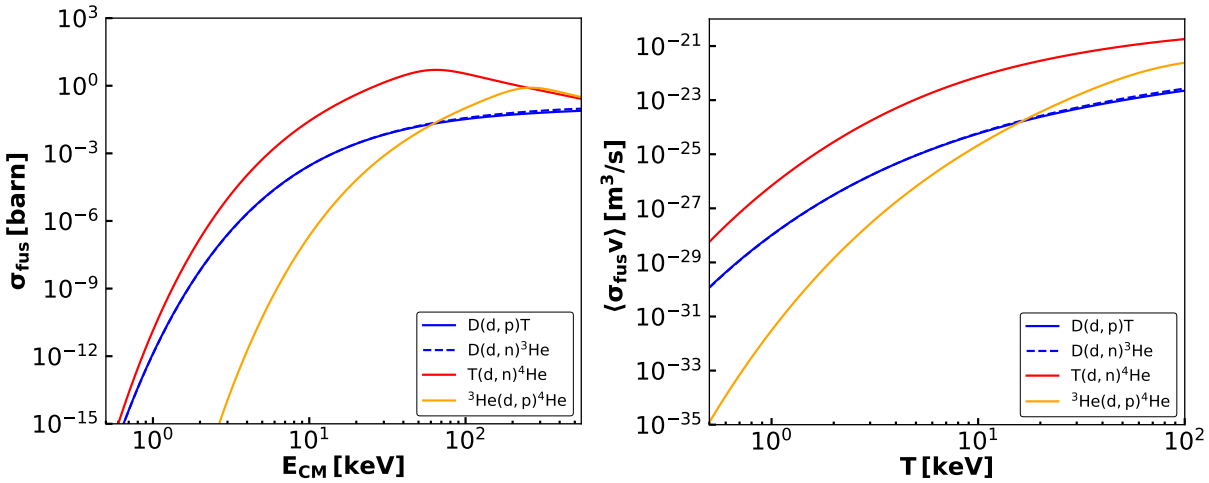

Figure 1.2: Left: fusion cross-sections, σ_{fus}, as a function of the energy in the center of mass. Right: reactivities $\langle\sigma_{\text{fus}}v\rangle$ as a function of temperature.

1.1.2 Ignition condition: The triple product

We may now ask the question of what are the minimum conditions in order to have a positive gain of fusion energy in a reactor. For that, we may define a figure of merit that relates the ratio of the produced thermonuclear power in the fusion reactions, P_{tn}, to the external heating power needed to heat the plasma, P_H, i.e. the Q-factor:

$$Q = \frac{P_{\text{tn}}}{P_H} \quad \text{with} \quad P_{\text{tn}} = \iiint \mathcal{R}\mathcal{E}\, \mathrm{d}V \tag{1.4}$$

Where $\mathcal{E}$ is the kinetic energy of the fusion products and dV is the differential of volume. In a D-T plasma, the most efficient mixture is that of 50% deuterium to 50% tritium. Furthermore, for the plasma bulk energy balance, only the contribution of the produced α-particles is important. Since the neutrons are not confined, they do not contribute to plasma heating (assuming no power recirculation). Thus, in steady-state, the power balance can be written as:

$$P_\alpha + P_H = P_{\text{loss}} \tag{1.5}$$

With $P_\alpha = \frac{1}{5}P_{\text{tn}}$ and P_{loss}, the power loss due to Bremsstrahlung, conduction, confinement quality, etc. In fusion devices, these loss mechanisms are usually expressed as a single macroscopic constant, namely, the energy confinement time τ_{E}. This leads to the definition of:

$$P_{\text{loss}} = \frac{\mathcal{W}}{\tau_{\text{E}}} \quad \text{with} \quad \mathcal{W} = \iiint 3nT \, \mathrm{d}V \tag{1.6}$$

Which states that the energy confinement time is the time it takes for the plasma to lose its thermal energy, $\mathcal{W}$, if no other heating sources are applied. The definition of $\mathcal{W}$ here provided stems from the equipartition theorem for electrons and ions assuming $n_e = \sum_i n_i = n$, $(Z = 1)$ and $T_e = T_i = T$. The most efficient situation, and limit case, is that in which external heating is not needed anymore, and the plasma bulk can be self-heated by the α-particle generation. This is termed *ignition*. According to **equation 1.4**, this corresponds to $Q \to \infty$. In this situation, we may reduce the power balance of **equation 1.5** in order to derive a sufficient condition for ignition, the so-called *Lawson criterion* [7]:

$$P_\alpha = P_{\text{loss}} \to \frac{\mathcal{E}_\alpha}{4}\overline{n^2}\,\overline{\langle\sigma_{\text{fus}}v\rangle}V = \frac{3\bar{n}\bar{T}}{\tau_{\text{E}}}V \to \overline{n}\tau_{\text{E}} = \frac{12\bar{T}}{\mathcal{E}_\alpha\overline{\langle\sigma_{\text{fus}}v\rangle}} \tag{1.7}$$

Where integration is performed over the plasma volume under the assumption of flat kinetic profiles, $\bar{n}$, $\bar{T}$ = const. Furthermore, $\langle\sigma_{\text{fus}}v\rangle \propto T^2$ in the $T \sim 10 - 20\,\text{keV}$ range [8], which helps to express the ignition condition as a product of quantities of interest:

$$\bar{n}\tau_{\text{E}}\bar{T} > 3 \times 10^{21}\,\text{m}^{-3}\text{keVs} \tag{1.8}$$

This expression is termed the *triple product*. Naturally, the constant on the right hand side is a function of the shape of the plasma profiles used in the integration. Finally, it is also to be noted that an economically-viable fusion reactor does not need to reach ignition, but a high enough Q-factor would be sufficient.

1.2 The approaches to fusion power. The tokamak: The ASDEX Upgrade tokamak

In the previous section, the Lawson criterion was introduced. In order to make nuclear fusion a feasible and economically-viable energy source, it should be maximized as much as possible. Several concepts to materialize this idea have been developed through the 1940s up to nowadays, each with advantages and disadvantages. As of now, the two most promising methods can be classified in: inertial confinement fusion and magnetic confinement fusion. Inertial confinement fusion relies on the adiabatic compression of thermonuclear material. Usually, a microscopically smooth spherical pellet filled with a deuterium-tritium mixture will be homogeneously ablated by an array of lasers, driving the fuel compression [9]. This compression increases the thermal

energy of the fuel, which reaches thermonuclear temperatures. This method's main difficulty is the low efficiency of lasers to transform electric power into fuel heating, and thus falls behind the current progress in magnetic confinement nuclear fusion in terms of the Q-factor. The latter relies on the confinement of the thermonuclear fuel inside a toroidal device by means of applying a magnetic field. The plasma levitates inside the fusion chamber without much contact with the walls, which allows its confinement for long periods of time while remaining at thermonuclear temperatures. For a complete explanation on the description of plasmas under such conditions, we refer the reader to [10]. In its more complex picture, the group of particles composing a plasma can be treated statistically through the kinetic equation, which gives the time-evolution of the particles distribution function down to thermodynamic equilibrium:

$$\partial_t f_s + \frac{\vec{p}}{m}\vec{\nabla} f_s + \vec{F}\,\partial_{\vec{p}} f_s = (\partial_t f_s)_{\text{coll}} \tag{1.9}$$

Where $f_s(\vec{x},\vec{v},t)$ is the 6-dimensional time-dependent particle distribution function of a given species s. In the above equation, $(\partial_t f_s)_{\text{coll}}$ represents the change of the distribution function due to collisions among the particles, whereas $\vec{F}$ represents the action of an external force such as gravity, a magnetic field, or the average contribution of the other particles to electric and magnetic fields. If the system is close to thermodynamic equilibrium, i.e. through the action of collisions, this kinetic equation can be integrated in velocity space to yield fluid equations, such as the Navier-Stokes equations. If the plasma is further considered to be a non-viscous fluid, one obtains the Euler equations. Here, each particle species, i.e. electrons, ions and neutrals can be treated as fluid elements connected through sources, sinks and Maxwell equations for the macroscopic electric and induction fields. In its simpler picture, one can average the independent fluid contributions into a single, neutral, fluid picture, yielding:

$$\begin{cases} D_t\rho = -\rho\vec{\nabla}\vec{v} \\ \rho D_t\vec{v} = -\vec{\nabla}p + \vec{j}\times\vec{B} \\ \vec{E} + \vec{v}\times\vec{B} = \sigma^{-1}\vec{j} \\ d_t\left(\dfrac{p}{\rho^\gamma}\right) = 0 \end{cases}$$

This is known as the single-fluid MHD (Magnetohydrodynamic) picture. In equilibrium, the material derivative $\left(D_t = \partial_t + (\vec{v}\cdot\vec{\nabla})\right)$ will not be time-dependent, i.e. $\partial_t = 0$. If we neglect the fluid flow ($\vec{v} = 0$), and assume infinite conductivity ($\sigma \to \infty$, ideal MHD limit), equilibrium is achieved when the plasma kinetic pressure is compensated by the Lorentz force felt by the fluid elements due to the magnetic field, this is:

$$\vec{\nabla}p = \vec{j}\times\vec{B} \quad \to \quad \vec{B}\cdot\vec{\nabla}p = 0, \quad \vec{j}\cdot\vec{\nabla}p = 0 \tag{1.10}$$

Under these conditions, surfaces exist of constant pressure to which the magnetic and current fields are perfectly tangential. By the Poincaré-Hopf theorem [11], such "flux surfaces" must be tori or Klein bottles. The latter being unrealizable in real space, we are left with tori as the only possibility. This mathematical foundation has motivated the pursuit of fusion with machines such as the tokamak or the stellarator [12], which are toroidal in nature. In fact, simpler, linear configurations were previously explored, such as the {z}-pinch or the screw-pinch, which suffer from strong instabilities or particles losses. In this way, magnetic confinement fusion research has mainly converged to the study of toroidal configurations. In the tokamak and stellarator, a

helical induction field confines the plasma. The main difference between these two machines is *how* this field is produced. In the tokamak (Russian acronym for **to**roidal chamber (**ka**mera) with **ma**gnetic (**k**) coils), an external set of poloidally-wound coils produces an almost-homogeneous (proportional to $\sim 1/R$) toroidal magnetic field. The missing poloidal component, needed to achieve helical lines, is supplied by a toroidal current induced in the plasma by a central solenoid by virtue of time-dependent flux change (Lenz's law). In the stellarator (Latin/English acronym for **stella** (star) + gene**rator**), both components, toroidal and poloidal, are produced by a set of external coils. Due to the difficulty of generating such a field by employing uniquely external conductors, stellarators are either constructed by a combination of toroidal and helical coils, or by a set of modular coils. The complexity of such coils makes the engineering requirements quite demanding. Positively, the stellarator is a steady-state machine, as no flux pumping is necessary, while on the other hand, the fast particle confinement is usually worse than in the tokamak.

The experimental and modeling work presented in this Ph.D. thesis has been performed uniquely on the ASDEX (**A**xially **S**ymmetric **D**ivertor **EX**periment) Upgrade tokamak, located in the Max Planck Institute for Plasma Physics (IPP), Germany. This machine is characterized by a divertor configuration, in which the core region is separated from the open field line region by a magnetic separatrix, made to intersect the wall at a specific location (divertor, see **figure 1.3**). The vessel first wall is covered with full tungsten tiles. A few parameters of interest are included in **table 1.1**. A comprehensive description of its scientific program can be found in [13].

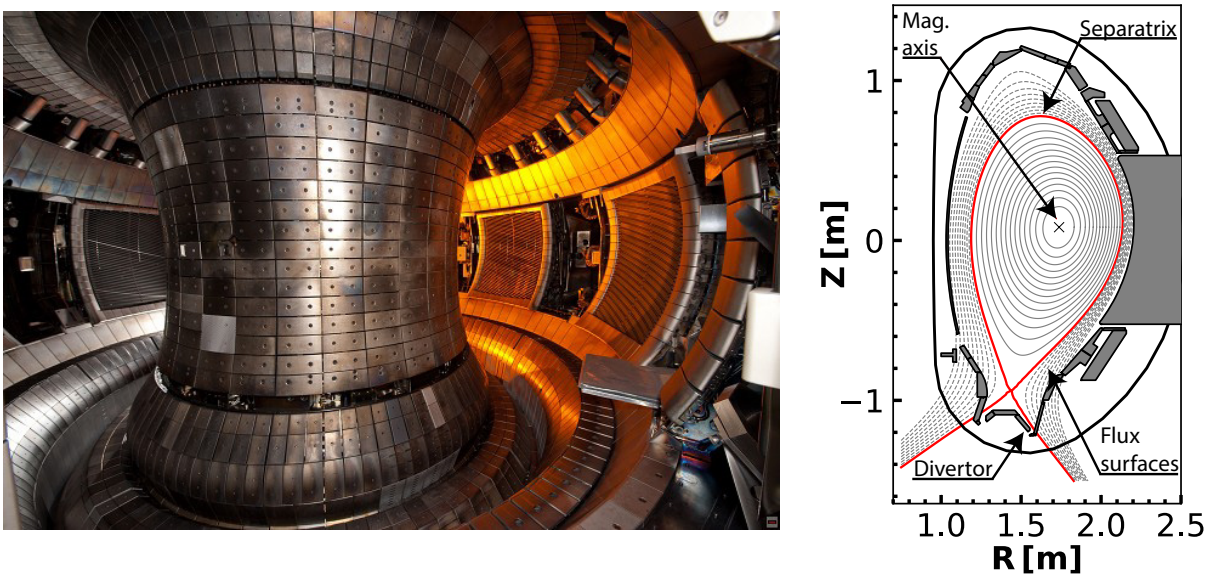

Figure 1.3: Left: Inner view of the ASDEX Upgrade tokamak vessel. Right: Poloidal cross section (ϕ = const. in a toroidal coordinate system). Named are the divertor region, the inner and outer flux surfaces, the separatrix and the magnetic axis.

Nearly 36 MW of heating power are installed in ASDEX Upgrade with the aim of bringing the plasma to fusion-relevant temperatures and to produce non-inductive current drive. A brief description of the physics involved in each heating method is introduced in the next section. We will mainly focus on ion cyclotron heating, and contrary to ASDEX's name, to the implications of non-axially-symmetric configurations on the accessibility of such waves to the core plasma.

R (Major radius)	1.65 m
a (Minor radius)	0.5 m (circular) - 0.8 m (elongated)
B_t (Maximum on-axis toroidal induction field)	3.9 T
I_p (Maximum on-axis plasma current)	2.0 MA
P_{ICRF} (Ion cyclotron net installed power)	8 MW
P_{ECRH} (Electron cyclotron net installed power)	8 MW
P_{NBI} (Neutral beam net installed power)	20 MW

Table 1.1: ASDEX Upgrade parameters of interest.

1.3 External heating methods. ICRF Heating. The ICRF coupling description

Fusion reactivity depends critically on the plasma temperature, and more specifically, on the ion distribution function. In order to achieve the optimum temperatures for ignition in a reactor, heating methods should be able to increase the total net plasma energy up to the desired conditions. Aside from the α-particle heating regime achieved close to thermonuclear temperatures, three main methods are commonly used in experimental reactors of the magnetic confinement type: Ohmic dissipation by a plasma current, neutral particle injectors and wave heating. The first one is mainly used in two types of reactors: the reversed field pinch and the already introduced tokamak. The stellarator, benefits from producing its magnetic topology purely by external conductors, and thus plasma currents are a spurious, unwanted effect, even less a heating method. In macroscopic terms, ohmic dissipation works due to the finite resistivity attributable to a plasma. Through collisions, the parallel momentum of the particles can be distributed among further degrees of freedom, thus, thermal energy. There is a limit, however, to how much a plasma can be heated through dissipation, as the resistivity scales down with temperature. If we assume that electrons accelerated in an electric field achieve an equilibrium velocity due to collisions with ions, that is $F_e = F_c \rightarrow eE = m_e \frac{v_d}{\tau_c}$, where v_d is the *drift velocity* of the electrons and $\tau_c \sim \tau_e$ is the electron-ion collision time, one can reach an approximate expression for the resistivity (proportional to that obtained by Cohen, Spitzer and Routly [14]) such that:

$$\eta \sim \frac{m_e^{1/2} e^2 ln\Lambda}{3\epsilon_0^2 (2\pi T_e)^{3/2}} \text{ where } P_\Omega = \eta j^2 \tag{1.11}$$

With $ln\Lambda$ the Coulomb logarithm and j the current density. This expression is seen to scale as $\propto T_e^{-3/2}$, thus, the hotter the plasma, the less efficient the method becomes (although neoclassical effects can increase the local resistivity depending on the plasma geometry). At $T_e = 10\,\text{keV}$, $\eta \sim 10^{-9}\,\Omega\,\text{m}$, one order of magnitude smaller than copper or silver at room temperature.
Neutral beam injection, or "NBI", relies on the injection of fast neutrals inside the reactor. Once injected, these neutrals are ionized by the plasma in three main processes: charge exchange with plasma ions, ionization by ions and ionization by electrons. The resulting fast ions are confined in the magnetic field, where they slow down up to thermalization via Coulomb collisions. NBI heating has the advantage that it does not require equipment to be installed inside the reactor vessel, but rather, the beam neutrals are guided through a duct into a port in the reactor. On the other hand, a large infrastructure is needed outside the vessel, sometimes comparable to the torus size, in order to accommodate the accelerator grids and neutralization chamber. Furthermore,

NBI has difficulties penetrating dense large plasmas, such as the ones expected in ITER or DEMO. The beam attenuation factor can be described through the total cross-section for the three aforementioned processes and the plasma density as $(\sigma_{\text{total}} n)^{-1}$, which is of the order of tens of cm for a deuterium beam in the $\sim$ 100 keV energy range and n $\sim 10^{20}$ m^{-3}. Consequently, NBI neutrals need to be produced with larger energies, where the charge exchange and ionization cross-sections become smaller, in order to penetrate the plasma up to the core. This poses a challenge in the neutralization process at the source, which becomes less efficient at high beam ion energies. The use of negative ion sources, which neutralization can be effectively achieved even at high beam energy, becomes mandatory. ITER will be equipped with 2 negative ion NBI sources, able to provide 33 MW of heating power by either using H^0 or D^0 neutrals [15].
The last external heating method to be discussed in this section is wave heating. Eigenmodes are supported in a plasma, which can be externally excited. These are known as plasma waves. The physical description of a plasma can be given through the use of an anisotropic dielectric or permeability tensor. Due to simplicity, the dielectric tensor is commonly preferred, and will be introduced in the next section. Depending on the excitation frequency of the mode (ω) relative to the plasma ion and electron motion (cyclotron frequency $\Omega_s = q_s B/m_s$), we classify them as:

1. **Low-frequency waves:** Alfvén waves ($\omega \ll \Omega_i$). Ion cyclotron waves ($\omega \approx \Omega_i$). Electron motion effectively neutralizes space charge along field lines. Electrons can be regarded as a massless fluid.

2. **Intermediate frequency waves:** Lower Hybrid waves: Ion oscillations that drive electron motion perpendicular to field lines. Both ion and electron inertia are relevant for this mode.

3. **High-frequency waves:** Electromagnetic plasma wave, Langmuir-Tonks plasma oscillations, Whistler mode, Electron cyclotron waves ($\omega \approx \Omega_e$) and upper hybrid waves: frequency too high for ion motion to happen. Ions can be regarded as a stationary fluid.

A schematic view of the heating systems in ASDEX Upgrade can be seen in **figure 1.4**. In this thesis, we are concerned purely with the study of ion cyclotron waves. Moreover, we will focus on their accessibility to the plasma when gradients of the density profile and the magnetic field components exist in 3D.

1.3.1 The susceptibility and dielectric tensors of the cold magnetized plasma

The treatment of plasma waves requires a mathematical description binding the interplay between microscopic particle motion and macroscopic wave properties, such as the oscillating E,B-fields. First introduced by Stix [16], a locally homogeneous plasma can be modeled as a dielectric material with no free current $\vec{J}_{\text{free}} = 0$, but bound charges. One may think of $\vec{J}$ as a polarization current density ($\vec{J}_{\text{pol}}$) in a dielectric medium and introduce a dielectric tensor. Assuming the background plasma to be static, bound charges will oscillate linearly from equilibrium, that is $\propto e^{i(\vec{k}\vec{r}-\omega t)}$. Therefore, any other related quantity will vary with the same behavior. Unlike the canonical derivation by Stix, which uses the microscopic formulation of Maxwell equations in Gaussian CGS units, for consistency in this thesis, we will start from the SI units macroscopic formulation of Ampère-Maxwell equation:

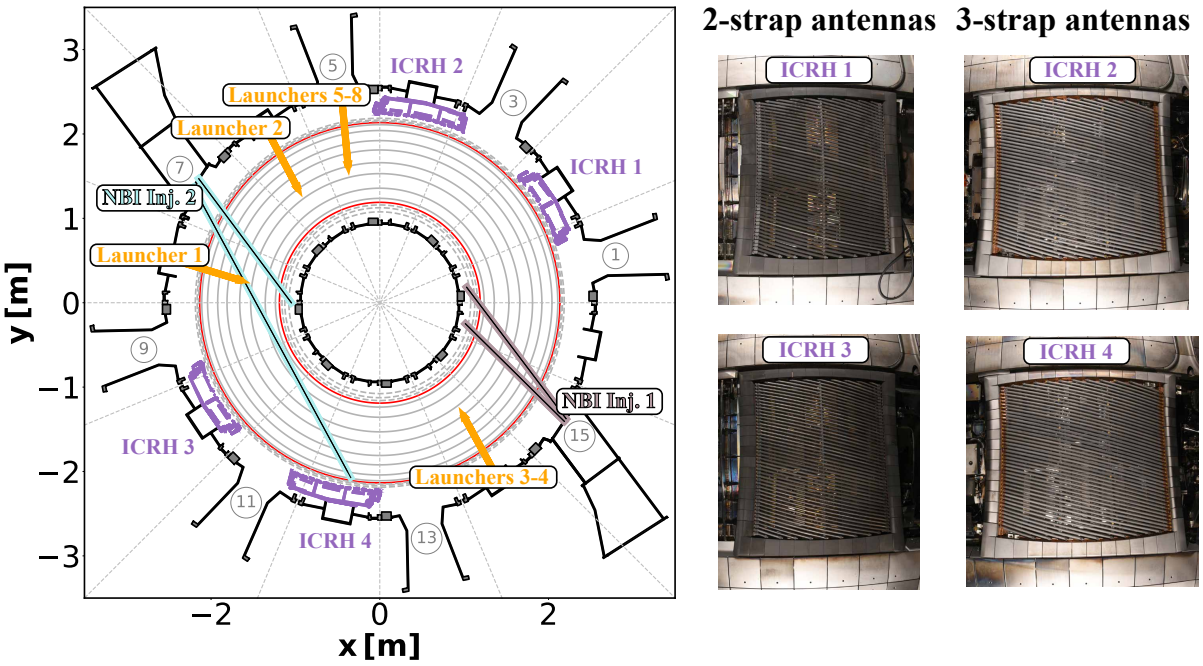

Figure 1.4: Left: ASDEX Upgrade toroidal cross-section with external heating methods. ECRH is installed in ports 5, 6, 8 and 14. NBI injectors are installed in ports 7 and 15, each of the injectors can accelerate up to 4 beams. ICRF antennas are installed in sectors 2, 4, 10 and 12. Antennas in ports 2 and 10 are 2-strap antennas, antennas in ports 4 and 12 are 3-strap antennas. Right: In-vessel pictures of the ICRF antennas.

$$\begin{cases} \vec{\nabla} \times \vec{H} = \partial_t \vec{D} = \epsilon_0 \partial_t \vec{E} + \partial_t \vec{P} = \epsilon_0 \partial_t \vec{E} + \vec{j}_{\text{pol}} & (1.12) \\ \vec{D}(\omega, \vec{k}) = \overline{\overline{\epsilon}}(\omega, \vec{k}) \vec{E}(\omega, \vec{k}) = \epsilon_0 \vec{E} + \vec{P} = \epsilon_0 \vec{E} + \int \vec{j}_{\text{pol}} dt = \epsilon_0 \vec{E} + \frac{i}{\omega} \vec{j}_{\text{pol}} & (1.13) \end{cases}$$

And $\vec{j}_{\text{pol}}$ being the total polarization current due to the plasma especies s:

$$\vec{j}_{\text{pol}} = \sum_s \vec{j}_{\text{pol},s} = \sum_s n_s q_s \vec{v}_s = \sum_s \epsilon_0 \overline{\overline{\chi}}_s \partial_t \vec{E} = \epsilon_0 \sum_s \overline{\overline{\chi}}_s (-i\omega) \vec{E} \tag{1.14}$$

Combining **equations 1.13 and 1.14**, we find:

$$\overline{\overline{\epsilon}}(\omega, \vec{k}) = \epsilon_0 \epsilon_r = \epsilon_0 \left(\overline{\overline{1}} + \sum_s \overline{\overline{\chi}}_s(\omega, \vec{k}) \right) \tag{1.15}$$

Now we proceed to determine the susceptibility, $\overline{\overline{\chi}}(\omega, k)$, and dielectric $\overline{\overline{\epsilon}}(\omega, \vec{k})$ tensors. As previously stated, we will assume a locally homogeneous plasma, which can be described by the multispecies MHD fluid equations. We further assume the fluids to be cold ($p = 0$) and lossless. By using perturbation theory on Cauchy's momentum equation:

$$\rho_{m,s}\frac{D\vec{v}_s}{Dt} = \rho_s(\vec{E} + \vec{v}_s \times \vec{B}) - \vec{\nabla}\overline{\overline{\Phi}}_s \rightarrow \begin{cases} 0 = 0 & 0^{\text{th}} \text{ order} \\ m_s(-i\omega)\vec{v}_s^{(1)} = q_s(\vec{E}^{(1)} + \vec{v}_s^{(1)} \times \vec{B}^{(0)}) & 1^{\text{st}} \text{ order} \\ m_s(-i\omega\vec{v}_s^{(2)} + \vec{v}_s^{(1)}\vec{\nabla}\vec{v}_s^{(1)}) = & \\ \qquad q_s\left(\vec{E}^{(2)} + \vec{v}_s^{(1)} \times \vec{B}^{(1)} + \vec{v}_s^{(2)} \times \vec{B}^{(0)}\right) & 2^{\text{nd}} \text{ order} \\ \dots & \end{cases}$$

Where $\rho_{m,s}$ and ρ_s are the mass and charge density of the fluid elements. Here, the zero-order quantities $\vec{v}_s^{\,(0)}, \vec{E}^{(0)}$ are assumed to be 0, and the Cauchy stress tensor $\overline{\overline{\Phi}}_s = 0$ due to our cold lossless plasma assumption. We will work with the first-order equation. Solving it, one obtains:

$$v_s^{\pm} = \frac{iq_s}{m_s}\frac{E^{\pm}}{\omega \mp \Omega_s}, \quad v_z = \frac{iq_sE_z}{\omega m_s} \tag{1.17}$$

From this and using **equation 1.14**, the susceptibilities can be calculated:

$$\vec{J}_{\text{pol},s} = \epsilon_0\chi_s^{\pm}(-i\omega)E^{\pm} = n_sq_sv_s^{\pm} \tag{1.18}$$

Hence:

$$\chi_s^{\pm} = -\frac{\omega_{p,s}^2}{\omega(\omega \mp \Omega_s)}, \quad \chi_{zz,s} = \frac{-\omega_{p,s}^2}{\omega^2} \quad \text{with } \omega_{p,s} = \sqrt{\frac{n_sq_s^2}{\epsilon_0 m_s}} \tag{1.19}$$

the plasma frequency. Finally, the dielectric tensor can be written as:

$$\vec{D}(\omega,\vec{k}) = \begin{pmatrix} S & -iD & 0 \\ iD & S & 0 \\ 0 & 0 & P \end{pmatrix}\vec{E}(\omega,\vec{k}) \tag{1.20}$$

Where:

$$\begin{cases} R = 1 + \sum_s \chi_s^- = 1 - \sum_s \frac{\omega_{p,s}^2}{\omega(\omega + \Omega_s)} & \text{(1.21a)} \\ L = 1 + \sum_s \chi_s^+ = 1 - \sum_s \frac{\omega_{p,s}^2}{\omega(\omega - \Omega_s)} & \text{(1.21b)} \\ P = 1 + \sum_s \chi_{z,s} = 1 - \sum_s \frac{\omega_{p,s}^2}{\omega^2} & \text{(1.21c)} \\ S = 1/2(R + L), \quad D = 1/2(R - L) & \text{(1.21d)} \end{cases}$$

1.3.2 The ICRF dispersion relation

Having the dielectric tensor means that we can now solve the wave equation:

$$\vec{\nabla} \times (\vec{\nabla} \times \vec{E}) = -\mu_0\epsilon_0\overline{\overline{\epsilon_r}}\partial_t^2\vec{E} \rightarrow \vec{\nabla} \times (\vec{\nabla} \times \vec{E}) - \omega^2\mu_0\overline{\overline{\epsilon}}\vec{E} = 0 \tag{1.22}$$

The wave equation is strongly bounded to the conditions of the medium with dielectric tensor $\overline{\overline{\epsilon_r}}$. Hence, the assumptions made in the derivation of $\overline{\overline{\epsilon_r}}$ will dictate what kind of eigenvalues

(waves) this medium will have. Appealing to the linear nature of our analysis to simplify the wave equation and by conveniently introducing the refractive index, n, as our "looking-for" eigenvalue, we can write this equation in matrix form:

$$\begin{pmatrix} S - n^2\cos(\theta) & -iD & n^2\cos(\theta)\sin(\theta) \\ iD & S - n^2 & 0 \\ n^2\cos(\theta)\sin(\theta) & 0 & P - n^2\sin^2(\theta) \end{pmatrix} \begin{pmatrix} E_x \\ E_y \\ E_z \end{pmatrix} = 0 \tag{1.23}$$

Where the vector refractive index is defined as $\vec{n} = c\vec{k}/\omega$. For simplicity, the vector refractive index has been considered to have only two components $\vec{n} = (n_x, 0, n_z)$, thus some of the extra-diagonal components of the equation do not show up. The angle θ is the angle between $\vec{k}$ and $\vec{B}$ defined such as $n_x = n_\perp = |n|\sin(\theta)$ and $n_z = n_\parallel = |n|\cos(\theta)$, where {z} is parallel propagation to the B-field and {x} is perpendicular. The full characteristic polynomial can be written as:

$$\begin{cases} An^4 - Bn^2 + C = 0 & \\ A = S\sin^2(\theta) + P\cos^2(\theta) & (1.24a) \\ B = RL\sin^2(\theta) + PS(1 + \cos^2(\theta)) & (1.24b) \\ C = PRL & (1.24c) \end{cases}$$

In the case of ICRF waves excited by an antenna, the $k_\parallel$ spectrum is fixed by its geometry. A more relevant expression is thus [17]:

$$\begin{cases} A_1 n_\perp^4 - B_1 n_\perp^2 + C_1 = 0 & \\ A_1 = S & (1.25a) \\ B_1 = -(S + P)n_\parallel^2 + RL + PS & (1.25b) \\ C_1 = P(n_\parallel^2 - R)(n_\parallel^2 - L) & (1.25c) \end{cases}$$

In this frequency range, the characteristic polynomial can be simplified through the following assumptions:

1. $\omega \ll \omega_{p,e}$, such that $|P| \gg 1$.
2. Negligible electron mass, i.e., $m_e \to 0$.

These approximations imply $|\mathrm{R}|, |\mathrm{L}|, |\mathrm{S}| \ll |\mathrm{P}|$ and $|\mathrm{RL}| \ll |\mathrm{P}(\mathrm{S} - \mathrm{n}_\parallel^2)|$. They also hold for a large range of parameters in the $\{n_e, |\vec{B}|, \%H\}$ space, as can be seen in **figure 1.5**. The bi-quadratic **equation 1.25** can be solved as a series expansion, which yields in the lowest order under these approximations the two well-known roots for low-frequency plasma waves.

$$n_{\perp,\mathrm{FW}}^2 = \frac{(R - n_\parallel^2)(L - n_\parallel^2)}{S - n_\parallel^2}, \quad n_{\perp,\mathrm{SW}}^2 = \frac{P(S - n_\parallel^2)}{S} \tag{1.26}$$

The first root corresponds to the fast wave (FW), while the second represents the slow wave (SW). In this thesis, we are mainly concerned with the fast wave behavior, which is the one that can be coupled to the core plasma. Under regular tokamak conditions, the slow wave is strongly evanescent, and thus cannot propagate. It is readily seen that the fast wave experiences two main cutoffs ($n_\perp^2 = 0$), one at $n_\parallel^2 = R$, the so-called R-cutoff and $n_\parallel^2 = L$, the so-called L-cutoff.

Furthermore, the wave also experiences the Alfvén resonance at $S = n_{\parallel}^2$.

For standard toroidal devices, the ICRF fast wave is excited by an antenna integrated within the wall of the vacuum vessel. Due to the low-density conditions at the plasma edge, the fast wave transits an evanescent region before accessing the core plasma, as seen in **figure 1.6**. At the edge, $n_{\perp,\mathrm{FW}}^2 < 0$ up to the R-cutoff, where the wave becomes propagative. This evanescent region determines the radiation impedance of the antenna [18], and thus the ICRF coupling properties, the antenna performance and behavior, and the RF transmission line quantities such as voltage standing wave ratio (VSWR), voltage maxima (V_{max}), etc., that are introduced in the next section.

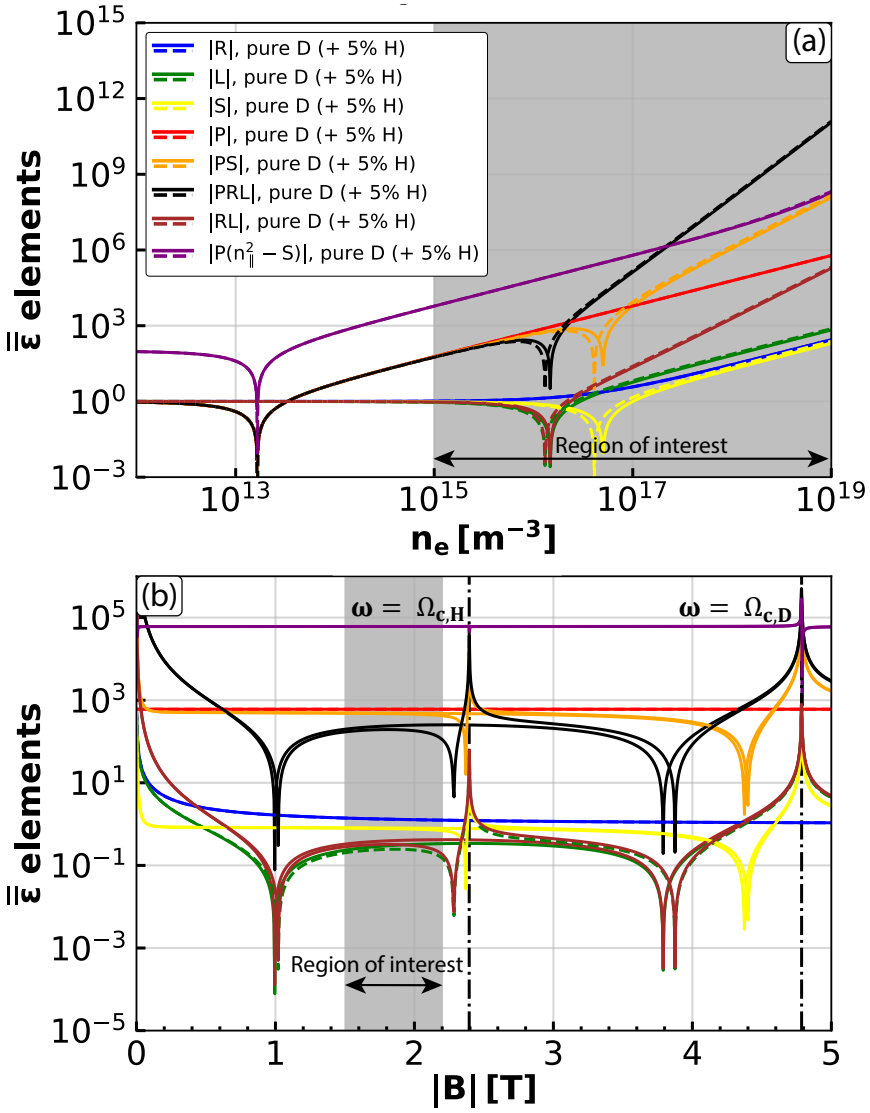

Figure 1.5: Absolute values of the cold plasma dielectric tensor elements (a) as a function of plasma density at constant $|B| = 2\,\mathrm{T}$, (b) as a function of magnetic induction field at constant $n_e = 1 \times 10^{16}\,\mathrm{m}^{-3}$. Elements are computed for a pure deuterium plasma (solid) and a D plasma with 5% H content (dashed). A value of $k_{\parallel} = 7.7\,\mathrm{m}^{-1}$ was used. The antenna frequency was taken to be $\nu_{\mathrm{antenna}} = 36.5\,\mathrm{MHz}$

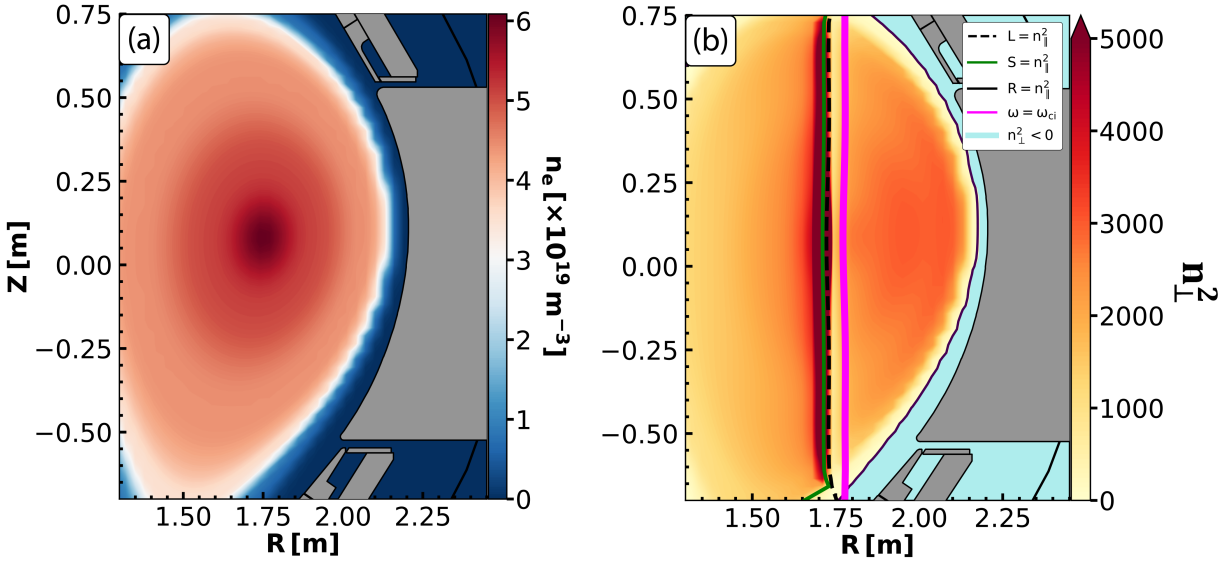

Figure 1.6: (a) Electron density profile from IDA (see **section 2.1.5**) mapped to the CLISTE equilibrium for discharge #34632 at $t = 3\,\mathrm{s}$. (b) $n^2_{\perp,\mathrm{FW}}$ as calculated by **eq. 1.26** for a D plasma with 5% H concentration, $k_\parallel = 7.7\,\mathrm{m}^{-1}$ and $\nu_{\mathrm{antenna}} = 36.5\,\mathrm{MHz}$. Blue color represents $n^2_{\perp,\mathrm{FW}} < 0$. Highlighted are the R- and L-cutoffs, the Alfvén (S) resonance and the ion cyclotron resonance for fundamental H and second harmonic D.

1.3.3 RF Antenna and transmission line theory

ICRF antennas are fed by a coaxial transmission line connected to a generator, a doodle of such a system can be seen in **figure 1.7**. The electrical connection is such that the inner conductor of the transmission line extends until becoming the antenna strap. Direct measurements of the relevant electrical quantities within the antenna such as the voltage and current are often challenging in a fusion and RF-intensive environment, and that is why most ICRF systems are diagnosed from the transmission line side, outside the main vessel. In order to extract useful information about the antenna performance, an electrical model of the transmission line and ICRF antenna must be used.

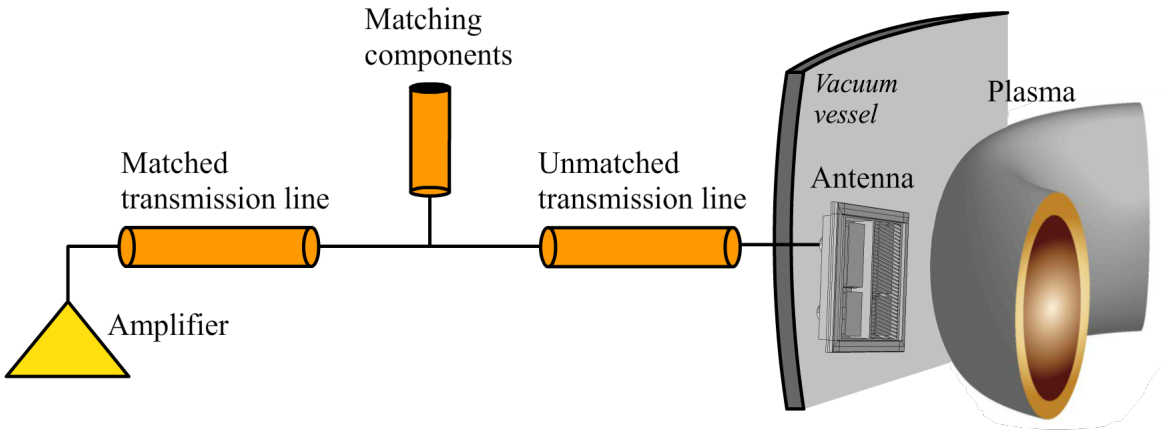

Figure 1.7: Schematic of an ASDEX Upgrade ICRF circuit from the amplifier to the antenna.

O. Heaviside devised what is now known as the circuit model of transmission lines [19], which we briefly introduce here. ICRF transmission lines are of the coaxial type, carrying a transverse electromagnetic mode (or TEM). The reason, is the low loss that a TEM line has in the $\sim 100\,\mathrm{MHz}$ range. A TEM mode needs a current to excite the transverse E-, B-fields (see Helmholtz equations); in this case, the inner conductor of the coaxial line carries this current. Taking an infinitesimal section of the line, the inner conductor can be assumed to have a series impedance, Z', consisting of a resistance per unit length, R', which accounts for the Ohmic losses, and an inductance per unit length, L'. The medium between the inner and outer conductors is usually filled with a dielectric, where a radial electric field exists. We thus include a parallel admittance, Y', consisting of a conductance per unit length, G', which represents the losses in the dielectric and a capacitance per unit length, C', between the plates. By applying Kirchhoff's circuital laws, one can obtain a set of equations relating the voltage, V, and current, I, in the line [20]:

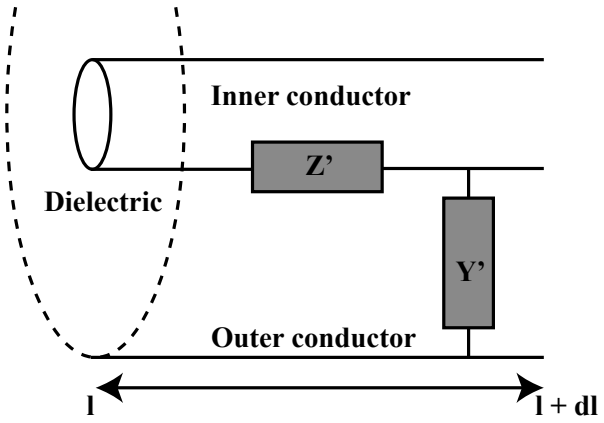

Figure 1.8: Circuit model of a coaxial transmission line.

$$\begin{cases} -\partial_l V(l,t) = R' I(l,t) + L' \partial_t I(l,t) & (1.27) \\ -\partial_l I(l,t) = G' V(l,t) + C' \partial_t V(l,t) & (1.28) \end{cases}$$

Commonly known as the telegrapher equations. In steady-state, this coupled system of PDEs has a general solution that allows for standing waves, which consist of a forward-propagating wave and a backward-propagating one:

$$\begin{cases} V(l) = V_+ e^{-i\beta_c l} + V_- e^{i\beta_c l} = V_+(l) + V_-(l) & (1.29) \\ I(l) = \dfrac{1}{Z_c}\left[V_+ e^{-i\beta_c l} - V_- e^{i\beta_c l}\right] = \dfrac{1}{Z_c}\left[V_+(l) - V_-(l)\right] & (1.30) \end{cases}$$

Where $\beta_c = -i\sqrt{Z'Y'}$ and $Z_c = \sqrt{Z'/Y'}$. In practice, the line is assumed lossless and $Z_c \sim Z_0 = \sqrt{L'/C'}$, the characteristic line impedance.
With a lossless line in steady-state, the losses can only occur at the antenna location. The conversion of power sent by the generator into radiation fields can be studied with the complex Poynting theorem. Starting from Ampère-Maxwell and Faraday's equations, we obtain:

$$\begin{cases} \vec{\nabla} \times \vec{H} = \vec{j} + \partial_t \vec{D} & (1.31) \\ \vec{\nabla} \times \vec{E} = -\partial_t \vec{B} & (1.32) \end{cases}$$

$$\rightarrow \vec{E}(1.31) - \vec{H}(1.32) \rightarrow -\vec{\nabla} \cdot \left(\vec{E} \times \vec{H}\right) = \vec{E}\vec{j} + \left(\vec{H}\overline{\overline{\mu}}\partial_t \vec{H} + \vec{E}\overline{\overline{\epsilon}}\partial_t \vec{E}\right) \quad (1.33)$$

Where the term on the lhs. is the divergence of the Poynting vector, $\vec{P} = \vec{E} \times \vec{H}$. If we choose to enclose the antenna by a volume where to apply the divergence theorem, the power balance can be obtained as:

$$-\iint_{\partial V}\vec{P}\,d\vec{S}-\iiint_{V}\vec{E}\vec{j}\,dV=\iiint_{V}\left(\vec{H}\overline{\overline{\mu}}\partial_t\vec{H}+\vec{E}\overline{\overline{\epsilon}}\partial_t\vec{E}\right)dV \tag{1.34}$$

Which relates the loss of electromagnetic energy within the volume to the outward power flow from its enclosing surface (first term lhs.) and the volumetric ohmic losses within the system (second term lhs.), which are attributable to the antenna conductors and transmission lines. In assuming the antenna straps and the transmission lines perfectly conducting, we can remove the second integral on the lhs. Since an antenna is fed by a generator in order to keep it working, the Poynting vector crossing the surface can be split into two contributions: $\vec{P}=\vec{P}_{\text{rad}}-\vec{P}_{\text{gen}}$, where $\vec{P}_{\text{rad}}$ represents the far field radiated power, and $\vec{P}_{\text{gen}}$ is the power flow from the generator across the surface into the antenna strap. For a multiport antenna network (with N ports), the power flow can be expressed as [21]:

$$\begin{cases}\displaystyle\iint_{\partial V}\vec{P}_{\text{gen},ij}\,d\vec{S}=V_i(l)I_j(l) & (1.35)\\ \displaystyle\iint_{\partial V}\vec{P}_{\text{rad},ij}\,d\vec{S}=\iint_{\partial V}\vec{E}_i\times\vec{H}_j\,d\vec{S} & (1.36)\end{cases}$$

With $V_i(l)$ and $I_i(l)$ given by **equations 1.29, 1.30** if we switch to frequency domain, and l is evaluated at the plane generated by the cross section between the enclosing volume and the transmission lines. With the fields decomposed according to the superposition principle due to each port $\vec{E}=\sum_1^N\vec{E}_i$, $\vec{H}=\sum_1^N\vec{H}_i$, the energy balance becomes:

$$-\iint_{\partial V}\vec{P}_{\text{rad},ij}\,d\vec{S}+V_iI_j=\iiint_{V}\left(\vec{H}_i\overline{\overline{\mu}}\partial_t\vec{H}_j+\vec{E}_i\overline{\overline{\epsilon}}\partial_t\vec{E}_j\right)dV \tag{1.37}$$

Since these quantities are assumed periodic in time, we are interested in the time-averaged power balance rather than the instantaneous one. By integrating in time and switching to phasor notation, we obtain:

$$\begin{aligned}&\frac{1}{T}\int_0^T(1.37)dt\rightarrow-\iint_{\partial V}\left\langle\vec{P}_{\text{rad},ij}\right\rangle_t d\vec{S}+\text{Re}(V_iI_j^*)=0\\ &\text{Im}(\vec{P}_{\text{rad},ij})=0\rightarrow\text{Im}(V_iI_j^*)=\omega\iiint_{V}\left(\vec{H}_i^*\overline{\overline{\mu}}\vec{H}_j-\vec{E}_i\overline{\overline{\epsilon}}\vec{E}_j^*\right)dV\end{aligned} \tag{1.38}$$

where every term $\frac{1}{T}\int_0^T Xe^{\pm2i\omega t}dt=0$. By virtue of $V_i(l)=Z_{ij}(l)I_j(l)$:

$$Z_{ij}=\frac{1}{|I_j|^2}\left[\left\langle P_{\text{rad},ij}\right\rangle_t+i\omega\iiint_{V}\left(\vec{H}_i^*\overline{\overline{\mu}}\vec{H}_j-\vec{E}_i\overline{\overline{\epsilon}}\vec{E}_j^*\right)dV\right] \tag{1.39}$$

Which is termed the *input impedance matrix*, i.e., $Z_{ij}=Z_{\text{inp}}$ and $\langle P_{\text{rad}}\rangle_t$ is the time-averaged surface-integrated radiated power. In most cases, Z_{inp} will differ from that of the transmission line, Z_0, and the line will be said to be *unmatched*. When this occurs, $|\text{V}_-|>0$ and the "voltage wave" will be first reflected at the strap short, creating a standing wave in the line. The reflection coefficient anywhere in the line can then be written as:

$$\Gamma_{ij}(l)=\frac{V_{-,i}(l)}{V_{+,j}(l)}=\frac{Z_{ij}(l)-Z_0I_{ij}}{Z_{ij}(l)+Z_0I_{ij}} \tag{1.40}$$

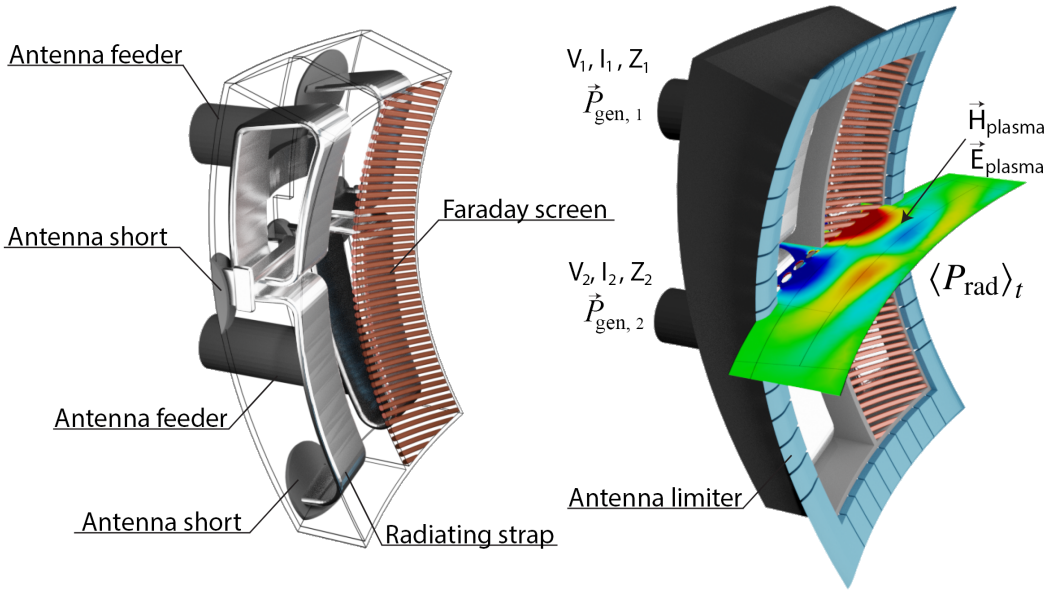

Figure 1.9: Left: Open view of the ICRF antenna box with feeder, straps and half Faraday screen. Right: With antenna box and radiated fields.

where I_{ij} is the diagonal unit matrix and the elements Γ_{ij} belong to the so-called *S-matrix*, the matrix of reflection coefficients. Generally, when multiple antenna ports are excited simultaneously, the cross-diagonal elements are not 0, i.e. $\Gamma_{ij} \neq 0 \ \forall i \neq j$. However, in experiments where the ports are not terminated on a matched load is generally not possible to separate the different contribution to the S-matrix. In this case the assumption $\Gamma_i = V_{-,i}/V_{+,i} = \Gamma$ is made for each port separately.

To protect the generator from the reflected power, matching components are added to the line, such that the total impedance seen by it is as close as possible to Z_0. This can be achieved by stub tuners, trombones, T-sections, and other elements that will not be discussed here in detail. This section of the line with low reflected power is referred to as "matched transmission line" in **figure 1.7**. The other side of the line, the "unmatched" one, has a high fraction of the power reflected at the load (antenna), and steady-state is achieved once the radiative and ohmic losses match the input power supplied by the generator. The standing wave structure in this section of the line is described by **equations 1.29, 1.30**. The circuital description of the antenna, short and given plasma is often reduced to a single quantity, $\Gamma_L = \Gamma_{\text{load}} = \Gamma_i = f(Z_{\text{inp}})$, on each antenna feeder, which is accessible both in simulations and experiments. Inverting **equation 1.40** allows relating the real part of Z_{inp} to the reflection coefficient at the load, defined as the intersection plane where V_i, I_i are evaluated. Thus:

$$\text{Re}(Z_{\text{inp}}) = \text{Re}(Z_{\text{L}}) = \text{Re}\left(Z_0 \frac{1+\Gamma_L}{1-\Gamma_L}\right) = Z_0 \left(\frac{1-|\Gamma_L|^2}{|1-\Gamma_L|^2}\right) \tag{1.41}$$

Therefore, if Γ_L and I_j can be measured, $\langle P_{\text{rad}} \rangle_t$ can be known. The measurement of Γ_L, however, presents several complications. As $\Gamma_L \in \mathbb{C}$, both its absolute value and phase must be measured. The latter often incurs large experimental errors [22]. Several methods exist: A pair of voltage and current probes can sample both the absolute values of $|V_i|$ and $|I_i|$, as well as the phase difference between them $\phi_V - \phi_I$, from which Z_i can be directly inferred. Directional

couplers in the unmatched line can also provide V_- and V_+, thus Γ. Voltage probe arrays allow the direct distribution of the voltage in the line to be sampled, from which Γ can be fitted. Significant work in the improvement of the voltage and current probe diagnostic in ASDEX Upgrade was carried out in [22], but the results turned out to be reliable only for one antenna out of the four installed. They also relied on cross-calibration ad-hoc factors against other diagnostics in the transmission lines, which would likely have to be re-evaluated for the newly installed 3-strap antennas.

A more common method to measure the antenna impedance is that of assuming the complex shape of the strap (see **figure 1.9**) can be thought to be a section of transmission line terminated at an impedance. This impedance is known as the *radiation impedance*, Z_{rad}, where I_j in **equation 1.39** becomes the current measured at the antenna short. In first approximation, this impedance is often reduced to a resistor, thus $\text{Im}(Z_{\text{rad,i}}) = 0$[1] (due to a good antenna design and small effect of the plasma on the near fields). The load at the short now fulfills $\phi(\Gamma) = -180°$, and thus:

$$Z_{\text{rad}} \in \mathbb{R},\ \phi(\Gamma_L) = -180° \rightarrow \text{Re}(Z_{\text{rad}}) = Z_0 \left[\frac{1 - |\Gamma_L|^2}{(1 + |\Gamma_L|)^2}\right] = R_L \tag{1.42}$$

This is termed the *loading resistance*. The interpretation of this quantity is simple: It is the resistance that a purely real resistor should have in order to dissipate $\langle P_{\text{rad}} \rangle_t$. The validity of this approximation will be discussed in **section 3.2.7**, for realistic experimental conditions. This expression depends uniquely on $|\Gamma|$, and therefore, it is of easier experimental accessibility. We may also reduce the expression for R_L to other quantities of interest, such as the coupled power and the maximum voltage on the transmission line. Given an incident voltage on the load V_L^+ [2], the voltage distribution along the line follows:

$$V(l) = V_L^+ e^{i\beta l}(1 + \Gamma(l)) \rightarrow |V(l)| = |V_L^+||1 + \Gamma(l)| \tag{1.43}$$

Since $1 - |\Gamma(l)| \leq |1 + \Gamma(l)| \leq 1 + |\Gamma(l)| \rightarrow V_{\text{min}} \leq V(l) \leq V_{\text{max}}$, where $V_{\text{min}} = |V_L^+|(1 - |\Gamma(l)|)$, $V_{\text{max}} = |V_L^+|(1 + |\Gamma(l)|)$. Therefore, $V(l)$ is bounded by V_{min}, V_{max}. Neglecting Ohmic losses on the transmission line, the power delivered to the load can be written as:

$$P_{\text{coupled}} = P_{\text{for}} - P_{\text{ref}} = \frac{\left(V_L^+\right)^2}{Z_0} - \frac{\left(V_L^-\right)^2}{Z_0} = \frac{\left(V_L^+\right)^2}{Z_0}\left[1 - |\Gamma_L|^2\right] \tag{1.44}$$

Since $|\Gamma(l)| = |\Gamma_L|$, it is immediate to see that:

$$\frac{P_{\text{coupled}}}{V_{\text{max}}^2} = \frac{1}{Z_0}\frac{\left(1 - |\Gamma_L|^2\right)}{(1 + |\Gamma_L|)^2} \rightarrow R_L = \frac{Z_0^2 P_{\text{coupled}}}{V_{\text{max}}^2} \tag{1.45}$$

Again, a more interesting formula is the time-averaged power coupled to the line, which in this case reads:

$$\frac{1}{T}\int_0^T P_{\text{coupled}}\, dt = \frac{R_L}{Z_0^2}\frac{1}{T}\int_0^T V_{\text{max}}^2 dt = \frac{R_L}{Z_0^2}\left[1 + |\Gamma_L|\right]^2\left(\frac{|V_L^+|^2}{2}\right) \rightarrow R_L = \frac{2Z_0^2\left\langle P_{\text{coupled}}\right\rangle_t}{|V_{\text{max}}|^2} \tag{1.46}$$

[1] In this approximation, the Gaussian volume only encloses free-space and connects to the transmission line at the short. We assume no antenna near fields, while the transmission line is still allowed to contain reactive power.

[2] Note that V_L^+ is the steady-state forward voltage in the unmatched line evaluated at the load (either the feeder or the resistor-short in our simplified picture), which also accounts for the reactive power, and thus, it is not directly accessible via knowledge of the generator output power alone.

This is the more common way the loading resistance is introduced in the literature. In ASDEX Upgrade, $\langle P_{\text{coupled}} \rangle_t$ is measured by directional couplers in the matched lines feeding each antenna, whereas V_{max} is measured by voltage probes in the unmatched lines. This quantity is central to the discussions presented in **chapters 3** and **4**. It has been used as the main RF diagnostic to study the accessibility of the fast wave under non-axisymmetric plasma conditions, as well as key quantity for the comparison against numerical simulations.
In this context, another common quantity, the voltage standing wave ratio (VSWR), can be defined as:

$$\text{VSWR} = \frac{V_{\text{max}}}{V_{\text{min}}} = \frac{1 + |\Gamma_L|}{1 - |\Gamma_L|} \rightarrow R_L = \frac{Z_0}{\text{VSWR}} \tag{1.47}$$

This quantity is inversely proportional to R_L and describes the matching quality between the antenna-plasma and the circuit with VSWR $\rightarrow$ 1, $+\infty$ as $|\Gamma_L| \rightarrow 0$ (perfect matching), 1 (total reflection).

Chapter 2

Tools used for the study of ICRF Coupling in 3D geometry

In this chapter, we describe the main tools, both experimental and numerical, used in the study of the influence of MPs on ICRF coupling. Within the experimental tools, we present the employed plasma diagnostics, for which a brief explanation of the underlying physical mechanism has been included. These are relevant to the measurements of **Chapter 3**. Within the numerical tools, the used codes for the simulations in **Chapter 4** are described. Particularly, an extensive description of the VMEC and BMW codes is made, due to the novel contributions to these as an outcome of the work in this thesis (i.e. MPI parallelization of the BMW code and divergence-free solution of the induction field over all the considered computational domain).

2.1 Experimental tools and diagnostics

2.1.1 Charge Exchange Recombination Spectroscopy diagnostics

The Charge Exchange Recombination Spectroscopy (CXRS) diagnostic allows the determination of impurity ion temperature, density and velocity from light emitted in charge exchange reactions. Temperatures are obtained from the Doppler width of the emitted light, velocities from the Doppler shift, and densities from the intensity of the emission line. The Neutral Beam Injectors are used as the active source of neutrals for these reactions. ASDEX Upgrade has two core CXRS systems and two edge systems [23]. The core CXRS channels, named "CEZ" and "CUZ", are aligned in toroidal direction (as seen in **figure 2.1(a)**). The edge systems are aligned such that one offers a toroidal view to allow for the determination of toroidal rotation profiles, "CMZ", and the other a poloidal view to allow the determination of the poloidal rotation profile, "CPZ", as seen in **figure 2.1(b)**.

In this thesis, the edge CXRS diagnostics have been used to track the plasma response generated by the application of Magnetic Perturbations, while the core CXRS ones have been used to evaluate parameters of interest, such as the impurity ion temperature, density and plasma collisionality, as described in **Chapter 3**.

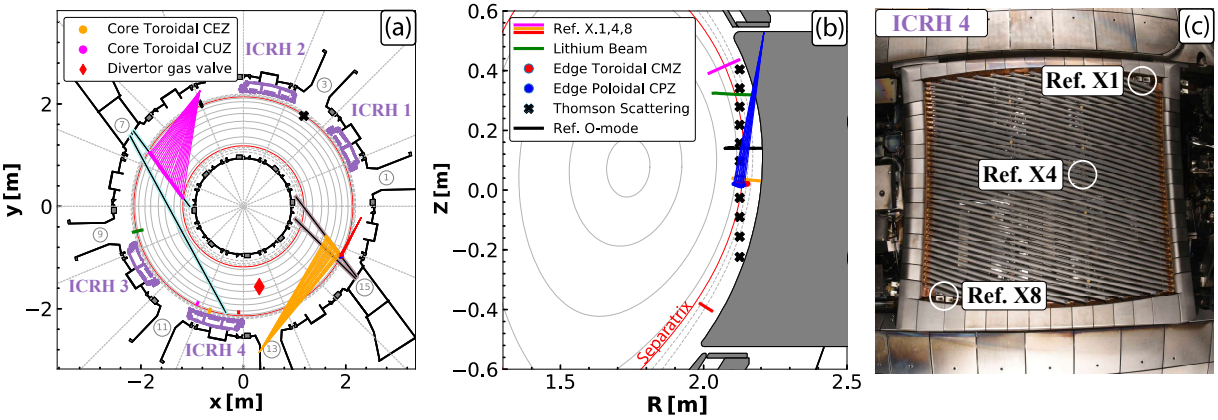

Figure 2.1: (a) Toroidal view of ASDEX Upgrade with used diagnostics: core CXRS channels, lithium beam, Thomson scattering, O-mode reflectometry and ICRF X-mode integrated reflectometry. (b) Poloidal view of ASDEX Upgrade. Displayed are the edge CXRS channels and the same diagnostics aforementioned except core CXRS. (c) In-vessel picture of ICRH4 with positions of embedded X-mode reflectometry.

2.1.2 Lithium Beam diagnostic

The Lithium Beam diagnostic is based on a collisional-radiative principle. Neutral lithium atoms are injected into the plasma region with an energy of $\approx 40\,\mathrm{keV}$. These suffer excitations until fully ionized via collisions with the plasma species. The excited states fall to lower energy ones by photonic emissions that can be tracked with photomultipliers. The most strongly populated state is the Li_{2p} line which decays to the 2s orbital at a wavelength of ~ 671.5 nm [24]. Profiles are measured along the beam propagation path. From the spatial distribution of this line intensity, it is possible to reconstruct the plasma electron density profile.
Since the lithium beam channels span the scrape-off layer (SOL) and beginning of the confined region, it is possible to track the position and density changes of the LCFS and ICRF fast wave R-cutoffs. This has been used in order to evaluate the displacements created by magnetic perturbations in these regions, as well as their radial decay in the SOL.

2.1.3 Reflectometry diagnostics

Reflectometry techniques are used to measure the electron density in a wide variety of plasma conditions. For profile reflectometry, the working principle consists in the measurement of the group delay, $\tau_g = d\phi/d\omega$. Here, ϕ is the phase shift that the wave acquires between being emitted from the antenna and reflected back to the receiver [25], which depends on the plasma refractive index and ω is the wave frequency. The wave is reflected at a plasma cutoff according to the dispersion relation of the used mode. Disregarding the launching method (CW, pulsed, swept, etc.), reflectometer systems can be classified according to the dispersion relation of the launched mode, namely: O-mode reflectometry and X-mode reflectometry. Starting from the characteristic polynomial in **equation 1.25**, and assuming $n_{\parallel} = 0$ here for simplicity, we obtain:

$$\begin{cases} n_\perp^2 = P & \text{O-mode} \quad (2.1a) \\ n_\perp^2 = \dfrac{RL}{S} & \text{X-mode} \quad (2.1b) \end{cases}$$

Cutoffs can be found in surfaces of $n_\perp^2 = 0$. For O-mode this means $\omega = \omega_{p,e}$, whereas for X-mode, the L- and R-cutoffs, often referred to as the lower and upper cutoffs, imply $L = 0, R = 0$. In ASDEX Upgrade both reflectometry types are available. An O-mode reflectometer is installed in the LFS and another one in the HFS [26], providing n_e profiles down to 20 μs. This system probes densities in the $\sim 10^{18}\,\mathrm{m}^{-3} \leq n_e \leq 2 - 3 \times 10^{19}\,\mathrm{m}^{-3}$ range, thus allowing the diagnosis of the plasma pedestal and near SOL. A poloidal X-mode reflectometry array was also installed in 2015-2016 [27, 28] embedded in ICRH4, as can be seen in **figure 2.1(c)**. The probing capabilities of this system depend on the background magnetic field (the R-cutoff is used), and at $B_t = 2.5\,\mathrm{T}$, the system works in the range $\sim 10^{17}\,\mathrm{m}^{-3} \leq n_e \leq 8 \times 10^{18}\,\mathrm{m}^{-3}$, thus allowing the diagnosis of the far SOL, inside the ICRF fast wave coupling region.

Both diagnostics have been used for the study of the displacement of the density layers in the SOL when MPs are applied. The X-mode reflectometry array has also allowed the visualization of the toroidal and (with reduced capabilities) the poloidal structure of the density perturbation in the SOL and its correlation to RF measurements.

2.1.4 Thomson Scattering diagnostic

Thomson scattering is able to measure n_e and T_e by means of scattered laser radiation. T_e is determined from the spectral broadening of the scattered light. n_e is measured from the absolute value of the scattered power. The scattered power per unit solid angle in the frequency range $d\omega$ is:

$$P_{\mathrm{sca}} = P_i r_e^2 \sin^2(\theta) n_e L S(\Delta|k|, \Delta\omega) d\omega \tag{2.2}$$

With P_i the initial laser power, r_e the classical electron radius, θ the angle between the incident and scattered rays, L is the interaction length and $S(\Delta|k|, \Delta\omega)$ is the spectral density function, which is a function of the Fourier spectrum of the fluctuations giving rise to the scattering. Here, $\Delta\omega = \omega_i - \omega_{\mathrm{sca}}$ and $\Delta|k| = |k_i| - |k_{\mathrm{sca}}|$. For a thermal plasma [8]:

$$S(\Delta|k|, \Delta\omega) d\omega = \Gamma(x_e) dx_e + Z_i \left(\frac{\alpha^2}{1 + \alpha^2} \right)^2 \Gamma(x_i) dx_i \tag{2.3}$$

With Z_i the ion atomic number, $\Gamma \sim e^{-x^2}$ the Salpeter function, $x_{e/i} = \Delta\omega / \Delta|k| v_{t,e/i}$ and $\alpha = 1/\Delta|k|\lambda_D$, the scattering parameter. In the scattered spectrum, the first term produces a broad peak with a width of the order of $\sim \Delta|k| v_{t,e}$ and the second a narrow peak with width $\sim \Delta|k| v_{t,i}$. With $\alpha \ll 1$ the first term dominates and T_e can be determined from it.

In ASDEX Upgrade, two Thomson scattering systems are available [29], one in the plasma core and one at the edge. We have used the edge system in order to provide further validation of the density profile measurements by reflectometry and lithium beam, a key component of the fast wave coupling studies presented in **Chapter 3**.

2.1.5 Integrated data analysis (IDA)

The Integrated Data Analysis (IDA) in ASDEX Upgrade, consists of a numerical framework developed to simultaneously process the data from several diagnostics via forward modeling and calibration parameters, in order to yield unified physical quantities and kinetic profiles [30]. A

set of kinetic profiles is first chosen, and each diagnostic is forward modeled to obtain synthetic data. This synthetic data is then compared to the real data measured by the diagnostic, and a probability distribution function is derived. Its maximization provides the best estimate for a given profile, and error propagation can be made with the computed distribution function. Interpretation of such errors is provided by Bayesian analysis:

$$p(n_e, T_e, ...|d_{\mathrm{LIB}}, d_{\mathrm{ECE}}, ...) \propto p(d_{\mathrm{LIB}}|n_e, T_e) \times p(d_{\mathrm{ECE}}|n_e, T_e) \times ... \times p(n_e, T_e) \tag{2.4}$$

Where $p(n_e, T_e, ...|d_{\mathrm{LIB}}, d_{\mathrm{ECE}}, ..)$ is the posterior, $p(d_{\mathrm{LIB}}|n_e, T_e)$, $p(d_{\mathrm{ECE}}|n_e, T_e)$... are the likelihoods of the different diagnostic data to be compatible with the chosen kinetic profiles and $p(n_e, T_e)$ is prior information, such as smoothness, positivity, etc.

This methodology allows to combine redundant diagnostic data and minimize systematic errors. The current drawback stems from the assumption of axisymmetry and ideal MHD, meaning that physical quantities are always assumed constant on a given flux surface. Therefore, IDA has been used in this thesis in order to obtain estimates for physical quantities at given ρ_{pol} positions, such as plasma collisionality or separatrix density. The further 3D analysis of plasma displacements has been performed with the *conventional*[1] diagnostic analysis methodology, in light of the current limitations.

2.2 Numerical tools

2.2.1 The MAKEGRID code

The MAKEGRID code (analogous to the VACFIELD code [31]) computes the vacuum magnetic induction field on a cylindrical grid for various types of coils. The magnetic induction field is computed in Cartesian coordinates and then converted to cylindrical coordinates. For the modeling of ASDEX Upgrade equilibria, the toroidal field component has been assumed axisymmetric, i.e. the toroidal field ripple due to the finite number of toroidal field (TF) coils is neglected. The toroidal field can then be approximated by that of an infinite straight conductor, placed at the symmetry axis, carrying an equivalent current I:

$$B_\phi \approx \frac{\mu_0 I}{2\pi R} = \frac{\mu_0}{2\pi R} \sum_1^{16} I_{\mathrm{TF}} \tag{2.5}$$

with I_{TF} the current in each TF coil. The poloidal field (PF) conductors are used for plasma shaping and control purposes. The ASDEX Upgrade tokamak is composed of 5 pairs of PF coils (OH2, OH3, V1, V2, V3) placed outside the TF conductors, and 1 pair of control coils placed inside the TF conductors (Co) [32]. Furthermore, when reconstructing the plasma equilibrium, the passive stabilization loop (PSL) and the central solenoid (OH1) are also taken into account, which are all modeled in the same way. A scheme of the used coils can be found in **figure 2.2**. All these coils are composed of circular conductors with radius R and vertical position Z. Due to finite radial or vertical extension of some coils, these are modeled by a number m of infinitely thin circular conductors, each having N_i^{wind} windings. For the ASDEX Upgrade tokamak, we use a representation of the poloidal field coils with $m_{\mathrm{total}} = 896$ circular conductors. Each

[1] As in on an individual per-diagnostic basis, rather than with this integrated framework.

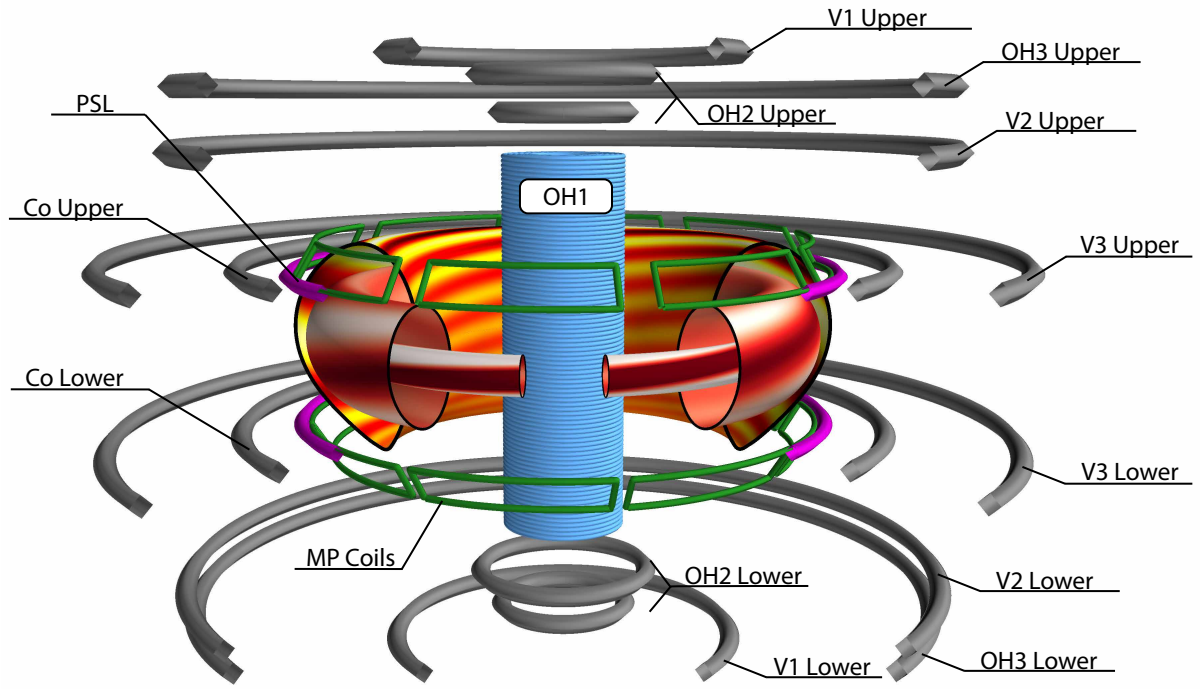

Figure 2.2: Scheme of the coils used in ASDEX Upgrade equilibria modeling. Marked in gray color are the poloidal field coils (V1, V2, V3, OH2 and OH3) and the control coils (Co). In green are the magnetic perturbation coils (MP coils). In magenta, the passive stabilization loop (PSL). The central solenoid (OH1) is plotted in blue color. Three magnetic flux surfaces are added.

circular conductor is then subdivided in L straight filaments. A magnetostatic approximation is used, thus the magnetic induction field is computed from the Biot-Savart law:

$$\vec{B}^{\text{coil}} = \sum_{i=1}^{m} \vec{B}_i^{\text{cond}}, \quad \vec{B}_i^{\text{cond}} = \sum_{j=1}^{L} \vec{B}_{i,j}^{\text{fil}} \tag{2.6}$$

Where:

$$\vec{B}_{i,j}^{\text{fil}} = \frac{\mu_0}{4\pi} I_i^{\text{cond}} \int_0^l \frac{\hat{k}_j \times \left(\vec{r} - \vec{r}_j(l)\right)}{|\vec{r} - \vec{r}_j(l)|^3} |\vec{r}_{j+1} - \vec{r}_j| \tag{2.7}$$

With $\hat{k}_j = (\vec{r}_{j+1} - \vec{r}_j)/|\vec{r}_{j+1} - \vec{r}_j| = d\vec{l}/|d\vec{l}|$ being the unit vector from one straight filament to the next, I_i^{cond} being the current flowing through the conductor i, $I_i^{\text{cond}} = I^{\text{coil}} \left(N_i^{\text{wind}}/N_{\text{coil}}^{\text{wind}}\right)$ with $N_{\text{coil}}^{\text{wind}} = \sum_i N_i^{\text{wind}}$, the total number of windings of the given coil.

The ASDEX Upgrade tokamak is further complemented with 16 in-vessel saddle coils (magnetic perturbation or MP coils, shown in **figure 2.2**) arranged into two poloidally shifted, toroidally distributed, rows of eight coils. The MP coils produce an induction field normal to the coil plane and approximately normal to the plasma surface under standard plasma shaping conditions, i.e. edge optimized configuration (EOC), low triangularity.
The numerical implementation of the MP coils is done by connecting small straight filaments in space, the same way it is done for the poloidal field coil conductors. The magnetic induction field is computed by applying the Biot-Savart law.

2.2.2 The DESCUR code

The DESCUR code [33] computes an optimized Fourier series representation of a given closed surface in $\mathbb{R}^3$ space. The power spectrum of the surface and q-order moment are defined as:

$$\begin{cases} S_p(m) = m^p \sum_n (X_{mn}^2 + Y_{mn}^2) \quad \forall p \geq 0 & \text{(2.8a)} \\ M(p,q) = \dfrac{\sum_m m^q S_p(m)}{\sum_m S_p(m)} & \text{(2.8b)} \\ X(\theta,\phi) = \sum X_{mn} \cos(m\theta - n\phi), \quad Y(\theta,\phi) = \sum Y_{mn} \sin(m\theta - n\phi) & \text{(2.8c)} \end{cases}$$

where $M(p,q)$ represents a measure of the spectral extent of X_{mn} and Y_{mn}, defining a given coordinate in real space (see **equation 2.16**). A variational principle is derived which allows the minimization of $M(p,q)$, i.e., $\delta M = 0 \leftrightarrow I(\theta,\phi) = 0$, where $I = f(X_{mn}, Y_{mn}, p, q, M, \theta, \phi)$. This introduces an additional number of constraints between X_{mn} and Y_{mn}, such that $\delta M = 0$, thus allowing the condensation of the spectral description. For a given curve, Fourier harmonics are sought by least squares minimization plus the spectral condensation condition:

$$W_T = \frac{1}{2} \sum_i \left[(X(\theta,\phi) - x_i)^2 + (Y(\theta,\phi) - y_i)^2 \right] + \epsilon M \tag{2.9}$$

with ϵ chosen to balance the contributions from the first and second terms. The forces which minimize this energy are obtained as its gradient $F = -\nabla W_T$, and are proportional to $F \propto ((X(\theta,\phi) - x_i), (Y(\theta,\phi) - y_i), I)$, such that $F = 0 \leftrightarrow X(\theta,\phi) = x_i, Y(\theta,\phi) = y_i$ (condition for a correct curve fit) and $I = 0$ (condition for spectral condensation).

Since a converged 2D equilibrium from CLISTE is used as input for NEMEC, its boundary[2] needs to be expressed as a Fourier series for the cylindrical coordinates $\{R, Z\}$ with a finite number of harmonics. The DESCUR code provides just that from a set of sampled points x_i, y_i along the surface. This spectral condensation is also applied in the NEMEC code (see next section). If the first term on W_T is changed by the ideal MHD energy functional, one obtains a set of force equations (**equations 2.15b**) which minimize it. Since spectral condensation is also desired, as it accelerates convergence, the second term ϵM is also appended to the ideal MHD energy functional, although it will not be explicitly stated in the forthcoming derivations.

2.2.3 The NEMEC (PARVMEC) code

Ideal MHD description. Formulation of the energy principle.

The PARVMEC code [34] is an MPI parallelization of the NEMEC code [35], that does not include further physics. We will thus introduce in this section the physical foundation of the NEMEC code, and will refer to PARVMEC in the remainder of this thesis as the usage of its parallel counterpart. NEMEC is a composition of two codes: VMEC (**V**ariational **M**oments **E**quilibrium **C**ode) plus NESTOR (**NE**umann **S**olver for **TO**roidal **R**egions), and it is used to compute 3D ideal, non-linear, plasma MHD equilibria. Therefore, the NEMEC code works under the constraint of preserving nested flux surfaces. Analogously to the derivation of the

[2]The separatrix, which contains an X-Point, cannot be treated in this manner. We will, therefore, consider the boundary to be an inner flux surface which toroidal flux is as close as possible to the separatrix one.

single-fluid MHD equations in **section 1.2**, equilibrium states are sought with zero resistivity ($\sigma \to \infty$) and neglecting flow ($\vec{v} = 0$), such that the momentum balance and relevant Maxwell equations read:

$$\begin{cases} \vec{F} = \vec{j} \times \vec{B} - \vec{\nabla} p \, (= 0 \text{ in equilibrium}) & \text{(2.10a)} \\ \vec{\nabla} \cdot \vec{B} = 0 & \text{(2.10b)} \\ \vec{\nabla} \times \vec{H} = \vec{j} & \text{(2.10c)} \end{cases}$$

By considering the plasma to be subject to adiabatic constraints, the potential energy of the system can then be written as [36]:

$$\mathcal{W} = \int_{\Omega_p} \left[\frac{|\vec{B}|^2}{2\mu_0} + \frac{p}{\gamma - 1} \right] dV \tag{2.11}$$

Where Ω_p is the plasma domain, $|\vec{B}|^2/2\mu_0$ is the magnetic energy density and $p/(\gamma - 1)$ is the fluid energy density with γ being the adiabatic constant, i.e. the ratio of the specific heats of the fluid. A stationary solution of minimum energy, such that $\dot{\mathcal{W}} = 0$, is sought. In order to exclude the trivial solution ($p = 0$, $\vec{B} = 0$), the plasma is bounded to preserve an initially prescribed magnetic flux inside every flux surface and the total number of particles, i.e. mass conservation. To ensure the first condition, the magnetic induction may be written as a function of Euler potentials / Clebsch notation [37, 38]:

$$\begin{cases} \vec{B} = \vec{\nabla} s \times \vec{\nabla} \nu \quad / \, \nu = \psi' \theta - \chi' \xi + \lambda & \text{(2.12a)} \\ B^s = 0 & \text{(2.12b)} \\ B^\theta = \dfrac{1}{\sqrt{g}} (\chi' - \partial_\xi \lambda) & \text{(2.12c)} \\ B^\xi = \dfrac{1}{\sqrt{g}} (\psi' + \partial_\theta \lambda) & \text{(2.12d)} \end{cases}$$

Which is the most general form of $\vec{B}$ that ensures $\vec{\nabla} \cdot \vec{B} = 0$, $\vec{B} \cdot \vec{\nabla} \psi = 0$. We have introduced here the radial coordinate $s = \psi_\mathrm{N} = \psi / \psi_\mathrm{LCFS} \in [0, 1]$, where ψ_LCFS is the total toroidal flux enclosed by the last closed magnetic surface. Likewise, we define the magnetic flux coordinates $\{s, \theta, \xi\}$, the magnetic induction contravariant components $\{B^s, B^\theta, B^\xi\}$, the poloidal flux $2\pi\chi(s)$, and the toroidal flux $2\pi\psi(s)$ enclosed by the flux surface "s". The prime denotes the radial derivative ∂_s, and $\sqrt{g} = (\vec{\nabla} s \cdot \vec{\nabla} \theta \times \vec{\nabla} \xi)^{-1}$ is the Jacobian of the transformation between toroidal and magnetic flux coordinates. The angle $\theta^* = \theta + \lambda(\rho, \theta, \xi)$ is the straight field-line angle that ensures that the rotational transform is dependent only on the s coordinate, i.e., $\iota = \iota(s)$. The retention of the λ parameter is important, as it ensures the fulfillment of the MHD equations when the coordinates are expanded in Fourier series with a finite number of harmonics (see Solov'ev equilibrium example in [35]).

In order to secure the second condition, we look for an expression that conserves mass. If ρ_m is the density of a fluid element, the mass of that element is to be an invariant of motion, such that $\rho_m dV = dm$. Since we have assumed the fluid to be adiabatic, this condition can easily be transformed into $p^{1/\gamma} dV = \text{const}$, for each fluid element. In order to obtain a more general condition for the whole plasma, we define the following flux surface quantity:

$$M(s) = \int_{\Omega_\rho} p^{1/\gamma} dV = \text{const.} \ \forall \Omega_\rho \in \Omega_p \tag{2.13}$$

With $M(s)$ being an invariant proportional to the total mass contained within a given flux surface Ω_ρ. $M(s)$ is incorporated into the description of the pressure profile, thus representing mass conservation.

A Fourier description will be now introduced in order to solve for $\dot{\mathcal{W}} = 0$. Here, $\vec{x} = \{R, \phi, Z\}$ assume the role of dependent variables, whereas the magnetic coordinates $\vec{\alpha} = \{s, \theta, \xi\}$ are the independent ones. First, the variation of $\mathcal{W}$ is performed with respect to time[3]:

$$\frac{d\mathcal{W}}{dt} = \int_{\Omega_p} \left[-\left(\frac{|B|^2}{2\mu_0} + p \right) \partial_t \sqrt{g} + \frac{1}{\mu_0 \sqrt{g}} \left(b_R \dot{b_R} + R^2 b_\phi \dot{b_\phi} + b_z \dot{b_z} + R b_\phi^2 \dot{R} \right) \right] d^3\alpha \tag{2.14}$$

with $b_j = \sqrt{g}(\vec{B} \cdot \vec{\nabla} x_i)$. By plugging each of the derivatives in, one obtains:

$$\begin{cases} \dfrac{d\mathcal{W}}{dt} = -\displaystyle\int_{\Omega_p} F_i \dot{x_i} \, d^3\alpha - \int_{\Omega_p} F_\lambda \dot{\lambda} \, d^3\alpha - \int_{s=1} \left|\sqrt{g}\right| \frac{\partial s}{\partial x_i} \left(\frac{|B|^2}{2\mu_0} + p \right) \dot{x_i} d\theta d\xi & \text{(2.15a)} \\ F_i = -\partial_{\alpha_j} \left[\left|\sqrt{g}\right| \dfrac{\partial \alpha_j}{\partial x_i} \left(\dfrac{|B|^2}{2\mu_0} + p \right) \right] + \dfrac{\left|\sqrt{g}\right|}{\mu_0} \vec{\nabla} \cdot \left[\left(g_{ii} \vec{B} \cdot \vec{\nabla} x_i \right) \vec{B} \right] & \text{(2.15b)} \\ \qquad + \delta_{i1} \dfrac{\left|\sqrt{g}\right|}{R} \left(\dfrac{|B|^2}{2\mu_0} + p - \dfrac{1}{\mu_0} R^2 (\vec{B} \cdot \vec{\nabla} \phi)^2 \right) \\ F_\lambda = \dfrac{\psi'}{\mu_0} \left(\partial_\theta B_\xi - \partial_\xi B_\theta \right) & \text{(2.15c)} \end{cases}$$

Where Einstein summation is implied and $g_{11} = g_{33} = 1$, $g_{22} = R^2$, the toroidal metric tensor elements. The last term in **equation 2.15a** corresponds to the energy change due to deformations of the plasma boundary. For a fixed boundary equilibrium, it is readily seen that a stationary solution $\dot{\mathcal{W}} = 0$ is achieved when $F_i = F_\lambda = 0$, which corresponds to $\vec{F} = 0$ in **equation 2.10a**. Here the choice $\phi = \xi$ is made, which reduces the Jacobian to 2 dimensions and implies $F_\phi = 0$, thus $F_i = \{F_R, F_Z\}$. This allows to define the coordinate system $\{R, \lambda, Z\}$, where λ now represents a coordinate. **Equation 2.15a** can be solved for, while simplified, through a Fourier description of the coordinate system, such that:

$$x_j = \sum_{mn} X_j^{mn}(s) \, e^{i(m\theta - n\xi)} \quad \forall j = \{R, \lambda, Z\} \tag{2.16}$$

Where $X_j^{mn} \in \mathbb{C}$ are the Fourier harmonic amplitudes. From this, the energy principle (neglecting the boundary terms) is reduced to:

$$\begin{cases} \dfrac{d\mathcal{W}}{dt} = -\displaystyle\sum_{mn} \int (F_j^{mn})^* \dot{X_j}^{mn} V' ds & \text{(2.17a)} \\ F_j^{mn} = \dfrac{1}{V'} \displaystyle\iint_{\theta,\xi} F_j e^{-i(m\theta - n\xi)} d\theta d\xi & \text{(2.17b)} \end{cases}$$

[3]Here, t, is a fictitious time coordinate.

The descent rate of **equation 2.17a** is $\int_s (F_j^{mn})^* \dot{X}_j{}^{mn} dV$, which is to be maximized. Using the Schwarz-Cauchy-Bunyakovsky inequality, one can see that this descent rate is bounded:

$$\int_s \left| (F_j^{mn})^* \dot{X}_j{}^{mn} \right|^2 dV \leq \int_s \left| F_j^{mn} \right|^2 dV \int_s \left| \dot{X}_j{}^{mn} \right|^2 dV \tag{2.18}$$

With equality pertaining if and only if both terms are linearly dependent, $\dot{X}_j{}^{mn} = k F_j^{mn}$. By taking $k = 1$, the equality holds and the descent rate is maximized, thus the descent path and maximum descent rate are:

$$\begin{cases} F_j^{mn} = \dot{X}_j{}^{mn} & \text{(2.19a)} \\ \dot{\mathcal{W}} = -\sum_{mn} \int |F_j^{mn}|^2 V' ds & \text{(2.19b)} \end{cases}$$

Computation of plasma currents and ideal MHD force balance.

The non-linear calculation of the plasma currents in VMEC is an important aspect of this thesis. These are used in the BMW code (see **section 2.2.4**) to reconstruct the magnetic induction in an arbitrary domain, inside and beyond the LCFS. We present in this section how these are directly obtained from the computed VMEC induction fields, and how they affect the numerical convergence of the ideal MHD force balance.
In VMEC, the computation of the covariant and contravariant field components is possible once the Jacobian and λ function are known. The force balance in **equation 2.10a** can then be evaluated through the computation of the plasma currents. We will assume straight field-line angle coordinates for this derivation. Starting from Ampere's law:

$$\vec{\nabla} \times \vec{H} = \vec{j} \rightarrow \left(\vec{\nabla} \times \vec{H} \right)^k = \frac{1}{\sqrt{g}} \epsilon^{ijk} \nabla_i H_j \vec{R}_k = j^k \vec{R}_k \tag{2.20}$$

with ϵ^{ijk} the Levi-Civita symbol, $\nabla_i H_j$ the covariant derivative of the covariant induction field components and $\vec{R}_k$ the covariant local basis vectors. Here, H_j includes both the plasma field and the vacuum field contributions. In order to compute the radial force balance, the field components and current densities can be flux-surface averaged, i.e.,

$$\begin{aligned} \frac{1}{\partial_s V(s)} \iint_{\theta,\phi} j^k \sqrt{g} d\theta d\phi &= \frac{1}{\partial_s V(s)} \iint_{\theta,\phi} \frac{1}{\sqrt{g}} \epsilon^{ijk} \nabla_i H_j \sqrt{g} d\theta d\phi \\ \rightarrow \left\langle j^k \right\rangle (s) &= \left\langle \frac{1}{\sqrt{g}} \epsilon^{ijk} \nabla_i H_j \right\rangle \end{aligned} \tag{2.21}$$

where $V(s)$ is the volume of the flux surface s. The flux-surface averaged current can only be identified with the plasma current, and has no contribution from the vacuum field since:

$$\begin{cases} \left\langle j^k \right\rangle (s) = \frac{1}{\partial_s V(s)} \iint_{\theta,\phi} \left(j^k_{\text{vac}} + j^k_{\text{pl}} \right) \sqrt{g} d\theta d\phi & \text{(2.22a)} \\ \frac{1}{\partial_s V(s)} \iint_{\theta,\phi} j^k_{\text{vac}} \sqrt{g} d\theta d\phi = I^{k,\text{vac}}_{\text{net}} = 0 & \text{(2.22b)} \end{cases}$$

That is, the vacuum field cannot produce a net current in the flux surface[4] (even though we may identify a corresponding local surface current). This point is discussed in more detail within the virtual casing principle explanation in **section 2.2.5**. Thus, one can compute the flux-surface averaged current components as:

$$\left\langle j^{\theta}\right\rangle = \left\langle \frac{1}{\sqrt{g}}\partial_{\phi}H_{s}\right\rangle - \left\langle \frac{1}{\sqrt{g}}\partial_{s}H_{\phi}\right\rangle = -\left\langle \frac{1}{\sqrt{g}}\partial_{s}H_{\phi}\right\rangle \tag{2.23a}$$

$$\left\langle j^{\phi}\right\rangle = \left\langle \frac{1}{\sqrt{g}}\partial_{s}H_{\theta}\right\rangle - \left\langle \frac{1}{\sqrt{g}}\partial_{\theta}H_{s}\right\rangle = \left\langle \frac{1}{\sqrt{g}}\partial_{s}H_{\theta}\right\rangle \tag{2.23b}$$

where $\int_{\theta/\phi}\partial_{\theta/\phi}H_{s}\,d\theta/d\phi = 0$ due to periodicity, and the covariant derivative has been transformed into partial derivatives owing to the symmetry of Christoffel symbols [39]. Having the plasma currents, the radial force balance can be computed as:

$$\vec{j}\times\vec{B} = \vec{\nabla}p \rightarrow \vec{j}\times\vec{B} = \sqrt{g}\epsilon_{ijk}j^{i}B^{j}\vec{R}^{k} = \sqrt{g}\left(j^{\theta}B^{\phi} - j^{\phi}B^{\theta}\right)\vec{R}^{s} = \partial_{s}p\vec{R}^{s} \tag{2.24a}$$

Using **equation 2.12** to express the contravariant induction field as a function of the toroidal and poloidal fluxes:

$$\sqrt{g}\left(j^{\theta}\frac{1}{\sqrt{g}}(\psi' + \partial_{\theta}\lambda) - j^{\phi}\frac{1}{\sqrt{g}}(\chi' - \partial_{\xi}\lambda)\right) = \partial_{s}p \tag{2.25}$$

From this relation, the flux-surface averaged residual of the ideal MHD force is computed. Noting that $\lambda = 0$ in this coordinate system:

$$\begin{aligned}
&\frac{\psi'(s)}{\partial_{s}V(s)}\iint_{\theta,\phi}j^{\theta}\sqrt{g}d\theta d\phi - \frac{\chi'(s)}{\partial_{s}V(s)}\iint_{\theta,\phi}j^{\phi}\sqrt{g}d\theta d\phi = \frac{1}{\partial_{s}V(s)}\iint_{\theta,\phi}\partial_{s}p\sqrt{g}d\theta d\phi \\
&\rightarrow \psi'(s)\left\langle j^{\theta}\right\rangle - \chi'(s)\left\langle j^{\phi}\right\rangle = \partial_{s}p \\
&\rightarrow -\psi'(s)\left\langle \frac{1}{\sqrt{g}}\partial_{s}H_{\phi}\right\rangle - \chi'(s)\left\langle \frac{1}{\sqrt{g}}\partial_{s}H_{\theta}\right\rangle - \partial_{s}p = \langle F_{\text{residual}}\rangle
\end{aligned} \tag{2.26}$$

where we have applied $\partial_{s}V(s) = \oiint_{\theta,\phi}\sqrt{g}d\theta d\phi$. Here, $\int F^{2}_{\text{residual}}d^{3}\alpha$, is the real-space magnetic coordinate analog to the right hand side of **equation 2.19b**. It is this quantity that we refer to as the force residual (f_{tol}) in the remainder of the text and that serves as the convergence criterion in VMEC. Its units, albeit no further stated, are taken to be $N\cdot m/s$.

Boundary cases. NESTOR extension.

Two situations can exist at the boundary, it is either kept fixed, thus producing a fixed-boundary simulation, or it is allowed to evolve, thus producing a free-boundary simulation. In the former case, the retention of the λ parameter allows to keep constant the Fourier coefficients at the plasma boundary, such that:

$$X^{mn}_{j}(s=1,t) = X^{mn}_{j}(s=1,0)\ \forall t\ ,\forall j = 1,3 \tag{2.27}$$

[4] We understand $I^{k,\,\text{vac}}_{\text{net}}$ as a net current that would contribute to the vacuum field outside the plasma equilibrium, and thus must be = 0 (the vacuum field must originate uniquely from the external coils). It is, of course, possible to create a net current in the flux surface by means of transformer action. We understand this as contributing to j^{k}_{pl}.

In the latter case, two conditions need to be met [40]:

1. Pressure continuity: The pressure must be constant across the plasma-vacuum interface, $\frac{|\vec{B}_p|^2}{2\mu_0} + p = \frac{|\vec{B}_{\text{ext}}|^2}{2\mu_0}$, where $\vec{B}_{\text{ext}}$ is the magnetic induction field in the exterior region. This external field includes the contribution from the vacuum field produced by the external coils, and that produced by the plasma currents.

2. The external induction field must satisfy the Neumann condition $\vec{B}_{\text{ext}} \cdot d\vec{\Sigma}_p = 0$, where $d\vec{\Sigma}_p$ is the normal exterior vector to $\partial\Omega_p$. This condition states that no normal component of the magnetic induction external field exists at the plasma-vacuum interface. The reason is intuitive by the Poincaré-Hopf theorem [11], given that at this boundary a flux surface lies.

The non-linear nature of the NEMEC code stems from the self-consistent calculation of the external field $\vec{B}_{\text{ext}}$ at the plasma boundary $\partial\Omega_p$, given the external coils vacuum field and the plasma currents. Generally, the initial external induction field will not be tangent to the plasma boundary, that is, it will not satisfy the Neumann condition. To prevent this, a scalar magnetic potential can be added, such that:

$$\vec{B}_{\text{ext}} = \vec{B}_0 + \vec{\nabla}\Phi, \text{ such that } \left(\vec{B}_0 + \vec{\nabla}\Phi\right) \cdot d\vec{\Sigma}_p = 0 \tag{2.28}$$

With $\vec{B}_0$ being the initial induction field and Φ the magnetic scalar potential. This scalar potential is consistently computed during NEMEC iterations. Since Φ is a harmonic function, $\vec{\nabla}^2\Phi = 0$, we can use Green's third identity to determine it on the plasma boundary:

$$\Phi(x) = \frac{1}{2\pi}\left[\oint_{\partial\Omega_p} G(x-x')\partial_{\vec{n}}\Phi(x')\, d\partial\Omega_p - \oint_{\partial\Omega_p} \partial_{\vec{n}} G(x-x')\Phi(x')\, d\partial\Omega_p\right] \tag{2.29}$$

Where $\partial_{\vec{n}}$ is the normal to the plasma surface directional derivative, $G(x-x')$ is the Green's function associated with the Laplace operator and $\partial_{\vec{n}}\Phi(x')$ is directly evaluated from the Neumann condition, **equation 2.28**, $\partial_{\vec{n}}\Phi = -\vec{B}_0 \cdot d\vec{\Sigma}_p$. When the boundary is expressed as a Fourier summation, such as **equation 2.16**, the scalar potential can be decomposed in Fourier harmonics with the following ansatz:

$$\Phi(\theta, \phi) = \sum_{mn} \Phi_{mn}\, e^{i(m\theta - n\phi)} \tag{2.30}$$

The Fourier expanded **equation 2.29** is solved by the NESTOR code [41]. The self-consistent calculation of Φ allows determining the final equilibrium in a non-linear fashion. The pressure continuity condition is then incorporated in the discrete representation of the MHD forces, and uses the Φ potential in every iteration. The leading term for the radial force can be seen to be:

$$F_R^N = \frac{-2}{\Delta s}\left(\partial_\theta Z^N P^N - \partial_\theta Z^{N-1/2} P^{N-1/2}\right) \tag{2.31}$$

With $P = R\left(|\vec{B}|^2/2\mu_0 + p\right)$ and $P^N = R^N\left(|\vec{B}_{\text{ext}}|^2/2\mu_0\right)$. It is thus seen that as $\Delta s \to 0$ (and the number of Fourier harmonics increases to infinity), pressure continuity is met.

2.2.4 The BMW code

The BMW (**B**iot-Savart **M**agnetic **V**MEC **V**ector potential) code[5] is used to calculate the magnetic induction field inside and outside the confined region of an MHD equilibrium. It takes into account both plasma currents and the vacuum induction field from external coils. The code is directly coupled to PARVMEC, thus allowing to *extend* the resulting equilibrium outside the last closed flux surface, which is a fundamental step for scrape-off layer transport studies. BMW calculates the magnetic vector potential on a cylindrical grid, and then obtains the magnetic induction field as $\vec{B} = \vec{\nabla} \times \vec{A}$. Due to this, BMW produces inherently divergence-free $\vec{B}$-fields, since $\vec{\nabla} \cdot \left(\vec{\nabla} \times \vec{A}\right) = 0$ (see discussion in **section 2.2.5**). This feature allows its usage with transport codes such as EMC3-EIRENE, which depend on a pre-calculation of the background magnetic induction field that must be continuous across the separatrix, in order to avoid non-physical behavior.

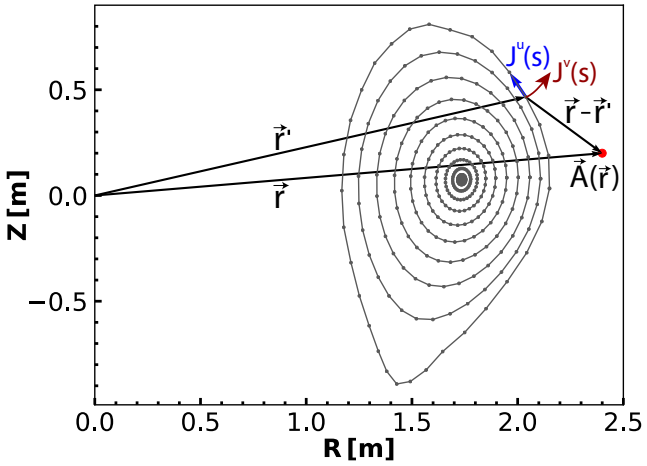

Figure 2.3: Scheme for the integration of **equation 2.34** in BMW.

Starting from a magnetostatic description, in which plasma and coil currents are in equilibrium, it is straightforward to derive from Maxwell equations:

$$\vec{\nabla}^2 \vec{A} = -\mu \vec{j} \tag{2.32}$$

where the Coulomb gauge is used. This Poisson equation can be solved by noting that the Green's function associated with the Laplace operator takes the form:

$$G(\vec{r}, \vec{r}\,') = \frac{-1}{4\pi |\vec{r} - \vec{r}\,'|} \tag{2.33}$$

This leads to the main quantity computed in BMW, the solution of **equation 2.32**:

$$\vec{A}(\vec{r}\,) = \frac{\mu_0}{4\pi} \iiint_{\Omega_p} \frac{\vec{j}(\vec{r}\,')}{|\vec{r} - \vec{r}\,'|} d^3\vec{r}\,' \tag{2.34}$$

Where $\vec{j}(\vec{r}\,')$ is the flux surface current density at $\vec{r}\,'$ and the integration is performed over the plasma domain Ω_p. A scheme of the integration for an ASDEX Upgrade equilibrium can be seen in **figure 2.3**. In order to avoid the singularity produced where $|\vec{r} - \vec{r}\,'| \approx 0$ for a constant $d^3\vec{r}\,'$, the currents are evaluated only at interleaved toroidal planes with those where the integral is computed. This extra toroidal spacing helps to avoid the singularity.
The total magnetic vector potential is the summed contribution from plasma currents and vacuum field:

$$\begin{cases} \vec{A}_T(\vec{r}\,) = \dfrac{\mu_0}{4\pi} \iiint_{\Omega_p} \dfrac{\vec{j}(\vec{r}\,')}{|\vec{r} - \vec{r}\,'|} d^3\vec{r}\,' + \vec{A}_v(\vec{r}\,) & \text{(2.35a)} \\ \vec{B}(\vec{r}\,) = \vec{\nabla} \times \vec{A}_T(\vec{r}\,) & \text{(2.35b)} \end{cases}$$

[5] BMW is a code originally written by Mark Cianciosa, Oak Ridge National Laboratory.

The Fourier harmonics of the current densities are computed according to the non-flux surface averaged version of **equations 2.23** and then summed in normal fashion:

$$\begin{cases} J^u(s,\theta\,\phi) = \sum_{mn} J^{u,c}_{mn}(s)\cos(m\theta - nN_p\phi) + J^{u,s}_{mn}(s)\sin(m\theta - nN_p\phi) & \text{(2.36a)} \\ J^v(s,\theta\,\phi) = \sum_{mn} J^{v,c}_{mn}(s)\cos(m\theta - nN_p\phi) + J^{v,s}_{mn}(s)\sin(m\theta - nN_p\phi) & \text{(2.36b)} \end{cases}$$

where $\{m,n\}$ are the poloidal and toroidal mode numbers, N_p is the number of field periods, $J^{u,c}_{mn}, J^{u,s}_{mn}$ are the cosine and sine amplitudes of the contravariant poloidal current harmonics and $J^{v,c}_{mn}, J^{v,s}_{mn}$ are the cosine and sine amplitudes of the contravariant toroidal current harmonics.

The BMW code has been used with PARVMEC ASDEX Upgrade equilibria for the first time during the work carried out in this Ph.D. thesis. A new MPI implementation of the code was necessary, in order to meet the wall-clock time limit of 24h in the DRACO cluster at IPP Garching. Extensive development and testing led to a new code version capable of MPI + OMP parallelization.

2.2.5 The MFBE and EXTENDER codes. Comparison against BMW

A word on magnetic induction divergence must now be raised. In addition to BMW, there currently exist two more codes that compute the resultant induction field outside the LCFS arising from the superposition of the vacuum field and the PARVMEC solution. These are the MFBE [42] and EXTENDER [43] codes. These codes, based on the virtual casing principle [44, 45], calculate the magnetic induction outside the confined region directly via a surface integral:

$$\begin{cases} \vec{B}(\vec{r}\,) = \frac{\mu_0}{4\pi}\iint \frac{\vec{\mathcal{K}}_s \times (\vec{r}-\vec{r}\,')}{|\vec{r}-\vec{r}\,'|^3} d\vec{A}' + \frac{\mu_0}{4\pi}\iint \sigma_{\text{dipole}}\frac{(\vec{r}-\vec{r}\,')}{|\vec{r}-\vec{r}\,'|^3} d\vec{A}' & \text{(2.37a)} \\ \vec{\mathcal{K}}_s = \hat{n}\times\vec{H}(s=1) & \text{(2.37b)} \\ \sigma_{\text{dipole}} = \hat{n}\cdot\vec{H}(s=1) & \text{(2.37c)} \end{cases}$$

Where the integration surface, $d\vec{A}'$, must toroidally enclose the plasma, $\hat{n}$ is the unitary vector normal to it and $\vec{\mathcal{K}}_s$ is an equivalent surface current density flowing through it. The term σ_{dipole} is a dipole moment density that can be included if the surface of integration is not a flux surface (otherwise $\hat{n}\cdot\vec{H}(s=1) = 0$ by definition). The main advantage of this method is the obvious computational acceleration that evaluating a surface integral has, in opposition to computing a full volume integral such as **equation 2.34**. The main drawback of these codes resides on the violation of $\vec{\nabla}\cdot\vec{B} = 0$ across the plasma boundary. In MFBE, the total magnetic induction is computed in two steps: first, for grid points inside the PARVMEC domain, the PARVMEC solution is linearly interpolated between neighboring flux surfaces. For points outside the PARVMEC domain, the virtual casing principle and the Biot-Savart vacuum field are used. For the former, the PARVMEC magnetic induction solution at the last radial half-grid point[6] needs first to be extrapolated to the last closed flux surface to obtain $\vec{H}(s=1)$. Then, this magnetic induction is used to evaluate the surface current which is used in **equation 2.37b**. This already presents the first problem, namely, two different numerical methods are used to compute the fields in different parts of the domain which are meant to connect smoothly. The second problem that

[6]PARVMEC uses 2 radial grids to solve the discrete MHD force equations.

arises is the accuracy of numerical integration of **equation 2.37a**. For points that are very close to the integration surface, $|\vec{r} - \vec{r}\,'|^3$ diverges strongly, with a $1/r^2$ trend in opposition to the $1/r$ behavior of **equation 2.34**. This issue can be somewhat alleviated with an adaptive grid for points lying very close to the integration surface, up to some limit. It is crucial that the behavior of this integral is captured correctly; the surface current in **equation 2.37b** is calculated from the total induction PARVMEC field, which has the contribution from the plasma and vacuum fields:

$$\vec{\mathcal{K}}_s = \hat{n} \times \vec{H}(s=1) = \hat{n} \times \left(\vec{H}^{\text{plasma}} + \vec{H}^{\text{vacuum}}\right)_{s=1} = \vec{\mathcal{K}}_s{}^{\text{plasma}} + \vec{\mathcal{K}}_s{}^{\text{vacuum}} \tag{2.38}$$

Since the vacuum sources (coils) are outside the equilibrium, $\iint_{s,\theta} \vec{\mathcal{K}}_s{}^{\text{vacuum}} d\vec{S} = I_\phi^{\text{vac, net}} = 0$, and only the plasma current $\vec{\mathcal{K}}_s{}^{\text{plasma}}$ should contribute to the field outside. However, there is no guarantee this is the case when the integral is evaluated numerically, especially for points lying very close to the boundary surface. The third and most important problem arises from the fact that the PARVMEC solution is an approximation constrained by the usage of a finite resolution, and smooth kinetic profiles (instead of discontinuous jumps as used in other codes [46]). In the more numerically demanding case of non-axisymmetric equilibria with rational flux surfaces, this results in a finite violation of the force balance, **equation 2.10a**, which translates to a nested solution from the PARVMEC fields point of view, but a non-nested one from the external field point of view ($\Phi \neq 0$ in **equation 2.28**). Therefore, when one preserves the original PARVMEC solution inside the boundary domain, no smooth transition is possible across the LCFS. For all these reasons, one finds that $\vec{\nabla} \cdot \vec{B} \neq 0$ across the plasma boundary $\partial\Omega_p$.
In EXTENDER, a virtual casing principle is utilized for both, the inner plasma domain (which is used to remove the approximated vacuum field), and the external domain (which gives the field contribution from the approximated plasma currents). Then, the real vacuum field from the Biot-Savart calculation of the external coils is imposed. This approach avoids the two-method problem of MFBE, but is still acutely affected by the accuracy requirements of **equation 2.37a**. Hence, despite constructing a different solution than PARVMEC inside the inner domain (that one would expect to be divergence-free), this method also results in $\vec{\nabla} \cdot \vec{B} \neq 0$ at $\partial\Omega_p$.
BMW addresses the problem by a direct calculation of the magnetic vector potential, performed the same way at every point, at the expense of having to evaluate a computationally demanding volume integral. Since BMW does not preserve the nested field solution, unlike MFBE, but uses the asymptotically approximated (in the sense of having finite resolution both in the radial grid and used number of Fourier harmonics) plasma currents and flux surfaces geometry, magnetic islands and stochastic regions appear in non-axisymmetric equilibria with rational flux surfaces[7]. However, in contrast with EXTENDER, the fulfillment of $\vec{\nabla} \cdot \vec{B} = 0$ is analytically enforced simultaneously for the whole computational domain.

In order to illustrate this, an ASDEX Upgrade PARVMEC equilibrium was extended with the three methods: BMW, EXTENDER virtual casing (VC), and EXTENDER used in "MFBE" mode. A 3D magnetic perturbation was applied in order to break the toroidal symmetry and showcase the development of islands at rational flux surfaces. The simulation parameters were kept modest, as we only intend to show the main differences between the three methods: $n = 8$ toroidal harmonics, $m = 22$ poloidal harmonics and $n_s = 201$ flux surfaces were employed. The vacuum field resolution was $\{n_r = 256, n_z = 512, n_\phi = 180\}$ and the equilibrium was converged

[7] A more detailed discussion follows in **Chapter 4**

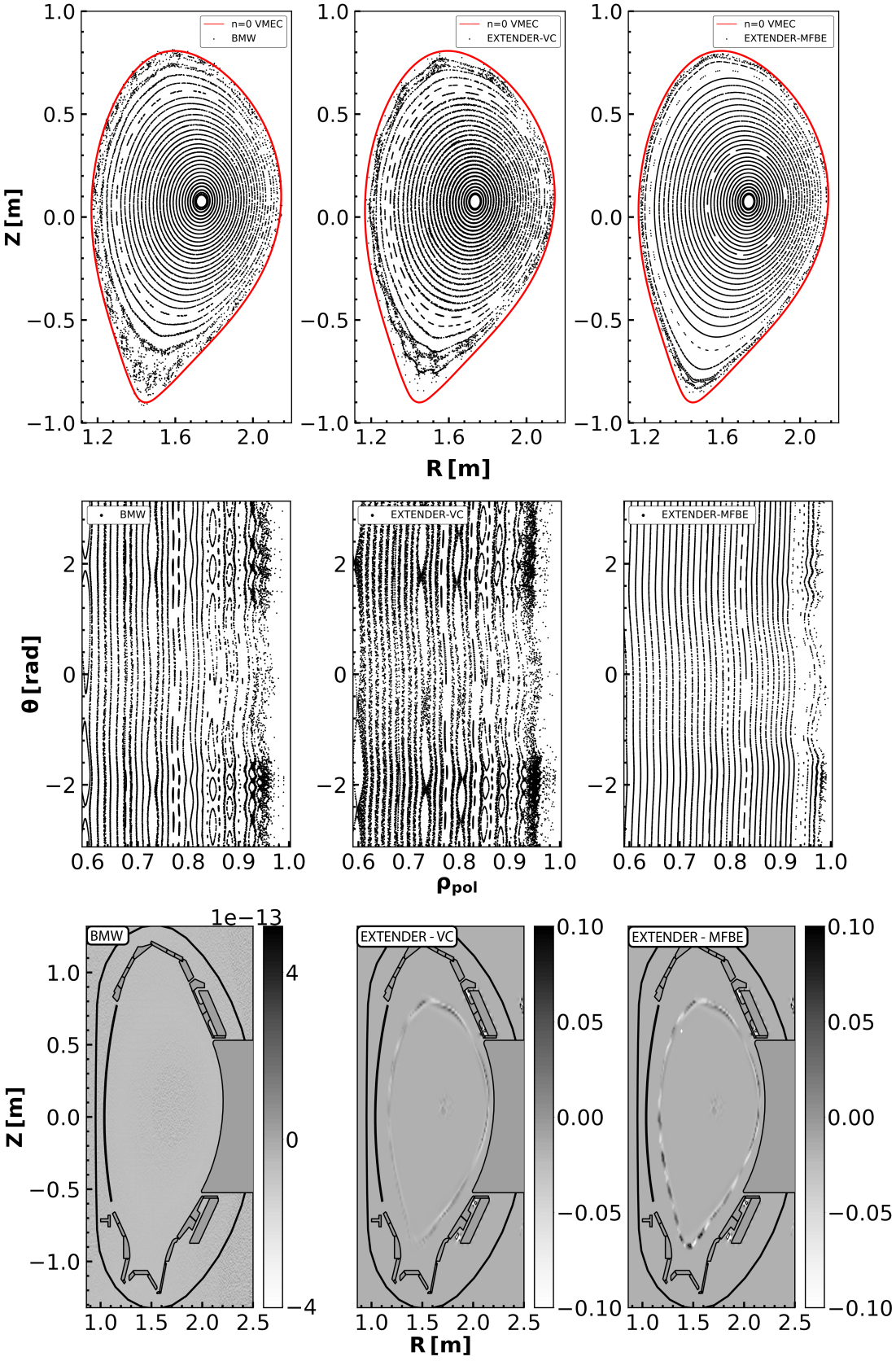

Figure 2.4: First row: Poincaré cross section plot for $\phi = 0$. Second row: same Poincaré plot as the first row but mapped to the $\{\theta, \rho_{\text{pol}}\}$ plane and zoomed into the $\rho_{\text{pol}} \in [0.6, 1.0]$ interval. Third row: Normalized divergence $\widetilde{\nabla B}$ of the induction field.

down to a tolerance of the force residuals $f_{\text{tol}} = 10^{-16}$. The result of this comparison can be seen in **figure 2.4**. In the upper row, a Poincaré plot cross-section is displayed as computed by the GOURDON code [42]. In the second row, the same Poincaré plot is displayed, but mapped to the $\{\rho_{\text{pol}}, \theta\}$ plane and zoomed into the $\rho_{\text{pol}} \in [0.6, 1.0]$ interval. For simplicity, the same poloidal flux matrix computed from BMW was used for the mapping of the other two cases. We observe that the BMW and EXTENDER-VC solutions display several islands localized near rational flux surfaces with the same $n = 2$ toroidal symmetry as the imposed perturbation field. On the other hand, the "MFBE" one, preserves completely the inner nested flux surfaces except at the very edge, where the precision of the aforementioned surface integral (**equation 2.37a**) is impoverished. In the last row, the divergence of the induction field is computed in cylindrical (toroidal) coordinates by implementing a first-order central finite differences nabla operator. The divergence scalar field is then normalized to a dimensionless quantity $\widetilde{\nabla B} = (R_0/B_0)\vec{\nabla}\vec{B}$ where $R_0 = 1.65\,\text{m}$ is ASDEX Upgrade's major radius and $B_0 = 2.5\,\text{T}$ is the central induction field value for this scenario. We verify that the BMW solution is divergence-free up to numerical accuracy, i.e., $\widetilde{\nabla B} \sim 10^{-13}$. The EXTENDER-VC approach displays larger divergence $\widetilde{\nabla B} \sim 0.1$. This is consistent with the numerical accuracy challenge of **equation 2.37a** when applied to two different domains that need to connect smoothly. We also observe that the effective flux surface "thickness", that is, the deviation of a field line from a perfect toroidal surface is substantially larger. Lastly, the "MFBE" computation fully preserves the PARVMEC nested flux surfaces, but also displays the largest divergence $\widetilde{\nabla B} \sim 0.15$. The same color bar scale was used in the EXTENDER-VC and "MBFE" divergence plots for clearer comparability. Given that $\widetilde{\nabla B} \sim 0$ for BMW and that the induction field calculation is more precise than in the EXTENDER-VC case, its usage becomes the optimal choice. These large differences between the three approaches are, however, expected to vanish for equilibria with no main rational flux surfaces, as it is often the case in stellarators.

A different approach that has been extensively used in the literature, the so-called "vacuum approximation" [47], consists in the linear superposition of an axisymmetric equilibrium calculation with the MP field. In this approach, no plasma response or screening of the MP field is possible, and therefore islands also arise in the *calculated* field. This approximation has been shown to fail to represent the measured plasma displacements in experiments [48] and to predict the loss of ELM suppression when the MP coil currents are ramped down [49]. Since the BMW solution displays islands in a similar fashion to the vacuum approximation, it is instructive to compare the field line tracing of the induction fields produced by both approaches. In order to obtain the vacuum approximation for our case, we first compute an axisymmetric PARVMEC solution using the same numerical parameters and force tolerance as the 3D case displayed in **figure 2.4**. BMW is then used to produce an induction field which extends up to the SOL. The vacuum field calculation of the MP coils is summed to the BMW one, which only accounts for the plasma currents in axisymmetry, and field lines are followed with the GOURDON code. A comparison of three fields: axisymmetric BMW field, the vacuum approximation and the 3D BMW field can be seen in **figure 2.5**. The vacuum approximation displays islands with larger width than in the BMW 3D case, which results in a more stochastic edge region. The lack of any MP shielding thus becomes manifest. This demonstrates that the BMW-3D approach includes the asymptotically approximated shielding currents that develop in PARVMEC given the used resolution in the radial grid, Fourier spectrum and force tolerance. This test also allows us to verify that no islands are present in axisymmetry, confirming the good accuracy of the GOURDON code.

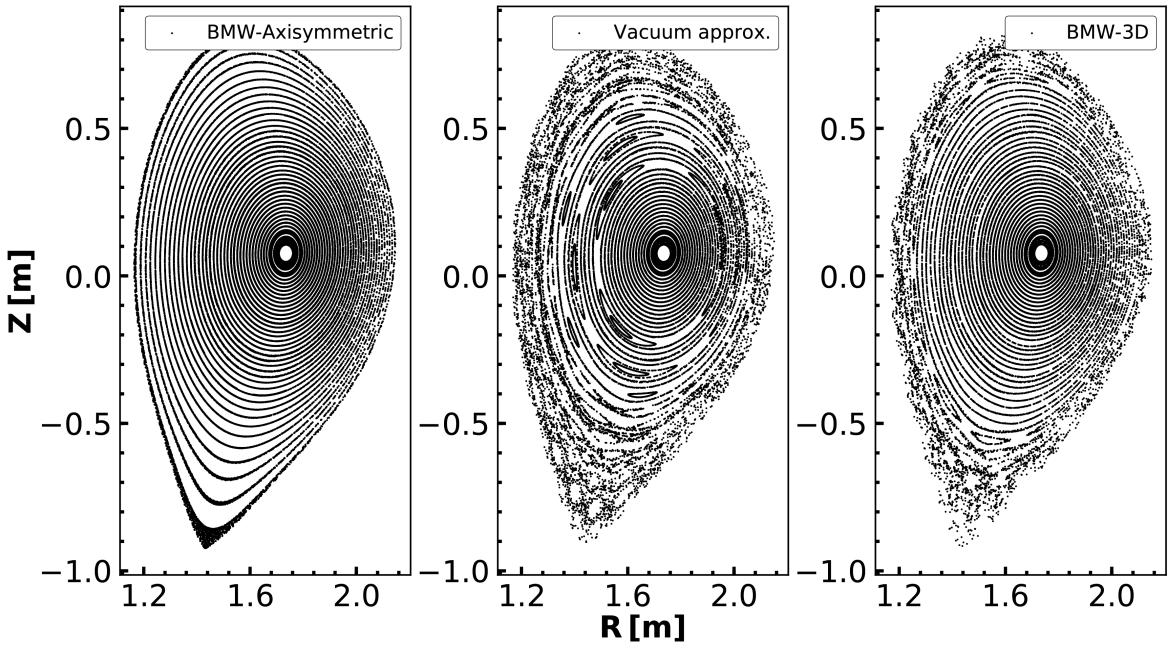

Figure 2.5: Poincaré plots of (left) axisymmetric BMW solution, (center) vacuum approximation and (right) BMW 3D solution.

A final approach that it is also worth mentioning, is that of the superposition of the vacuum approximation with an ad hoc constructed field [50]. The additional field is meant to provide complete MP shielding inside the core region, while the edge remains stochastic. Such a method has been used to study heat diffusion across the edge stochastic layer in ASDEX Upgrade [51]. This method, while useful as an user-tunable model, lacks a self-consistent description of the MHD equilibrium, plasma currents and flux surface displacements, parameters that have to be manually adjusted to the desired result. For this reason, this method lacks predictive applicability, which is regarded as one of the main objectives of this thesis.

2.2.6 Finite elements model for magnetic perturbation coils

Magnetic perturbation coils have been installed in many tokamaks with the main aim of mitigating and/or suppressing ELMs [52, 53]. The ASDEX Upgrade tokamak is equipped with two toroidally distributed arrays of eight in-vessel perturbation coils, situated at two different poloidal positions on the low field side. The coils are mounted on top of the passive stabilization loop (PSL), a copper bulk conductor meant to decrease the growth rate of the vertical instability [54]. When the coils operate in AC, eddy currents are induced both in the PSL and the Inconel casing of the coils. The net magnetic induction field is thus attenuated and lagged with respect to the one generated by the coils when simply considering the applied current to them, as 2D finite element (FE) simulations have demonstrated [55]. Due to different mounting distances of the upper and lower arrays to the upper and lower sections of the PSL, the lag and attenuation is different for each of them. Furthermore, the coil-plasma distance is often different as well for both arrays. This can be seen in **figure 2.6**, where a FE analysis[8] is performed for coil-plasma distances of $d_{\text{upper-plasma}} = 0.156\,\text{m}$ and $d_{\text{lower-plasma}} = 0.204\,\text{m}$, corresponding to the coil-plasma separation of discharge #32092.

[8] Kindly provided by W. Suttrop, IPP Garching

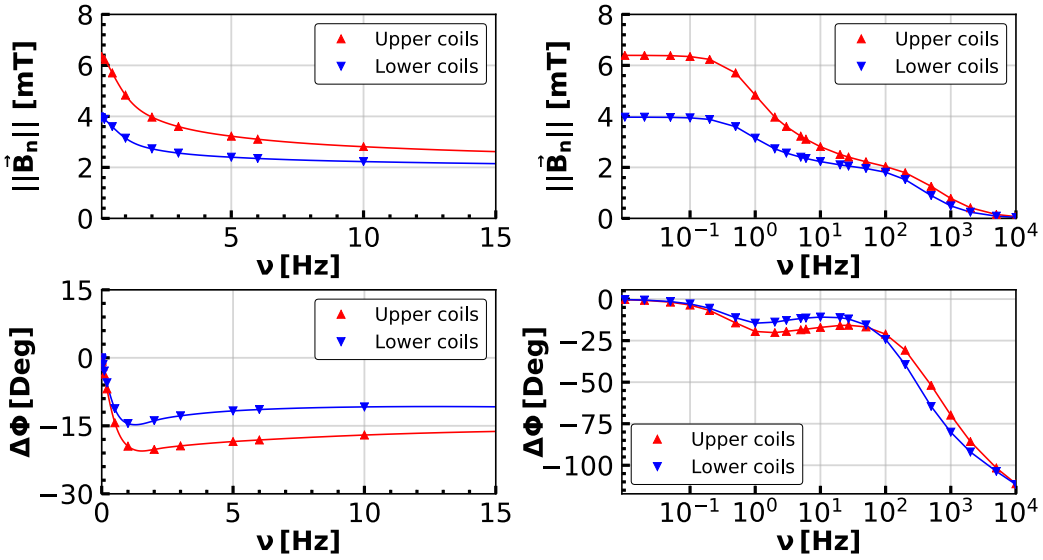

Figure 2.6: Module of the magnetic induction $||\vec{B}_n||$ produced by the magnetic perturbation coils and phase lag $\Delta\phi$ with respect to the applied current as a function of frequency. Observation points are taken perpendicular to the coil plane center at distances $d_{\text{upper-plasma}} = 0.156\,\text{m}$ and $d_{\text{lower-plasma}} = 0.204\,\text{m}$. Solid lines are cubic splines fitting the values.

This fact is taken into account for the MHD simulations by correcting the input current values of the MP coils. Given a coil current as a function of time, the current is not a perfect sinusoid, but contains numerous harmonics, such that its Fourier series can be written:

$$I_{\text{coil}}(t) = \sum_{n=1}^{N} a_n \sin\left(2\pi n \nu_0 t + \phi_n\right) \tag{2.39}$$

Where a_n is the amplitude of the n-th harmonic with frequency $n\nu_0$ and phase ϕ_n. Each harmonic is lagged and attenuated differently according to the FE analysis. We can then define an attenuation factor $\alpha(\nu)$, such that:

$$\alpha(\nu) = \left|\frac{B_n(\nu = 0)}{B_n(\nu)}\right| \tag{2.40}$$

Furthermore, the lag of the net field also depends on the frequency, such that $\Delta\phi = f(\nu)$. Our corrected current then becomes:

$$I'_{\text{coil}}(t) = \sum_{n=1}^{N} \frac{a_n}{|\alpha_n|} \sin\left(2\pi n \nu_0 t + \phi_n + \Delta\phi_n\right) \tag{2.41}$$

These corrections are implemented through Fourier analysis of the original current signals:

$$I(\nu) = \mathscr{F}(I(t)) = \text{Re}\left(I(\nu)\right) + i\text{Im}\left(I(\nu)\right) \tag{2.42}$$

$$||I(\nu)|| = \sqrt{\text{Re}(I(\nu))^2 + \text{Im}(I(\nu))^2} \tag{2.43}$$

$$\phi(I(\nu)) = \text{arctg}\left(\frac{\text{Im}(I(\nu))}{\text{Re}(I(\nu))}\right) \tag{2.44}$$

The real and imaginary parts of the current Fourier transform can be corrected, such that:

$$\mathrm{Re}(I'(\nu)) = \frac{\|I(\nu)\|}{\alpha(\nu)} \cos\left(\phi(I(\nu)) + \Delta\phi(\nu)\right) \tag{2.45}$$

$$\mathrm{Im}(I'(\nu)) = \frac{\|I(\nu)\|}{\alpha(\nu)} \sin\left(\phi(I(\nu)) + \Delta\phi(\nu)\right) \tag{2.46}$$

Then $I'(t) = \mathscr{F}^{-1}(I'(\nu))$. Since the FE analysis is performed for a limited frequency domain $\nu \in [0, \nu_{\max}^{\mathrm{FE}} = 10^4]$ Hz, any frequency component in the Fourier expansion of I_{coil} / $\nu_n > \nu_{\max}^{\mathrm{FE}}$ is discarded. This introduces a negligible error since $a_n \,\forall\, \nu_{\mathrm{n}} > \nu_{\max}^{\mathrm{FE}}$ are very small.

For a sinusoidal waveform applied to both coil rows, such as the one that we will apply in the experiments described in the next chapter, the total phase difference between both rows (upper vs. lower, i.e. "UL") can be defined as:

$$\Delta\varphi_{\mathrm{UL}} = \Delta\varphi_{\mathrm{UL}}^{0} + \Delta\varphi_{\mathrm{UL}}^{\mathrm{cond}} \tag{2.47}$$

Where $\Delta\varphi_{\mathrm{UL}}^{0}$ is the user-defined phase difference programmed in the coils' currents and $\Delta\varphi_{\mathrm{UL}}^{\mathrm{cond}}$ is due to the $\Delta\phi(\nu)$ effect by the PSL and Inconel conductors. Note that this effect is quite pronounced for individual coils as seen in **figure 2.6**. Nevertheless, since both upper and lower rows suffer similarly from it, the net total phase difference is not greatly changed for the low frequencies used in this study, i.e. $\nu = 3$ Hz (see **Chapter 3**). A further correction factor to **equation 2.47** arises from the fact that the upper coils don't have the same toroidal extension as the lower coils. This results in a relative shift of the geometrical center of the coils, which adds a further $\Delta\varphi_{\mathrm{UL}}^{\mathrm{geo}} \approx 2°$:

$$\Delta\varphi_{\mathrm{UL}} = \Delta\varphi_{\mathrm{UL}}^{0} + \Delta\varphi_{\mathrm{UL}}^{\mathrm{cond}} + \Delta\varphi_{\mathrm{UL}}^{\mathrm{geo}} \tag{2.48}$$

This is the final expression used in this study.

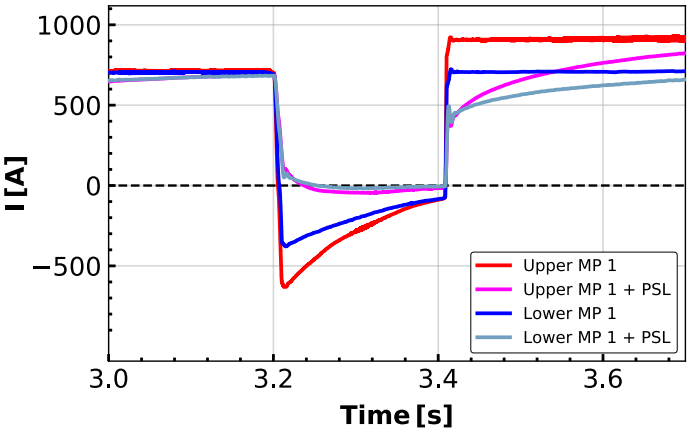

Figure 2.7: Applied currents to one pair of upper/lower MP coils and PSL-induced effective currents.

An example of the importance of this FE model can be found in [56], where the MP coils' current waveforms were designed such that a fast switch-off of the perturbation field occurs. This is done by balancing the PSL induced field with counter currents in the MP coils, as can be seen in **figure 2.7**. Note that the negative currents on the MPs drive an almost-zero net effective current of the MP-PSL system from t ≈ 3.2 – 3.4 s.

2.2.7 The EMC3-EIRENE code

The edge Monte Carlo EMC3-EIRENE code computes the 3D transport equations of different plasma species in fluid approximation, EMC3 [57, 58], and is coupled to a kinetic description of neutral species, EIRENE [59], through the sources and sinks. The mass, momentum and energy equations in conservation form read:

$$\vec{\nabla} \cdot \left[n_i v_{i\parallel} \hat{b} - D_i \hat{b}_\perp \hat{b}_\perp \cdot \vec{\nabla} n_i \right] = S^p \tag{2.49}$$

$$\vec{\nabla} \cdot \left[p_{i\parallel} v_{i\parallel} \hat{b} - \eta_\parallel \hat{b}\hat{b} \vec{\nabla} v_{i\parallel} - D_i \hat{b}_\perp \hat{b}_\perp \cdot \vec{\nabla} p_{i\parallel} \right] = -\hat{b} \cdot \vec{\nabla} p + S^m \tag{2.50}$$

$$\begin{aligned} \vec{\nabla} \cdot \Bigg[& \frac{5}{2} n_{e/i} T_{e/i} v_{i\parallel} \hat{b} - \kappa_{e/i} \hat{b}\hat{b} \cdot \vec{\nabla} T_{e/i} - \frac{5}{2} T_{e/i} D_i \hat{b}_\perp \hat{b}_\perp \cdot \vec{\nabla} n_{e/i} \\ & - \chi_{e/i} n_{e/i} \hat{b}_\perp \hat{b}_\perp \cdot \vec{\nabla} T_{e/i} \Bigg] = \mp K_B (T_e - T_i) + S^e_{e/i} \end{aligned} \tag{2.51}$$

with $\eta_\parallel$ the parallel viscous momentum transport coefficient, $n_{e/i}$, $T_{e/i}$, $\kappa_{e/i}$, $\chi_{e/i}$, the density, temperature, parallel-field and cross-field energy transport coefficients for electrons and ions, $p_{i\parallel} = n_i m_i v_{i\parallel}$, S^p, S^m, $S^e_{e/i}$, the particle, momentum and energy sources associated with neutrals, and S^e_e also containing energy loss from impurity radiation. D is the diffusion tensor, that is separated in parallel $D_\parallel$ and perpendicular $D_\perp$ components. Impurities are also modeled through an analogous continuity equation that includes ionization and recombination, as well as a momentum balance equation that accounts for their interaction with bulk plasma ions and electrons.
These fluid equations are solved with a Monte Carlo scheme. The transport of Monte Carlo *particles*[9] is described by a stochastic process with a local transition probability function T. This can be integrated along magnetic field lines, in order to separate parallel from perpendicular transport, i.e.:

$$T = \underbrace{T_\parallel(l, \Delta t, v_\parallel, D_\parallel)}_{\parallel \text{ contribution}} \cdot \underbrace{\frac{1}{4} \sum_{ij} \delta_{ij} (\Delta r - \Delta r_{\perp ij}(v_\perp, D_\perp))}_{\perp \text{ contribution}} \tag{2.52}$$

The EIRENE code, to which EMC3 is coupled, computes the Boltzmann equation for each neutral species using a linear collision operator. This linear system of kinetic equations can be reduced to a single kinetic equation by considering the species index, i, as an additional coordinate in phase space. Integrating such equations yields:

$$f(x) = S(x) + \int_{x'} f(x') \cdot K(x' \to x) \, \mathrm{d}x' \tag{2.53}$$

$$K(x' \to x) = C(r', v', i' \to v, i) \times T(v, i, r' \to r) \tag{2.54}$$

which designates a Markovian process, with x, x' the general coordinates for two states $\{\vec{r}, \vec{v}, i, t\}$, and $K(x' \to x)$ the transition kernel. This kernel is decomposed in a collision kernel, C, (changing velocity and species state at r') and a transport kernel, T, changing the position of the test particle between collision events. Within the collision kernel, one can consider each of the possible collision processes weighted by a given cross-section, such as CX, elastic collisions, dissociation, etc. $S(x)$ represents the particle sources distribution function such as gas puff, recycling, etc. The coupling of EIRENE to EMC3 is performed by taking a given moment of the neutral distribution function with a weighting function g_t:

[9] In the sense of mean-field particles, i.e. samples of a deterministic distribution function.

$$S^t = \int f(x) g_t(x)\,\mathrm{d}x \tag{2.55}$$

where g_t is a function that would depend on the source term in question, i.e. particle, momentum or energy.

The detailed transport equations in EMC3-EIRENE allow for a realistic reconstruction of the SOL density profile within the fast wave coupling region, and this will be shown in **section 4.3**. Combining this scheme with PARVMEC&BMW, which provide a background MHD equilibrium calculation in 3D, one can go beyond the limitations of using only MHD codes[10]. On the other hand, this scheme is not self-consistent, i.e., transport does not affect the magnetic field calculation, and the SOL magnetic description of PARVMEC&BMW arises from a superposition principle that does not consider SOL inherent currents.

2.2.8 The RAPLICASOL code

The RAPLICASOL code [61–63] performs full-wave simulations on a finite element mesh, and is able to handle the realistic geometry of ICRF antennas. Maxwell equations are solved in vacuum or plasma conditions, imposed via a dielectric tensor. In its current version, the cold plasma dielectric tensor introduced in **equation 1.20** is used for the plasma region. A set of "perfectly matched layers" (PMLs) [64] provides absorbing boundaries at the radial, toroidal and poloidal ends of the simulation domain (see **figure 2.8**), that serve to mimic the outward radiation boundary condition, i.e. no wave reflection.

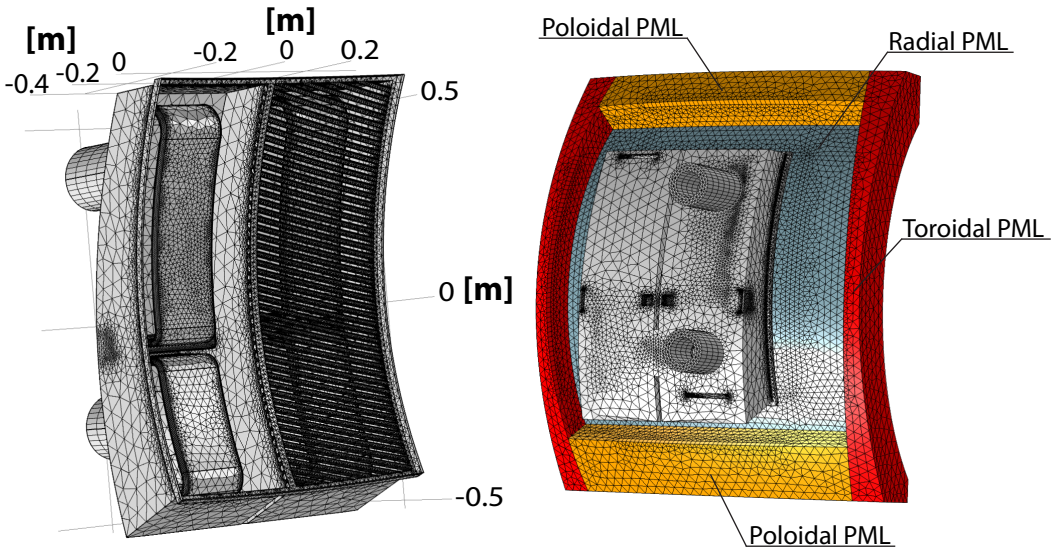

Figure 2.8: Left: RAPLICASOL 2-strap ICRF curved antenna model with mesh. Right: Meshed ICRF antenna and PMLs. Red: toroidal PML. Orange: Poloidal PML. Blue: Radial PML. The same color has been used for vacuum and plasma PMLs.

[10]Even if multi-fluid time-domain MHD equations are solved, i.e. in the JOREK code, these currently offer a substantial less realistic description of the far SOL, where Dirichlet boundary conditions are often used (e.g. $n_e(\rho_{\mathrm{pol}} > x) = \text{const.}$) [60].

The code is run through the COMSOL Multiphysics® software package, which provides the necessary tools to create finite element meshes. Everything else, the antenna model, the simulation domain and the physics, has been integrated externally into COMSOL. The wave equation in *double-curl* notation and frequency domain is solved:

$$\vec{\nabla} \times \left(\overline{\overline{\mu^{-1}}}\, \vec{\nabla} \times \vec{E} \right) - \omega^2 \overline{\overline{\epsilon}} \vec{E} = -i\omega \vec{j}_{\text{free}} \tag{2.56}$$

The solution vector $\vec{E}$ is chosen in a subspace of $H_0(\text{curl}, \Omega)$ spanned by edge Nédélec elements, with $H_0(\text{curl}, \Omega) = \{\vec{F} \in \mathcal{L}^2,\ \vec{\nabla} \times \vec{F} \in \mathcal{L}^2,\ \hat{n} \times \vec{F} = 0\}$ being a Sobolev space where we assume the metallic surfaces to be perfect electrical conductors. The problem is solved in weak formulation, by asking all vectors $\vec{v} \in H_0(\text{curl}, \Omega)$ to fulfill:

$$\left\langle \overline{\overline{\mu^{-1}}}\, \vec{\nabla} \times \vec{E}, \vec{\nabla} \times \vec{v} \right\rangle - \omega^2 \left\langle \overline{\overline{\epsilon}} \vec{E}, \vec{v} \right\rangle = -i\omega \left\langle \vec{j}_{\text{free}}, \vec{v} \right\rangle \tag{2.57}$$

With $\mathcal{L}^2$ the Lebesgue-2 inner product.

As an output, RAPLICASOL computes the $\vec{E}, \vec{H}$ field distributions in the simulation domain and the S-matrix of the ICRF antenna at a plane intersecting the transmission lines. This S-matrix can be converted to quantities of experimental interest, such as the voltage standing wave ratio and the loading resistance (see **equation 1.42**, **equation 3.11** and **equations 3.12**).

Chapter 3

Experimental study of ICRF coupling in 3D geometry

This chapter includes adapted material from:
G. Suárez López et al. *"Investigation of the coupling properties of the ion cyclotron fast wave under applied magnetic perturbations and MHD phenomena in ASDEX Upgrade"*, published in *EPJ Web of Conferences* **157** (2017) [65].
G. Suárez López et al. *"ICRF Coupling in ASDEX Upgrade magnetically perturbed 3D plasmas"*, published in *Plasma Phys. Control. Fusion* **61** 125019 (2019) [66].

In this chapter, the influence of non-axisymmetric tokamak plasma configurations on ICRF coupling performance is experimentally studied. First, the case of MHD instabilities is briefly introduced. The rotation of a (2,1) tearing mode coherently modifies the loading resistance measured in all antenna feeders. Due to the large mode rotation frequency $\sim$ kHz, edge density measurements pose a challenge, these being key for their correlation to the RF measurements. Therefore, a more consistent approach based on the usage of magnetic perturbation (MP) fields was sought.
The RF properties of the four ICRF antennas in the ASDEX Upgrade tokamak are characterized in high-confinement (H-mode [67]) magnetically perturbed 3D discharges. An $n = 2$ MP field is applied and rigidly rotated, which allows diagnosing the separatrix displacement and consequent coupling change. We find the antenna loading resistance to be coherently modified by the resulting non-axisymmetric plasma equilibria, thus becoming a function of the applied MP field poloidal mode spectra. We perform a detailed statistical analysis, which correlates the change in loading resistance to the fast wave R-cutoff layer movements. From it, a 1D scaling is derived that differs from previous studies evaluated in pure axisymmetric plasma conditions. This experimentally derived scaling is used to predict the average loading resistance change of the ITER ICRF antenna under applied MPs. ICRF coupling simulations using measured 1D density profiles are performed with the RAPLICASOL code, in order to investigate the predictive capabilities of numerical state of the art tools. We find that both 1D conventional scaling laws and 1D numerical simulations fail to capture the 3D physics, and can substantially overestimate the measured loading resistance change up to a factor of ~ 3.

3.1 Effect of MHD modes on ICRF Coupling: A case study

The effect of 3D tokamak configurations on ICRF coupling can be demonstrated in MHD active ICRF heated discharges. MHD instabilities can deform the plasma boundary in a non-axisymmetric fashion. This occurs in the presence of "external kink modes" or "internal modes" (ideal or resistive) with toroidal coupling to external ones. The displacement produced depends upon their radial profile, $\hat{\xi}(r)$, and growth rate, γ, which in the limit of linearized MHD can be described as [68]:

$$\vec{\xi}(r,\theta,\phi,t) = \hat{\xi}(r)\exp\left[i(m\theta - n\phi + \omega t) + \gamma t\right] \tag{3.1}$$

with m, n the poloidal and toroidal mode numbers, here assumed unique, and ω the mode rotation frequency. In this section, we present the case of coherent modulation of the loading resistance in the ICRF antennas with the rotation of a (2,1) tearing mode [65].

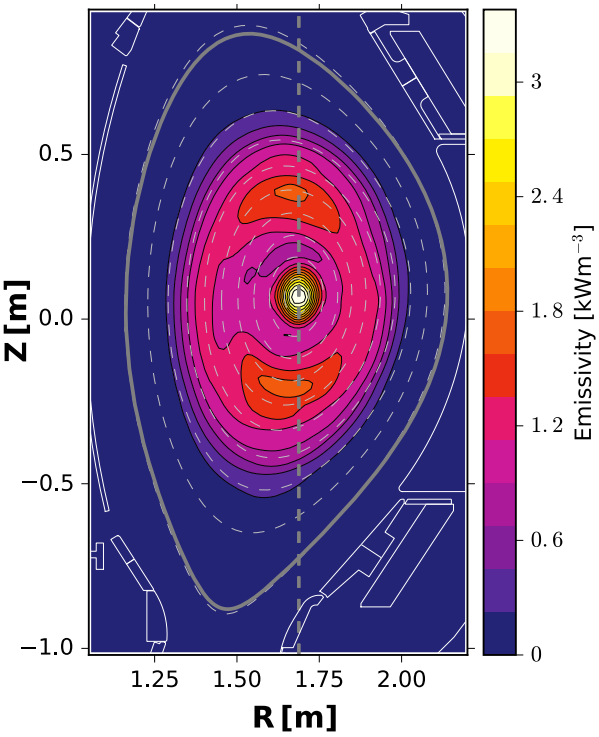

Figure 3.1: Soft X-Ray emission profile for discharge #32749 at $t \sim 3.25$ s. Two island O-Points are clearly distinguishable.

Soft X-Ray measurements, presented in **figure 3.1**, locate the main island at $\rho_\theta \sim 0.5 \pm 0.1$. The (2,1) mode numbers are identified via the poloidal and toroidal arrays of Mirnov and Ballooning coils present on the tokamak vessel. A spectrogram in **figure 3.2** shows the same frequency components for the loading resistance measured in the upper feeder of ICRH1, and a Ballooning coil in the vessel wall, which registers the change of radial magnetic field, $\dot{H}_r$, due to the mode rotation. The change in loading resistance is hypothesized to be connected with a density modification in front of the ICRF antennas due to the three-dimensional displacement produced by the MHD mode. The loading resistance spectrogram also displays a beat wave pattern from $3s$ on. The reason is the activation of the 3-strap antennas, which are shifted by 1 kHz in their operational frequency with respect to the 2-strap antennas. During the time period highlighted, a loading resistance oscillation an order of magnitude faster than the ELM cycle and with significant amplitude is observed during the appearance of this (2,1) mode, as seen in **figure 3.2(b)**. Due to the fast rotation frequency $\nu \sim 3$ kHz of this MHD mode, and most in general, edge density measurements with standard diagnostics, i.e. lithium beam, are challenging[1]. Since these are of crucial importance for their correlation to RF measurements, a different approach to the study of 3D configurations was taken. The magnetic perturbation system in ASDEX Upgrade can be utilized to create 3D plasma corrugations via the excitation of edge kink modes. A controlled rigid rotation of the

[1]Faster edge density measurements are now possible with O-mode and X-mode reflectometry. However, X-mode reflectometry was not yet available at the start of this Ph.D. thesis [27], and O-mode reflectometry does not cover the whole fast wave coupling region alone.

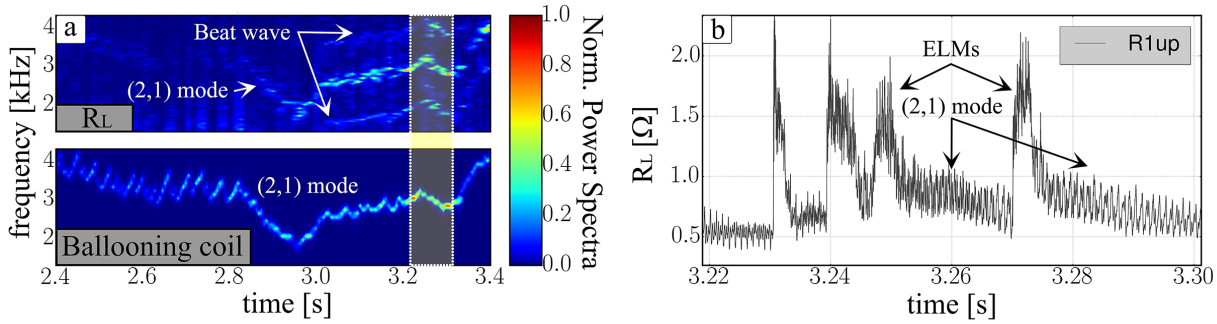

Figure 3.2: Discharge #32749. (a) Spectrograms of the loading resistance measured in the upper feeder of ICRH1 and Ballooning coil for reference. The signature of an MHD mode is clearly visible on both signals. (b) Loading resistance during the highlighted time region.

perturbation field is also possible with a more optimum time scale for the density measurements of ~ Hz. This approach also presents interest beyond pure academic research, since MP coils are foreseen in ITER for ELM control, thus allowing the determination of their impact on the ICRF system. In what follows, we will explore this approach, and confirm with the results obtained both its academic interest and practical utility.

3.2 ICRF coupling experiments with Magnetic Perturbations

ICRF coupling can be influenced by MPs in two ways. On the one hand, the known pump-out effect tends to improve ICRF coupling [69], as it produces an increase in the radial particle transport from the confined region to the SOL. On the other hand, the plasma response to the MPs results in a field-aligned kink displacement that modifies the plasma density in a non-axisymmetric fashion.

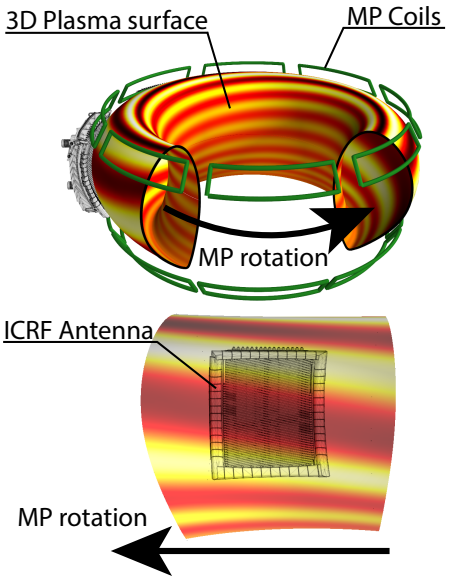

Figure 3.3: Arbitrary $n = 2$ deformed LCFS computed by the PARVMEC code and ICRF antenna. The 3D plasma deformation is shown in color.

This kink response has been well predicted and characterized in many tokamaks, such as ASDEX Upgrade [48, 70], DIII-D [71] and MAST [72]. The density perturbation extends into the ICRF fast wave coupling region in the SOL, modifying the R-cutoff in just the same fashion. The degree of displacement and its topology depend upon the toroidal and poloidal mode number spectrum of the MP field, the edge plasma current and the edge pressure gradient. We have systematically studied for the first time the coupling properties of the fast wave when MP fields are applied and rigidly rotated. This allows us to assess the impact of plasma non-axisymmetric profiles, regardless of where the ICRF antennas are placed inside the vessel. For this purpose, we have utilized the MP and ICRF systems in the ASDEX Upgrade tokamak (see **fig-**

ure 3.3). In addition, the poloidal phasing of the MP coils is scanned, and the effect of the plasma response to the MPs on the ICRF system is discussed. It is shown that for the studied plasma conditions, $\Delta\varphi_{\mathrm{UL}}$ plays a significant role on the response of the ICRF system. In the remainder of this chapter, plasma discharges with ICRF heating and MPs are described along with measurements of key RF quantities. The effect of different MP phasings on ICRF coupling is studied. We compare the experimental results against 1D analytical formulas and experimentally-derived scalings found in the literature, in order to assess their validity under our experimental conditions. A statistical analysis of the data allows deriving a 1D scaling for the average loading resistance change under applied MPs. Numerical simulations using measured 1D density profiles are presented and compared to the experiments. Finally, the experimentally-derived 1D scaling is utilized to predict the average loading resistance changes in the ITER ICRF antenna due to MP plasma displacements.

3.2.1 Discharges description

A set of five H-mode discharges was performed in order to study the effect of MPs on ICRF coupling. In order to explore a reactor-relevant scenario, two main parameters were optimized: high plasma $\beta_{\mathrm{N}} \sim 2$ and low electron and ion pedestal collisionalities $\nu_e^* \sim 0.25 - 0.65$, $\nu_i^* \sim 0.15 - 0.25$. Time traces for the edge safety factor q_{95}, plasma current I_{p}, core line-averaged electron density $\langle n_e \rangle$, deuterium gas puff $D_{\mathrm{puff}}^{\mathrm{tot}}$ and applied total power P_{tot} can be seen in **figure 3.4**. The discharges were performed in Lower Single Null (LSN) configuration, with the ion $\vec{\nabla}B$ drift pointing towards the X-point. The plasma parameters were kept constant with on-axis $|B_t| = 2.5\,\mathrm{T}$, $I_{\mathrm{p}} = 0.8\,\mathrm{MA}$, resulting in an edge safety factor $q_{95} \sim 5.3$, with core line-averaged electron density $\langle n_e \rangle \sim 5 \times 10^{19}\,\mathrm{m}^{-3}$. A total heating power of $P_{\mathrm{tot}} \sim 11.5\,\mathrm{MW}$ was applied, out of which $P_{\mathrm{ICRF}} \sim 2.2\,\mathrm{MW}$ was delivered simultaneously by the four ICRF antennas in dipole phasing. This value is the generator power after subtracting the dissipated power in the 3dB hybrid coupler loads and the Ohmic losses in the transmission lines, accounted for by vacuum measurements on the 2-strap antennas. The ICRF heating scenario was minority (H)-D, second harmonic D ($\omega_{\mathrm{ICRF}} = 2\omega_{c,D}$), with central deposition at a frequency $\nu_{\mathrm{ICRF}} = 36.5\,\mathrm{MHz}$. The rest of the heating power was supplied by NBI ($\sim 6.8\,\mathrm{MW}$) and ECRH ($\sim 2.5\,\mathrm{MW}$). The discharges were fueled with deuterium gas by a single lower divertor valve located in sector 13 (**figure 1.4(a)**). One of the discharges was performed as a reference (#34632), without magnetic perturbations. For the rest of discharges, the MPs were switched on at 2 seconds, during the flat top, and were supplied with $I_{\mathrm{coil}} = 5\,\mathrm{kA} \times \mathrm{turns}$. Two differential phasings, $\Delta\varphi_{\mathrm{UL}}$, were applied per discharge in $n = 2$ toroidally symmetric configuration and rigidly rotated with a frequency of $\nu_0 = 3\,\mathrm{Hz}$ for diagnostic purposes. The last two discharges terminated prematurely due to disruptions, and only one $\Delta\varphi_{\mathrm{UL}}$ phase was acquired for them, resulting in a set with $\Delta\varphi_{\mathrm{UL}} = \{-145°, -45°, 0°, +45°, +90°, 180°\}$. For the discharge with $\Delta\varphi_{\mathrm{UL}} = \{-45°, +45°\}$ a sputtered tungsten flake produced a density increase from 1.5-3 s, hence this time slice is rejected in the analysis. The resulting average plasma beta poloidal, $\langle \beta_{\mathrm{pol}} \rangle_t$, electron and ion collisionalities, $\langle \nu_e^* \rangle_t$, $\langle \nu_i^* \rangle_t$, are presented in **table 3.1** for reference. The collisionalities were computed according to the formulas included in [73, 74] using the electron density and temperature profiles obtained from the integrated data analysis (IDA) [30] and the ion temperature profiles obtained from charge exchange recombination spectroscopy (CXRS)[2]. All the profiles are evaluated at $\rho_{\mathrm{pol}} = 0.9$, i.e. at the pedestal top.

[2]Here, we consider $T_{D^+} \sim T_{B^{5+}}$.

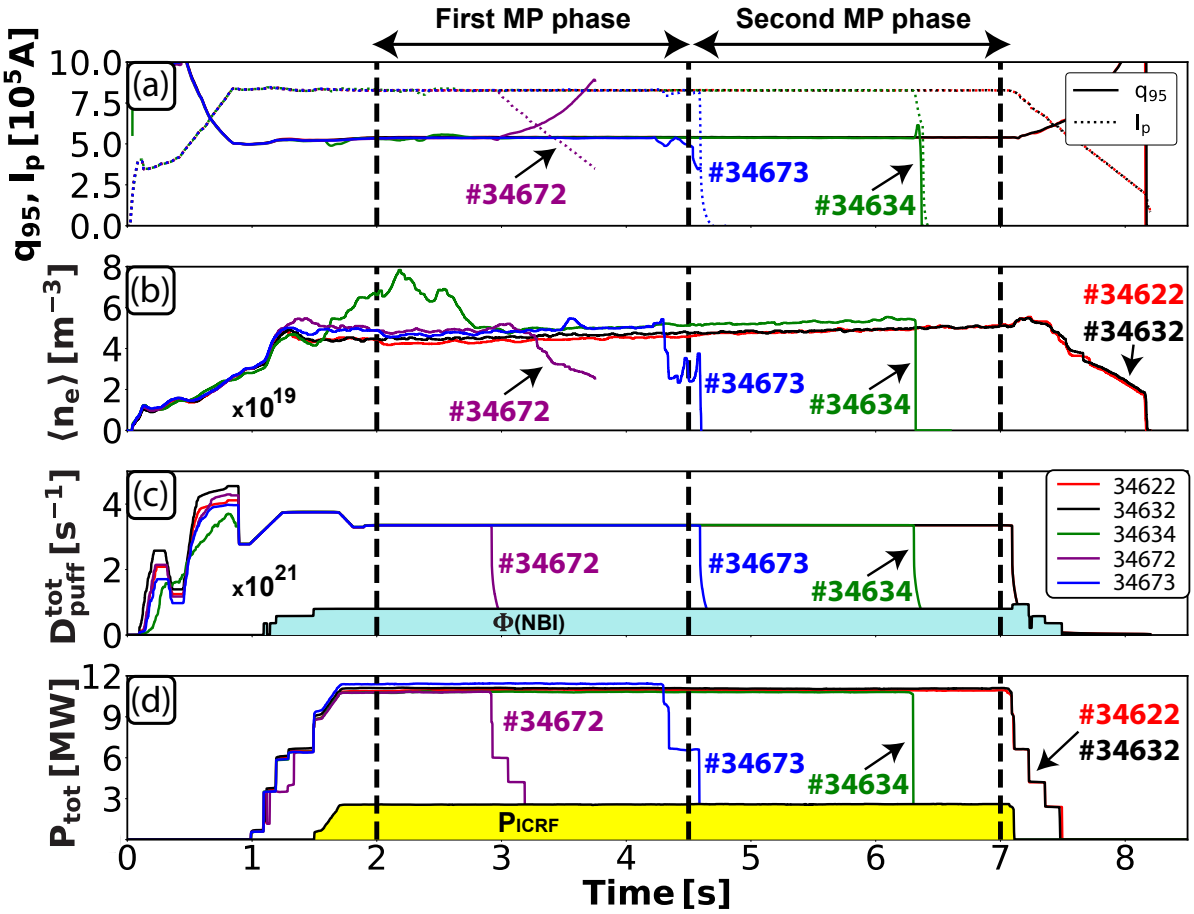

Figure 3.4: Time traces of the considered discharges: (a) Safety factor at 95% poloidal flux, q_{95}, and plasma current, I_p (b) core line-averaged electron density $\langle n_e \rangle$, (c) total deuterium fueling $D^\mathrm{tot}_\mathrm{puff}$ with NBI contributed particle flux and (d) total power P_tot out of which, ICRF power fraction, P_ICRF.

Shot #	$\Delta\varphi_\mathrm{UL}$	used MP periods	$\langle\beta_\mathrm{pol}\rangle_t$	$\langle Z_\mathrm{eff}\rangle_t$	$\langle\nu^*_\mathrm{e}(\rho_\mathrm{pol}=0.9)\rangle_\mathrm{t}$	$\langle\nu^*_\mathrm{i}(\rho_\mathrm{pol}=0.9)\rangle_\mathrm{t}$
34622	0°, 180°	8, 8	1.38, 1.37	1.42, 1.41	0.44, 0.64	0.18, 0.24
34632	No MPs	-	1.42	1.37	0.57	0.19
34634	−45°, 45°	5, 5	1.53, 1.47	1.57, 1.33	0.25, 0.25	0.16, 0.16
34672	90°	3	1.5	1.30	0.30	0.15
34673	−145°	4	1.52	1.28	0.29	0.15

Table 3.1: Discharge numbers with MP configuration and average parameters of interest: Number of used MP periods in the analysis, time-averaged poloidal plasma beta $\langle\beta_\mathrm{pol}\rangle_t$, time-averaged effective charge number $\langle Z_\mathrm{eff}\rangle_t$, time-averaged electron/ion collisionality at the pedestal top $\langle\nu^*_\mathrm{e}\rangle_\mathrm{t}$ / $\langle\nu^*_\mathrm{i}\rangle_\mathrm{t}(\rho_\mathrm{pol}=0.9)$.

The Z_eff value was obtained from Bremsstrahlung emission. For the ion density, a fractional boron impurity percentage of $n_\mathrm{B}/n_e \sim 0.005$ was consistently computed by the CHICA code [75]. In order to represent all the impurity species, this value was scaled to match the measured Z_eff, such that $(n_\mathrm{B}/n_e)_\mathrm{scaled} \sim 0.013 - 0.03$. Due to the passive stabilization loop (PSL) on which the MP coils are mounted inside the vessel, the applied perturbation field is attenuated and lagged with respect to the expected one when no conducting structures are taken into account. The combination of this attenuation and a pedestal pressure of $p_\mathrm{ped} \sim 16.5\,\mathrm{kPa}$ ($p_\mathrm{ped,e} \sim$

7.5 kPa), results in the ELM behavior to be unchanged by the MPs, that is, the discharges behaved as regular ELMy H-modes. This behavior is consistent with previous studies of ELM mitigation and suppression accessibility in ASDEX Upgrade [49].

Even though all discharges were performed with the same input waveforms on the actuators, some differences are noticeable. Discharges #34622 and #34632 have higher electron collisionalities than the others, which arise from lower pedestal electron temperatures. They were performed on the same experimental session and thus with very similar machine conditioning. On the other hand, the rest of discharges were distributed into two different experimental sessions, and the difference in plasma parameters is attributed to different machine conditioning and core MHD activity. Furthermore, since no feedback control was used on the density profile, its average value is seen to increase during the discharge time for all the performed experiments, due to NBI fueling and the feed-forward gas puff. While electron density changes have an impact both on the plasma response to the MPs and on the ICRF coupling, such changes are taken into account for all the studied quantities, as discussed in **section 3.2.4**, through baseline correction and sinusoidal fits representing the average value over the considered MP periods.

3.2.2 Plasma response to applied magnetic perturbations. Effect of MPs on the SOL density profiles

The plasma edge 3D displacement was evaluated with toroidally localized diagnostics in the same fashion as in [48, 70]. The MP field is rigidly rotated and the diagnostics register variations in the plasma kinetic profiles locked to the external field as a time-dependent oscillation of their measurement quantity. In this study, we have used the lithium beam diagnostic [24], two chords of the CXRS diagnostic (termed CMZ: edge toroidal CXRS and CPZ: edge poloidal CXRS) [23], three X-mode reflectometry channels embedded in the 3-strap antenna ICRH4 [27], labeled as Ref. X{1,4,8} in **figure 2.1**, and the midplane O-mode reflectometer [26]. These diagnostics are positioned on the low-field side (LFS) of ASDEX Upgrade, with the CXRS chords, Ref. X4 and Ref. O-mode at the outboard midplane (OMP), here $\theta \approx 0$, the lithium beam and Ref. X1 above the midplane and Ref. X8 below the midplane. The CXRS diagnostics track the B^{5+} impurity line intensity corresponding to $\lambda \approx 494$ nm, which is taken as a proxy for the B^{5+} impurity density, while in the lithium beam and reflectometers case we use the reconstructed electron density profiles.
The plasma displacements are evaluated in time-domain by tracing the position ($d^{\mathrm{iso}}_{\mathrm{LOS}}$) of constant intensity or density layers over the line of sight (LOS) of each diagnostic during the MP rotation. The data is ELM-filtered, and an ordinary least squares (OLS) fit is performed to the position of these iso-layers. The OLS fit computes the amplitudes of sine functions ($|\xi_n(\nu_j)|$) and the coefficients of a polynomial (α_k) for baseline subtraction. We chose to fit 4 harmonics of the fundamental frequency, ν_0, i.e., $\nu_j = (j+1)\nu_0 \ \forall j \in [0,3]$, and a cubic polynomial:

$$d^{\mathrm{iso}}_{\mathrm{LOS}} \approx \sum_{j=0}^{j=3} |\xi_n(\nu_j)| \sin(\omega_j t + \phi_j) + \sum_{k=0}^{k=3} \alpha_k t^k \tag{3.2}$$

where $\omega_j = 2\pi\nu_j$ and ϕ_j is the phase of each sine function. The resulting displacement profiles of the density layers for $|\xi_n(\nu_0)|$ can be seen in **figure 3.5** for the $\Delta\varphi_{\mathrm{UL}} = 0°$ and reference cases. During the MP phases, the plasma displacements decay monotonically in the SOL. This is well-registered by both the lithium beam and the reflectometers, with the exception of a "bump"

observed in the lithium beam at around $n_e \sim 7 - 8 \times 10^{18}\,\mathrm{m}^{-3}$, which matches the position of the H-mode density shoulder [76].

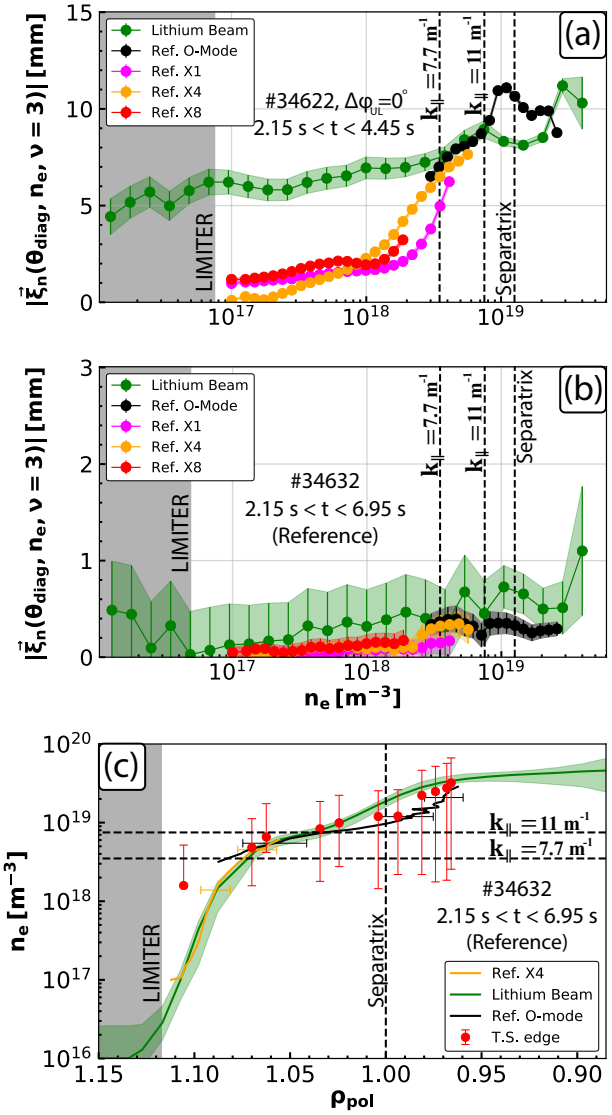

Figure 3.5: (a,b) n_e-dependence of the OLS $|\xi_n(\nu_0)|$ estimator amplitude for the $\Delta\varphi_{UL} = 0°$ and reference cases. The time-averaged n_e at the limiter was evaluated using the lithium beam LOS on a per-discharge basis (c) Time-averaged n_e profiles for the reference case from Ref. X4, Ref. O-mode, lithium beam and edge Thomson scattering diagnostics. Reflectometry error bars are taken as 1σ and only displayed for some points.

Very good agreement is found among all the diagnostics in the region $3 \times 10^{18}\,\mathrm{m}^{-3} < n_e < 8 \times 10^{18}\,\mathrm{m}^{-3}$, which includes the R-cutoff for all the ICRF antennas. However, in the far SOL no absolute agreement is found when MPs are active, despite the fact that the fluctuation level for $|\xi_n(\nu_0)|$ is very similar when no MPs are applied. The ICRF limiter position in density-space is included along the lithium beam LOS, to give a reference of the measurements alignment and discard its effect on the displacements. The time-averaged density profiles are also included for the reference case as a function of the $\rho_{\mathrm{pol}} = \sqrt{\chi - \chi_0/\chi_{\mathrm{sep}} - \chi_0}$ magnetic coordinate, with χ the poloidal flux at a given point, χ_{sep} the poloidal flux at the separatrix and χ_0 the poloidal flux at the magnetic axis. This comparison highlights the good agreement of the diagnostics in axisymmetry in the $n_e \sim 10^{18}\,\mathrm{m}^{-3}$ region. Measurements of the density profile in reflectometry depend on different parameters: X-mode reflectometry requires an accurate magnetic equilibrium reconstruction in order to correctly place the position of the first fringe, or first plasma *echo* [25]. The precision of the magnetic reconstruction is hampered when MPs are applied, since the used tool (the CLISTE code [77]), is a Grad-Shafranov solver that can only handle axisymmetric plasmas. Furthermore, there are built-in assumptions when computing the density profiles, such as a constant residual density for the wave upper cut-off determination, that can affect the density profile initialization [28]. Similarly, in O-mode reflectometry while the magnetic field plays no role, the assumption of a constant value for the $R(n_e = 0) = 2.24\,\mathrm{m}$ is used. On the other hand, the profiles should be less sensitive to these effects the farther they are from their initialization point, which can explain the good agreement with the lithium beam at the $n_e \sim 10^{18}\,\mathrm{m}^{-3}$ density layers. A detailed study of the differences between the diagnostics and possible improvements to X-mode reflectometry when a proper 3D magnetic reconstruction is used, goes however, beyond the scope of this thesis. It should also be kept in mind that the lithium beam profiles become more inaccurate inside the

pedestal region, $n_e \gtrsim 3-4\times10^{19}\,\mathrm{m}^{-3}$, where beam attenuation plays an important role [24]. In this study, we have included the data obtained from reflectometry under the premises that:

1. Reflectometry profiles are always used in relative terms, that is, to compare the change between the minimum and maximum plasma-antenna gap distance. In this manner, systematic errors play a smaller role.

2. The good agreement among all the diagnostics in the $n_e \sim 10^{18}\,\mathrm{m}^{-3}$ density layers further motivates their validity in this region. For the ICRF cutoff oscillation, either using the lithium beam or reflectometry density profiles does not change the conclusions of our study. The R-cutoff displacements are nearly equivalent for both diagnostics (we refer to **figure 3.5(a)**).

3. The ICRH4 embedded X-mode reflectometers offer a description of the poloidal distribution of the density profile. This information is very valuable to the study at hand, and unavailable otherwise.

From now on, we will focus exclusively on three positions of interest for this study: the separatrix and the two main R-cutoffs for the 2-strap and 3-strap antennas. The iso-density and iso-intensity values for the separatrix are taken to be a time-average of all MP periods in a given $\Delta\varphi_{\mathrm{UL}}$ of the $\rho_{\mathrm{pol}} = 1$ value, as determined by CLISTE, and were found to be $n_e^{\mathrm{iso}} \approx 1.2\times10^{19}\,\mathrm{m}^{-3}$, $I_{\mathrm{CXRS}}^{\mathrm{iso}} \approx 2\times10^{16}\,\mathrm{ph}/(\mathrm{m}^2\times\mathrm{sr}\times\mathrm{s})$. The lithium beam measurements are corrected for the geometrical angle between the diagnostic LOS and the normal vector to the axisymmetric CLISTE flux surface, such that a correct normal displacement, $\vec{\xi}_n$, can be obtained. This results in displacements about $\sim$ 6% smaller than those measured by the diagnostic. The R-cutoff positions are obtained from **equation 1.26** with the assumption of a H-D mixture of 5%-95% in the plasma, and using the CLISTE axisymmetric magnetic induction field calculation. This way, the total tokamak field is included in the analysis, although, partially inaccurate due to the assumption of pure axisymmetry. For the $k_{\parallel}$ values, we will take those for which the predicted Fourier spectra of the field-aligned RF magnetic field component by plasma loaded numerical calculations finds a maximum close to the antenna Faraday screen. For the 3-strap antennas, a value of $k_{\parallel} = 11\,\mathrm{m}^{-1}(n_{\parallel} \sim 14.4$ for the used $\nu_{\mathrm{ICRF}})$ is usually representative for dipole phasing, as the power balance between the central and outer straps was kept at 1.5:1 [78]. The resulting R-cutoff density is of the order of $n_e^{\mathrm{cutoff}} \sim 7.5\times10^{18}\,\mathrm{m}^{-3}$, which is positioned beyond the X-mode reflectometry density measurements, hence, only the lithium beam and O-mode reflectometry diagnostics will be used for the analysis of the 3-strap antennas. On the other hand, the main parallel wavenumber of the 2-strap antennas spectrum, $k_{\parallel} = 7.7\,\mathrm{m}^{-1}(n_{\parallel} \sim 10)$ [78, 79] results in a lower R-cutoff density of the order of $n_e^{\mathrm{cutoff}} \sim 3.5\times10^{18}\,\mathrm{m}^{-3}$, that is well-resolved by X-mode reflectometry measurements, and thus are also included in the analysis. The $|\xi_n(\nu_0)|$ fit amplitudes as a function of the MP phasing, and the time traces for $\Delta\varphi_{\mathrm{UL}} = 0\,^\circ$ can be seen in **figure 3.6**. It is to be noted that the abscissa values in (a)-(c) are slightly different from the ones presented in **table 3.1**. The PSL model, described in **section 2.2.6**, has been incorporated into the calculations, which results in slightly different $\Delta\varphi_{\mathrm{UL}}$ values from the ones applied to the coil current waveforms of the order of $\sim 3^\circ$.
From the measurements, it is clear that $|\xi_n(\nu_0)|$ depends on the applied $\Delta\varphi_{\mathrm{UL}}$, not only for the separatrix, but also for the ICRF R-cutoffs. The maximum separatrix displacements are seen around $-90^\circ < \Delta\varphi_{\mathrm{UL}} < 0^\circ$ while the minimum displacements lie somewhere between $90^\circ \leq \Delta\varphi_{\mathrm{UL}} \leq 180^\circ$. In general, very good agreement is found at the separatrix between the

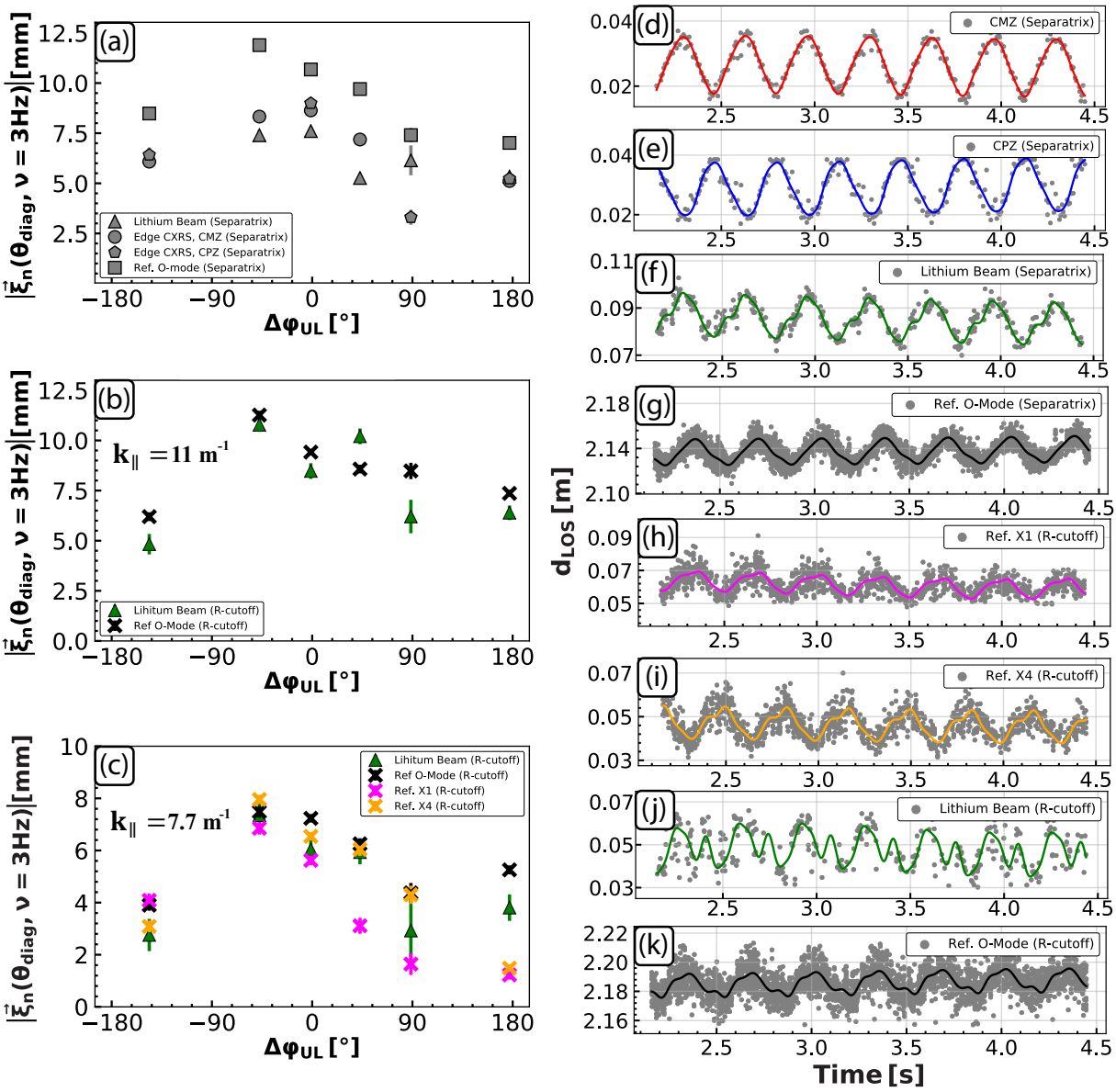

Figure 3.6: (a) Plasma normal displacements $|\vec{\xi}_n(\nu_0)|$ measured at the separatrix by the lithium beam, two CXRS diagnostics and O-mode reflectometry. (b) Plasma normal displacements at the R-cutoff ($k_\parallel = 11\,\mathrm{m}^{-1}$) measured by the lithium beam and O-mode reflectometry. (c) Plasma normal displacements at the R-cutoff ($k_\parallel = 7.7\,\mathrm{m}^{-1}$) measured by the lithium beam, X-mode reflectometers 1 and 4, and O-mode reflectometry. (d,e) CMZ and CPZ separatrix iso-intensity layer position time trace, (f) lithium beam separatrix iso-density layer position time trace, (g) O-mode reflectometry separatrix iso-density layer position time trace (h,i) Ref. X1 and X4 R-cutoff layer ($k_\parallel = 7.7\,\mathrm{m}^{-1}$) position time trace, (j) lithium beam R-cutoff layer ($k_\parallel = 7.7\,\mathrm{m}^{-1}$) position time trace, (k) O-mode reflectometry R-cutoff layer ($k_\parallel = 7.7\,\mathrm{m}^{-1}$) position time trace. The positions, d_{LOS}, of the time traces in (d-k) correspond to each diagnostic LOS for the $\Delta\varphi_{\mathrm{UL}} = 0°$ case, and the solid lines are OLS fits.

CXRS diagnostics and the lithium beam, even though they sit at different poloidal positions. The biggest scatter in the data is seen for the $\Delta\varphi_{\mathrm{UL}} = 90°$ case, which has the least number of MP periods available, and thus the poorest statistics, also resulting in larger measurement error bars. On the other hand, the O-mode reflectometer tends to overestimate the displacements in this region. In the SOL, the reflectometers and the lithium beam measure the same monotonic dependence of the R-cutoffs' displacement on the applied $\Delta\varphi_{\mathrm{UL}}$. Once again, fair agreement is found between the lithium beam and the midplane measurements from Ref. X4. and Ref. O-mode, even though they are positioned at different poloidal locations on the LFS. It is interesting to observe that the separatrix $|\xi_n(\nu_0)|$ dependence on $\Delta\varphi_{\mathrm{UL}}$ differs slightly from that of the R-cutoffs. The density profile in the SOL can be locally affected by fueling and recycling processes due to plasma-wall interactions, as well as by ICRF induced density perturbations. In the case of discharge #34634, the early detachment of a tungsten flake is seen to increase the SOL density throughout the discharge. Therefore, these differences suggest that SOL physics and machine conditioning also play a role in the amplitude of the edge plasma displacements. Finally, while the complete non-axisymmetric structure will dictate the behavior of the ICRF antenna, the SOL trend already hints to which phasings might have the biggest impact on the ICRF coupling. A detailed study of the measured loading resistance is presented in the next sections.

3.2.3 Impact of perturbed SOL density profiles on ICRF coupling

X-mode reflectometry density profiles and loading resistance measurements are presented in **figure 3.7** for the $\Delta\varphi_{\mathrm{UL}} = \{0°, 180°\}$ cases and the reference discharge. All considered time traces were analyzed with ELM-filtered data. The density profiles are plotted along the LOS coordinate of the X-mode reflectometer channels d_{LOS}, where $d_{\mathrm{LOS}} = 0$ represents the reflectometer horn antenna position. Since the reflectometer uses X-mode, the maximum resolvable density differs among channels depending on their radial location inside the vessel. A clear density oscillation is observed in front of ICRH4 when the MPs are rotated. The R-cutoff position (included in the figure is the one for the 2-strap antennas) oscillates with the density profile, and the amplitude of the oscillation directly depends on the $k_{\parallel}$ value, as it was observed in **figure 3.5**. Coherent loading resistance oscillations are registered, as measured in the two feeding lines of the same antenna. It is worth noting that when the MPs change from in-phase ($\Delta\varphi_{\mathrm{UL}} = 0°$) to out of phase ($\Delta\varphi_{\mathrm{UL}} = 180°$), the plasma response changes, decreasing the displacements in front of the antenna and thus the coupling oscillations. It is also seen that the loading resistance oscillations follow closely the density perturbation on Ref. X4, which is the reflectometer channel best aligned with the geometrical center of ICRH4.

A more comprehensive way of plotting the density perturbation vs. the loading change can be found in **figure 3.8**. There, we plot the density structure arising from the intersection of a poloidal plane with the three X-mode reflectometer channels. Since the gap between the ICRF antenna and the plasma changes poloidally, the distance between the ICRF antenna and the plane is also made to change accordingly. Three separation values are chosen for each reflectometer, $d_{\mathrm{ref.X1}} = 6\,\mathrm{cm}$, $d_{\mathrm{ref.X4}} = 4\,\mathrm{cm}$ and $d_{\mathrm{ref.X8}} = 7.25\,\mathrm{cm}$. A mapping function for the density has been used such that the oscillation can be commonly observed using the same normalized scale:

$$\tilde{n}_e^j = \frac{n_e^j - \min(n_e^j)}{\max(n_e^j) - \min(n_e^j)} \in [0, 1] \tag{3.3}$$

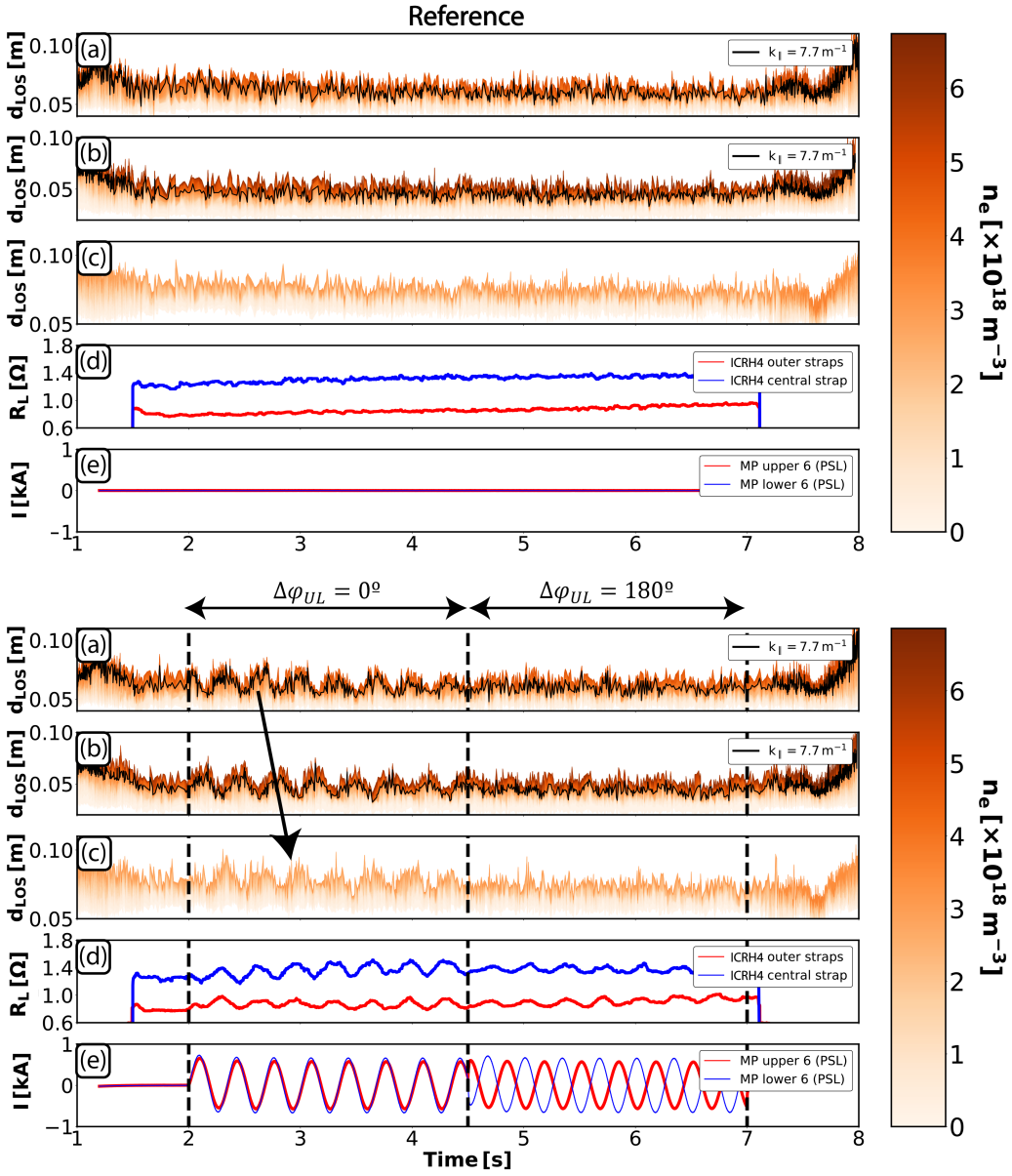

Figure 3.7: Upper plot: Discharge with no MPs. Lower plot: discharge with $\Delta\varphi_{\mathrm{UL}} = \{0°, 180°\}$. (a,b,c) n_e measurements at the different reflectometer channels Ref. X1, Ref. X4, Ref. X8 plotted along lines of sight. (d) Loading resistance measured at the feeders of the ICRH4 three-strap antenna. A sliding median filter has been applied for display purposes. (e) Applied currents to the MPs, corrected for the PSL attenuation. The tilted arrow in (a,b,c) marks the direction of rotation of the kink displacement along the antenna front.

with $j = 1, 4, 8$. The toroidal mode structure of the perturbation can be well resolved due to the high-enough sampling frequency of the reflectometers during the MP rigid rotation. On the other hand, the poloidal mode structure is poorly resolved, since only three measuring positions cover approximately 0.8 m of vertical distance. Nevertheless, the 3D density structure can be seen traveling across the antenna from top to bottom, as marked by the tilted arrows. The antenna loading resistances have been fitted with an OLS fit, in the same fashion as indicated before, in order to obtain the times when the local maxima happen (dashed red and blue lines in **figure 3.8**). These lines for ICRH4 have been extended upwards to the density plot for

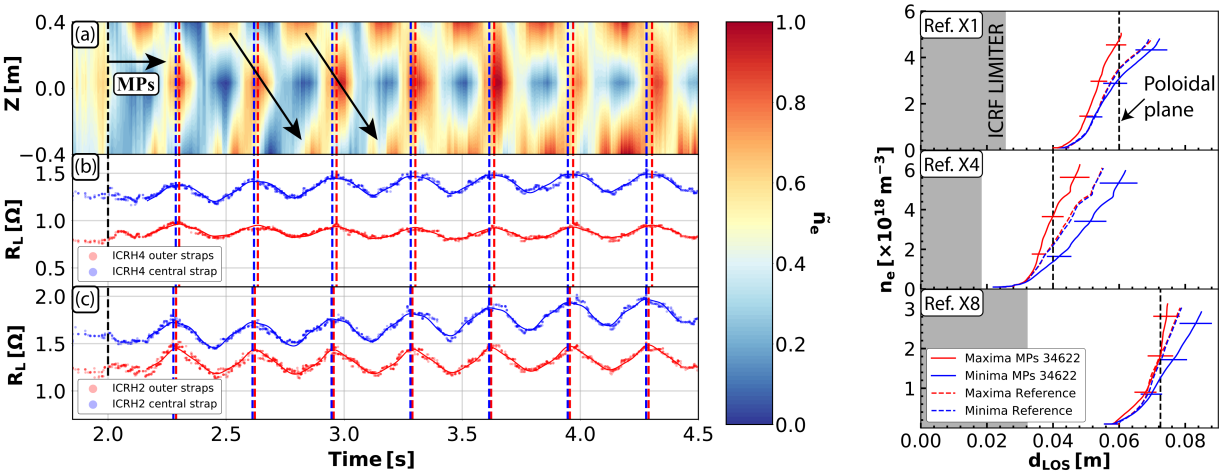

Figure 3.8: Left: (a) Density contour from Ref. X1, Ref. X4 and Ref. X8 as intersected by a poloidal plane with chosen distances to the reflectometer horns of $d_{ref.X1} = 6\,cm$, $d_{ref.X4} = 4\,cm$ and $d_{ref.X8} = 7.25\,cm$, (b) loading resistance time traces of ICRH4 with local maxima and minima, (c) loading resistance time traces of ICRH2 with local maxima and minima. Right: 1D density profiles from Ref. X1, Ref. X4 and Ref. X8 at maximum and minimum approach to ICRH4. The profiles for discharge #34622 with MPs are included as solid lines, while the profiles from #34632 without MPs are included as dashed lines.

comparison. The maxima are well correlated with the density perturbation when it is closer to the antenna center. We hypothesize that this is due to the ballooned structure of the perturbation on the LFS of the tokamak, thus covering a larger portion of the ICRF antenna the closer it is to its center. On the right, one-dimensional density profiles are plotted for the three reflectometer channels, representative of local maximum and minimum approach to the ICRF antenna position when the MP phasing was set to $\Delta\varphi_{UL} = 0°$. The profiles were calculated by performing local averages centered at each extremum over 50 ms windows. All locally averaged profiles are then averaged together for all the maxima and minima separately. The density profiles for the reference discharge with no MPs are evaluated in the same way, and included as dashed lines. Error bars are added for some points as one standard deviation of the used profiles. Significant displacements of the density profiles are seen close to the ICRF antenna in the MP case, while for the reference case the profiles have a steady position. In the next section, we will investigate how the different MP phasings affect the ICRF antennas loading resistance.

3.2.4 Loading resistance change as a function of applied MP phasing

At a constant safety factor q, pressure profile and MP coil currents, the amplitude and topology of the plasma kink displacement vary as a function of the applied poloidal mode spectra from the MP field, which we tune through different $\Delta\varphi_{UL}$. In the same fashion as observed in **figure 3.7**, the loading resistance variation of each feeder will depend on the plasma displacements. We perform an OLS fit to the loading resistances of each antenna feeder for every one of the applied $\Delta\varphi_{UL}$ phasings, such that the amplitude of the coupling variation can be obtained. The procedure is displayed in **figure 3.9**, where the loading resistances are fitted for the case of $\Delta\varphi_{UL} = 0°$. The loading resistances for the discharge with no MPs during the same time period are added for comparison. A sliding median filter with a window size of 51 points is performed to the no-MP time traces in order to better visualize the baseline level of the loading. Aside

from the harmonic oscillation when the MPs are present, it is also observed that, on average, the loading resistance is higher with MPs than without them, as already observed in previous studies [22, 69]. This observation is consistent with the plasma density increase in the SOL due to the pump-out effect, which is visible in the line-integrated density measurements in **figure 3.4**. In the lower plot, we present the loading variation in percentage as a function of the applied $\Delta\varphi_{\mathrm{UL}}$. Here, ΔR_L is the amplitude of the fundamental ν_0 component of each feeder and $\langle R_L \rangle$

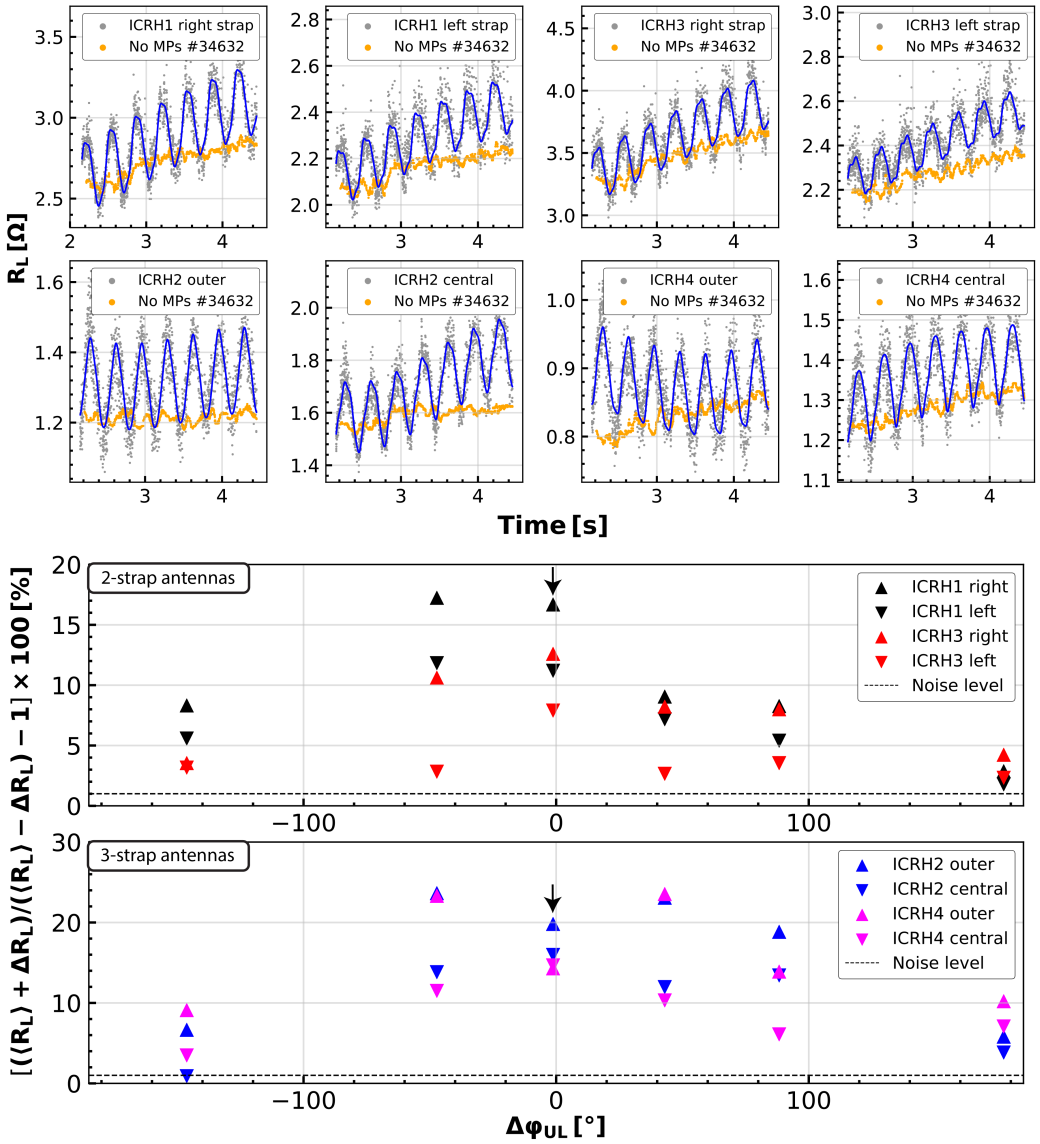

Figure 3.9: Upper plots: loading resistance of each ICRF antenna feeder and OLS fit for the case of $\Delta\varphi_{\mathrm{UL}} = 0°$ (blue), and reference with no MPs (orange). A sliding median filter with a 51 point window has been applied to the reference case for display purposes. Lower plot: loading resistance percentage change for the (upper) 2-strap antennas and (lower) 3-strap antennas. *Left* and *right* straps from the 2-strap antennas, as seen from the antenna reference frame towards the plasma. The outer straps in each 3-strap antenna are connected to the same feeder. The arrow marks the $\Delta\varphi_{\mathrm{UL}} = 0°$ amplitudes of the shown loading resistance time traces in the upper plot. The marker size is representative of the OLS 1σ uncertainty.

is the loading resistance time average of the considered window. Thus, the minimum loading resistance for a given $\Delta\varphi_{\mathrm{UL}}$ is taken to be $\langle R_L\rangle - \Delta R_L$ and the maximum $\langle R_L\rangle + \Delta R_L$. The error bars representing the uncertainty of the OLS fit alone are comparable to the marker size, and thus have not been included. The noise level, marked as a horizontal dashed line on the lower plot, is calculated by performing the same OLS fit to the loading resistances for the discharge with no MPs, and then taking the average over the antenna pairs.

An interesting observation is that the loading resistance baseline increases during the discharge, especially for the 2-strap antennas. This is due to the general electron density increase in the plasma over time, also seen in **figure 3.4**. Since the baseline variation is effectively accounted for and removed by the polynomial fit, it is assumed throughout the analysis that the amplitudes of the OLS fit represent an average value of the loading resistance amplitude over the considered time trace. From the performed analysis, a clear dependence of the loading resistance change on the applied $\Delta\varphi_{\mathrm{UL}}$ is observed well above the noise level. This corroborates the picture of the coupling change being directly correlated to the plasma kink displacements. A maximum loading resistance change of $\sim 25\%$ is reached, with a similar $\Delta\varphi_{\mathrm{UL}}$ dependence between the 2-strap antennas and the 3-strap antennas. The 3-strap antennas experience larger coupling changes, as it would be expected from their higher $k_{\parallel} \sim 11\,\mathrm{m}^{-1} > 7.7\,\mathrm{m}^{-1}$ combined with the fact that the displacements decay radially in the SOL. Even larger coupling changes would be expected, well correlated with larger plasma displacements, if the MP field attenuation by the PSL becomes smaller, e.g. with slower MP rotation frequencies, or if larger currents are applied to the MP coils, provided we are not close to non-linear saturation.

3.2.5 Experimental scaling of antenna loading resistance with cutoff distance

It is instructive to compare the experimental data obtained in these non-axisymmetric scenarios against one-dimensional analytical and experimentally-derived formulas, often used to describe the scaling behavior of the loading resistance with plasma parameters. In particular, we would like to know if the three-dimensionally perturbed cases behave similarly to radial scans of the (axisymmetric) plasma position in the limit of very small perturbations, and how large does the non-axisymmetry need to become before large deviations occur. For the comparison, we build data sets based on the displacements measured by the different diagnostics. We, therefore, use the density data measured by Ref. X4, Ref. O-mode and the lithium beam for the 2-strap antennas and the Ref. O-mode and lithium beam for the 3-strap antennas. The 1D-cutoff oscillation amplitudes are taken to be $\Delta d_{\mathrm{cutoff}}/2$. Again, we consider $R_L^{(1)} = \langle R_L\rangle - \Delta R_L$ the minimum loading resistance and $R_L^{(2)} = \langle R_L\rangle + \Delta R_L$ the maximum loading resistance for a given MP phasing. We will also evaluate the data sets for the different ICRF antennas separately and grouped by antenna type. Median values of the loading resistance are computed over the feeders of the antennas for each MP phasing and then fitted to an exponential function of the shape $f_{\mathrm{fit}}(d) = e^{-\alpha\Delta d_{\mathrm{cutoff}}}$ from which the α value is obtained. The motivation behind this fitting function stems from the derived expressions in [80, 81]. The radiation impedance of an ICRF antenna depends on the optical properties of the medium in front of it. If an evanescent region exists, we obtain from the cold plasma theory a scaling for the coupling resistance such that:

$$\mathrm{Re}(Z_{\mathrm{rad}}) = R_c \propto e^{-\beta\eta}, \text{ with } \eta = \int_{\Omega_e} k_{\perp} dl \tag{3.4}$$

the optical thickness of the medium, Ω_e the domain that bounds the evanescence region, β a constant that depends on the assumptions made in the derivation and R_c the coupling resistance, equal to the real part of the radiation impedance. In order to evaluate this integral, knowledge of the RF near fields is necessary. Some common approximations rely on stating $|k_\perp| \sim |k_\parallel|$, since in vacuum $|k_\parallel| \gg |k_0|$, with k_0 the free-space wavenumber. Here, we acknowledge the dependence of η on the distance between the strap and the cutoff (size of the coupling region) and retain the functional form $R_L \propto e^{-\alpha d_{\text{cutoff}}}$ for convenience. The fitting is performed with two statistical tools: OLS and orthogonal distance regression (ODR). OLS minimizes the squared vertical distance between the fit and the loading resistance measurements in order to determine α. ODR, on the other hand, finds the estimators which minimize the squared errors between the fit and observed points for both the dependent and independent variables $\{k_\parallel \Delta d_{\text{cutoff}}, R_L^{(2)}/R_L^{(1)}\}$ simultaneously. This approach should be more robust than OLS for obtaining the α estimator. The results for both approaches can be visualized in **table 3.2**. The covariance matrix is computed both for OLS and ODR, and a 99% confidence interval is constructed assuming the samples to be normally distributed.

Data set	$\alpha_{\text{OLS}} \pm 2.58\sqrt{\text{Var}(\alpha_{\text{OLS}})}$	$\alpha_{\text{ODR}} \pm 2.58\sqrt{\text{Var}(\alpha_{\text{ODR}})}$
ICRH1 (Ref. X4)	8.49 ± 1.40	8.96 ± 0.42
ICRH1 (Lit. Beam)	8.72 ± 2.51	9.04 ± 1.16
ICRH1 (Ref. O)	7.52 ± 2.37	7.91 ± 0.36
ICRH3 (Ref. X4)	5.39 ± 1.63	5.89 ± 0.33
ICRH3 (Lit. Beam)	5.62 ± 1.90	6.01 ± 0.79
ICRH3 (Ref. O)	4.95 ± 1.38	5.30 ± 0.29
ICRH1 and ICRH3 (Ref. X4)	**7.18 ± 0.98**	**7.48 ± 0.37**
ICRH1 and ICRH3 (Lit. Beam)	**7.40 ± 1.90**	**7.57 ± 0.97**
ICRH1 and ICRH3 (Ref. O)	**6.40 ± 1.74**	**6.63 ± 0.32**
ICRH2 (Lit. Beam)	8.03 ± 2.27	8.12 ± 0.50
ICRH2 (Ref. O)	7.49 ± 2.27	7.50 ± 0.26
ICRH4 (Lit. Beam)	7.47 ± 0.53	7.47 ± 0.47
ICRH4 (Ref. O)	6.89 ± 1.32	6.99 ± 0.27
ICRH2 and ICRH4 (Lit. Beam)	**7.79 ± 1.42**	**7.73 ± 0.48**
ICRH2 and ICRH4 (Ref. O)	**7.22 ± 1.70**	**7.14 ± 0.26**

Table 3.2: α exponent factors in $[\text{m}^{-1}]$, computed for all ICRH antennas on the basis of the different diagnostics. Results are obtained from OLS and ODR with a 99% confidence interval. The exponents arising from fits to both 2-strap antennas and both 3-strap antennas are highlighted.

Among the mentioned formulas found in the literature, we first turn our attention to the analytically derived one proposed in [80], which we term the *Bilato* scaling. This formula is based on the cold plasma dielectric tensor formulation. The plasma is assumed homogeneous in toroidal and poloidal directions and the antenna is assumed ideal, producing a single $k_\parallel$ value. It is further assumed that the only excited plasma mode is the fast wave, and that $n_\perp^2$ increases linearly from the antenna to the R-cutoff within the *linear model* derivation. In order to allow the flow of energy from the antenna to the cutoff, the poloidal electric field of the fast wave is decomposed in a sum of two opposite-"propagation" evanescent waves. The coupled power can then be expressed in terms of the plasma admittance, and in the limit of low optical thickness ($0 < \eta < 3$)

it reduces to:

$$P_{\text{trans}} \approx P_0 e^{-1.1 k_{\parallel} d_{\text{cutoff}}} \tag{3.5}$$

with P_0 the power corresponding to the amplitude of the current at the straps and d_{cutoff} the distance from the antenna to the R-cutoff. Neglecting losses on the antenna conductors and transmission lines, **equations 1.46** and **3.5** can be used to give an estimate of the loading resistance change due to a radial movement of the cutoff position, Δd_{cutoff}, such that:

$$\Delta R_L = \frac{R_L^{(2)}}{R_L^{(1)}} = e^{-1.1 k_{\parallel} \Delta d_{\text{cutoff}}} \tag{3.6}$$

The results of the comparison between the experimental scaling and this analytical formula can be seen in **figure 3.10**. It is observed that the exponent correctly reproduces the data within the given uncertainties for ICRH1, while it overestimates the changes of the other data sets.
We now further compare the data to numerically and experimentally-derived scalings found in the literature. A statistical analysis of the ASDEX Upgrade 2-strap antennas coupling properties, combining L-mode and H-mode discharges, was performed in [22]. The numerically computed coupling resistance (R_c) from the Rsolver code was related to specific features of the experimentally measured density profiles. A scaling law was derived of the shape:

$$\begin{aligned} R_c^{\text{Rsolver}} \propto\ & e^{-11.5 d_{\text{cutoff}} + 3.9 d_{\text{min}} - 0.064 \nabla_{\text{eff}}} \\ & e^{-0.004 \nabla_{\text{max}} + 0.0036 n_{\text{edge}}} \end{aligned} \tag{3.7}$$

where d_{min} is the distance between the main R-cutoff and the minimum density gradient, $\min(\nabla n_e)$, used to characterize the effect of the density shoulder that often appears in H-mode density profiles. $\nabla_{\text{eff}} = (n_{\text{edge}} - n_{\text{co}})/(r_{\text{edge}} - r_{\text{co}})$ with n_{edge} defined at the pedestal top following the convention described in [22] and r_{edge} its position, $n_{\text{co}} = 3.5 \times 10^{18}\ \text{m}^{-3}$ the main R-cutoff density for the 2-strap antennas and r_{co} its position. ∇_{max} is defined as the maximum density gradient of the profile. A linear relationship was also found between the actual loading resistance as computed by the TOPICA code [83] and the coupling resistance computed by Rsolver, such that $R_L^{\text{TOPICA}} \sim 6.3 R_c^{\text{Rsolver}} - 0.92$. We take the lower limit of this scaling, i.e. $R_L^{\text{approx}} \sim 6.3 R_c^{\text{Rsolver}}$, since it can be shown that $\Delta R_L^{\text{approx}} \leq \Delta R_L^{\text{TOPICA}}$ for $R_c^{\text{Rsolver,2}} / R_c^{\text{Rsolver,1}} \geq 1$, yielding:

$$\begin{aligned} \Delta R_L^{\text{approx}} \propto\ & e^{-11.5 \Delta d_{\text{cutoff}} + 3.9 \Delta d_{\text{min}} - 0.064 \Delta(\nabla_{\text{eff}})} \\ & e^{-0.004 \Delta(\nabla_{\text{max}}) + 0.0036 \Delta n_{\text{edge}}} \end{aligned} \tag{3.8}$$

The evaluation of **equation 3.8** is only possible with a diagnostic that covers the region from the far SOL to the pedestal top. We use lithium beam profiles to give an estimate of the importance of each term in the exponential factor under our experimental conditions. All discharges in **table 3.1** are investigated. We again produce representative n_e profiles, analogously to previously performed with the X-mode reflectometers. First, the time traces are ELM-filtered and local maxima and minima density profiles are computed for each MP cycle as the median of the extrema neighboring profiles over ~ 40 ms. Next, the median is computed again over all the local maxima and minima in order to yield representative profiles for a given $\Delta\varphi_{\text{UL}}$. The result of this procedure is seen in **figure 3.11** for the $\Delta\varphi_{\text{UL}} = 0^\circ$ case. Points for $n_{\text{edge}}, \max(\nabla n_e), \min(\nabla n_e)$

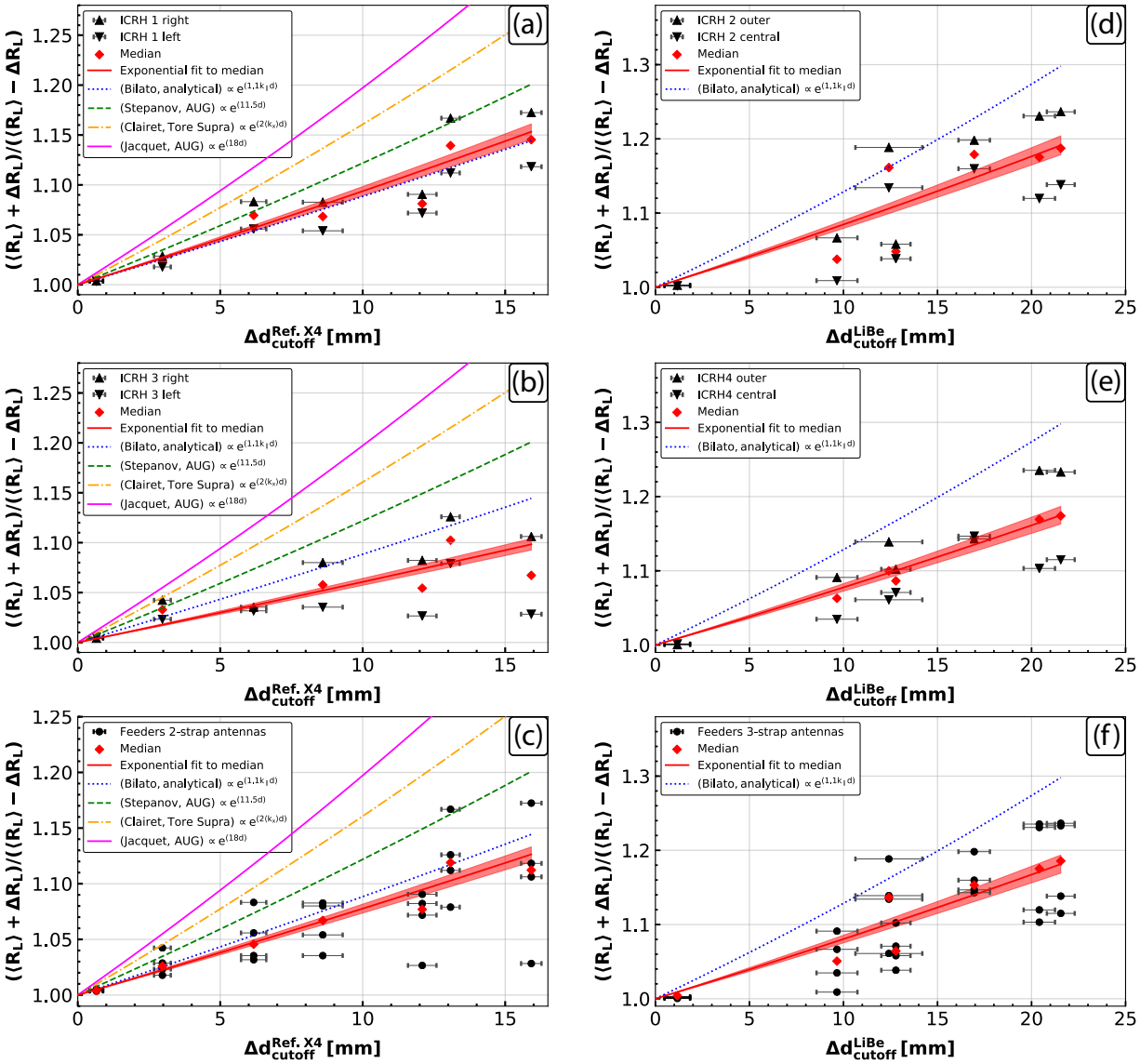

Figure 3.10: Average change of loading resistance as a function of the average R-cutoff displacement as measured by Ref. X4 for the 2-strap antennas and the lithium beam for the 3-strap antennas. A fit using ODR on f_{fit} is performed. (a,b,c): Using ICRH1 alone, ICRH3 alone and the combined data set. (d,e,f): Using ICRH2 alone, ICRH4 alone and the combined data set. The formula derived in [80] is added as a blue dashed curve. The scaling predicted in [22] is added as a green dashed curve. The scaling predicted in [81] is added as a yellow dashed curve. The scaling measured in [82] is added as a magenta solid curve. The marker size is representative of the vertical OLS 1σ uncertainty.

are added as per definition in [22]. It is found that in all studied cases $|0.0036\Delta n_{\text{edge}}| \ll |-11.5\Delta d_{\text{cutoff}} + 3.9\Delta d_{\text{min}} - 0.064\Delta(\nabla_{\text{eff}}) - 0.004\Delta(\nabla_{\text{max}})|$, and hence can be safely neglected. Among the rest of parameters, $|-11.5\Delta d_{\text{cutoff}}|$ is usually much larger than $\epsilon = |3.9\Delta d_{\text{min}} - 0.064\Delta(\nabla_{\text{eff}}) - 0.004\Delta(\nabla_{\text{max}})|$, except in the cases where Δd_{cutoff} is very small, like in the $\Delta\varphi_{\text{UL}} = 180°$ case, or the density shoulder is not clearly defined and thus cannot be captured by the $\min(\nabla n_e)$ condition. The evaluation of all the MP phases yielded:

$$\left\langle \frac{|-11.5\Delta d_{\text{cutoff}}|}{\epsilon} \right\rangle \sim 24.5 \pm 18.9 \tag{3.9}$$

where the uncertainty represents 1σ. We hence estimate the main parameter to be Δd_{cutoff} and further reduce $\Delta R_L^{\text{approx}} \sim e^{-11.5\Delta d_{\text{cutoff}}}$. This scaling, which we term *Stepanov* scaling, approximates in the lower limit the expected loading resistance change computed by TOPICA for the 2-strap antennas. It is also seen in **figure 3.10**, that it overestimates the measurements here presented, only agreeing occasionally with some of the feeders. Naturally, this scaling can only be applied to the 2-strap antennas, since it was performed prior to the installation of the 3-strap antennas in ASDEX Upgrade and the statistical analysis was never repeated for these.

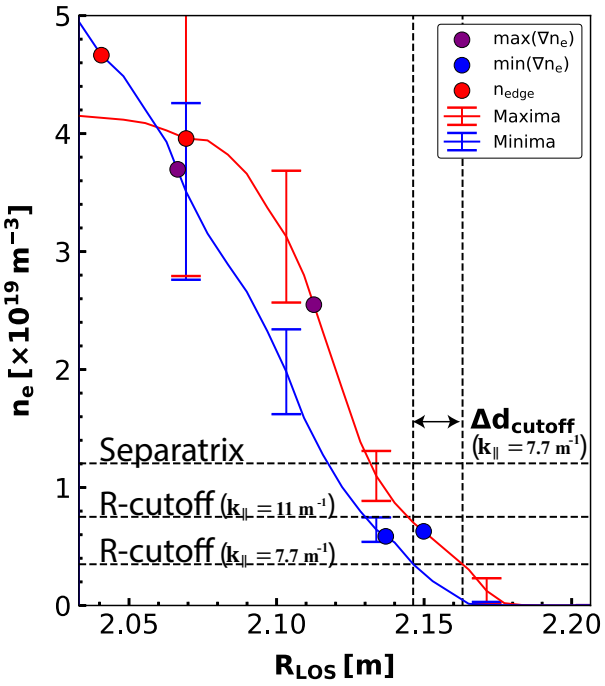

Figure 3.11: Lithium beam density profiles for discharge #34622, $\Delta\varphi_{\text{UL}} = 0°$. Local maxima and minima profiles are computed for each MP cycle taking the median over ~ 40 ms. The final profiles are computed as the median of all the local extrema profiles.

A purely experimental scaling was also derived for the ASDEX Upgrade 2-strap antennas when studying the influence of different gas puff locations on the loading resistance [82]. The O-mode reflectometer was utilized to find the distance from the antenna to the R-cutoff, and this was correlated to the loading resistance measured by a set of voltage and current probes in the unmatched transmission lines (which are not used in this thesis). The scaling, which we term *Jacquet* scaling, was derived by uniquely using H-mode discharges fueled with divertor gas puff. The reported exponent factor was $\alpha \sim 18\,\text{m}^{-1}$, i.e., $\Delta R_L \propto e^{-18 d_{\text{cutoff}}}$. This factor greatly overestimates the measured loading resistance change for all the antenna feeders. Despite this fact, it will be seen in **section 3.2.6** that this scaling is in very good agreement with 1D ICRF coupling simulations.

In Tore Supra, the measured loading resistance of a database of ICRF heated discharges could be fit with the exponent $\alpha \sim 17.3\,\text{m}^{-1}$ [81]. This scaling compares favorably to the one found in ASDEX Upgrade ($\alpha \sim 18\,\text{m}^{-1}$), which is further accentuated by the fact that both were obtained with 2-strap antennas in dipole phasing, despite the slightly different $k_\parallel$, i.e., $k_\parallel^{\text{Tore Supra}} \sim 9.1\,\text{m}^{-1} > 7.7\,\text{m}^{-1}$. A generalization of the experimental scaling was proposed from purely theoretical grounds stemming from the cold plasma approximation, such that: $R_L \approx e^{-2\langle k_x\rangle d_{\text{cutoff}}}$. Here, $\beta = 2$ and $\eta \sim \langle k_x\rangle d_{\text{cutoff}}$ in **equation 3.4**. We will call this relation the *Clairet* scaling. The value for $\langle k_x\rangle$ was taken to be approximately the maximum $k_\parallel$ of the radiated power spectrum in the plasma, as computed by the ICANT code. The change in loading resistance would be:

$$\Delta R_L = e^{-2\langle k_x\rangle \Delta d_{\text{cutoff}}} \tag{3.10}$$

We utilize the RAPLICASOL code, as described in the next section, in order to better estimate the radiated power $\max(k_\parallel)$ for the ASDEX Upgrade 2-strap antenna coupling to an axisymmet-

ric density plasma. We assume the fast wave to carry most of the radiated power, and therefore, we compute the power spectral density (PSD) of the field-aligned RF magnetic field component, which can be seen in **figure 3.12**.

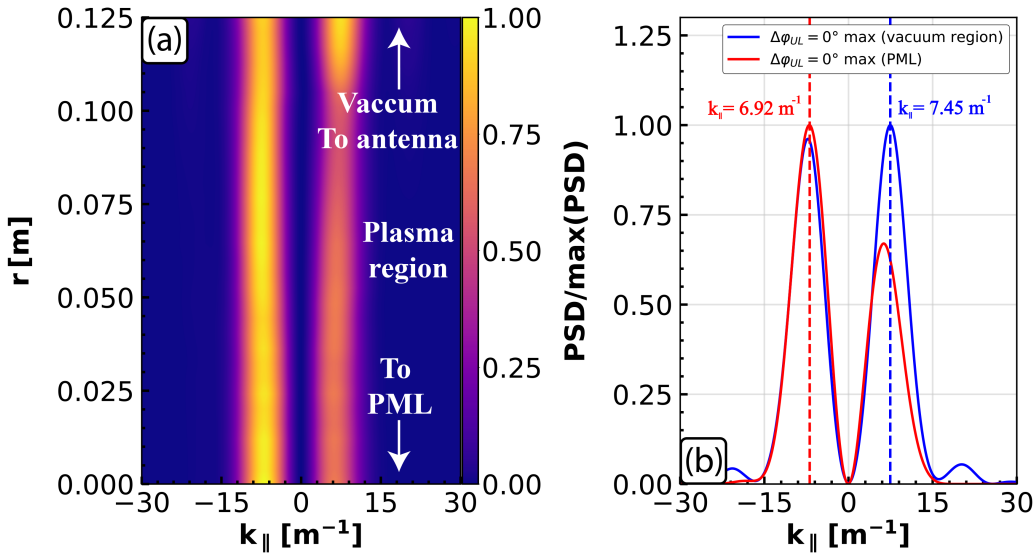

Figure 3.12: (a) PSD of the RF magnetic field component for a field-aligned 2D plane intersecting the coupling region. (b) PSD as in (a) for $r = 0.125\,\mathrm{m}$ (inside the vacuum region) and $r = 0\,\mathrm{m}$, at the plasma-PML interface.

The vacuum profile is evaluated in the private region in front of the ICRF antenna, close to the Faraday screen (FS). The PML profile is evaluated at the end of the simulation domain, where outward radiation boundary conditions exist, and therefore, where we consider the power to be coupled to the core. We have obtained $\max(|k_{\parallel}^{\mathrm{FS}}|) \sim 7.45\,\mathrm{m}^{-1}$, in good agreement with the value used in the experimental determination of the R-cutoff. We therefore approximate $\langle k_x \rangle \sim \max(|k_{\parallel}^{\mathrm{FS}}|)$ on the basis that $|k_{\parallel}| \gg |k_0|$, and included this value in the scaling displayed in **figure 3.10**. It can be seen that this theory-based scaling also overestimates the measured change in loading resistance. Yet, it approximates fairly well the experimental measurements in ASDEX Upgrade under axisymmetric plasma conditions predicted by the Jacquet scaling.

With the presented comparison, we find that the diverse scalings overestimate the measured loading resistance change in the investigated non-axisymmetric configurations. The best agreement is found with Bilato's scaling for the 2-strap antennas. Nevertheless, this scaling clearly departs from the other experimental and simulation observations reported in the literature. Particularly, it strongly diverges from the experimental 1D scaling in axisymmetric conditions obtained by Jacquet. A marginal improvement can be found if the 2-strap antenna current spectrum $k_{\parallel}^{\mathrm{current}} \sim 9.25\,\mathrm{m}^{-1}$ is used instead (as suggested in [80]), leading to $R_L \propto e^{-10 d_{\mathrm{cutoff}}}$. This departure could be attributed to the assumption that $n_{\perp}^2$ increases linearly from the strap to the cutoff. In reality, it is likely that a sharp decrease in plasma density occurs inside the ICRF limiter. Under these circumstances, the *step model* also proposed in [80] could be a better representation of reality, but has not been here investigated.
It should also be remarked that the experimental scaling here presented from Jacquet, and the hybrid one from Stepanov, were obtained under different (and axisymmetric) plasma conditions,

with unknown S-matrices, making a comparison with our measured data only qualitative, but still valuable. In addition, we have purposely not included error bars for the scaling laws, since even though they would help to improve the agreement, our objective is simply to compare the measured data sets against the general trend. We can also attempt to give an explanation to the measured scaling deviation from the ones of the literature in the following manner: In opposition to radial movements of axisymmetric plasmas, where the whole plasma column is moved towards/away from the ICRF antenna, the poloidal and toroidal inhomogeneities brought by the MP plasma deformation can make part of the plasma to be closer to the antenna, and another part to be farther away simultaneously with respect to the axisymmetric case. It can be seen in **figure 3.8** that when the plasma is the closest to the antenna center, it is farther away at the antenna top and bottom. An "integration" of this 3D density structure by the relatively large (compared to the plasma size) ASDEX Upgrade antenna could, therefore, result in a smaller net effect on the coupling characteristics. Thus, one would expect the loading changes to scale slower with the measured 1D cutoff deformation amplitude than those produced by axisymmetric movements of the plasma volume. In other words, if the change in the 3D deformation could be represented by a single "effective" integrated one-dimensional displacement $\langle \Delta d_{\mathrm{cutoff}} \rangle^{\mathrm{eff}}$, we would likely find $\langle \Delta d_{\mathrm{cutoff}} \rangle^{\mathrm{eff}} < \Delta d_{\mathrm{cutoff}}$. A similar integration was already attempted in [84] for an axisymmetric plasma with changing triangularity, and when weighted with a filtering factor to account for the exponential evanescent behavior, resulted in a consistent scaling of the measured loading resistance. This approach could also shed some light on why the found radial decay parameters, α, are very similar between the 2-strap and the 3-strap antennas, which is, in principle, an unexpected result due to their different $k_{\parallel}$. Such study would, however, require precise knowledge of the 3D magnetic topology and needs to be supported by dedicated MHD and/or transport simulations.
It can also be noted that the loading resistance change measured in different feeders scatters more significantly the higher the cutoff oscillation amplitude becomes. Systematic errors in the V_{max} determination between different feeders can become more apparent the larger the perturbation grows. Furthermore, cross-coupling terms in the unknown S-matrices play a role in these differences, which is difficult to assess since no direct measurements of the antennas S-matrices are currently possible. It is plausible, that the larger scatter between the feeders' experimental data can be partly explained by the poloidal and toroidal effects on coupling becoming of greater importance. In this situation, it is not possible to approximate the coupling change in each feeder accurately with a single 1D scaling anymore (i.e. a single value of $\Delta d_{\mathrm{cutoff}}$), but rather, a functional description of the S-matrix dependence on the 3D density profile becomes mandatory.

To summarize, it is clear from these results that reducing the 3D density profile to 1D by neglecting toroidal and poloidal inhomogeneities would result in a notable deviation when assessing the change in antenna loading resistance. In order to better elucidate the impact of arbitrary plasma asymmetries on ICRF coupling, and other important antenna performance quantities, dedicated full-wave modeling is performed in the next sections: first in 1D approximation in **section 3.2.6** and, finally, in full 3D geometry in **Chapter 4**.

3.2.6 ICRF simulations using the COMSOL based RAPLICASOL code

In the previous section, we investigated the scaling of the experimentally measured loading resistance change with respect to the 1D R-cutoff movements measured by different diagnostics.

We found that the derived 1D scaling deviated from previous experimentally-derived and analytical scalings found in the literature. In this section, we focus on the numerical change of the loading resistance when 1D density profiles are fed into an ICRF antenna coupling code. By doing so, we want to test our expectation that considering a 1D density profile for the whole ICRF coupling region, even if representative of the OMP measurements, is not enough to replicate the experimental results, which are inherently of three-dimensional nature. Furthermore, we can test how large the deviation is between the experimental results and the numerical predictions. We will use for the simulations the COMSOL based RAPLICASOL code, introduced in **section 2.2.8**. So far, only flat models of the ASDEX Upgrade antennas had been used in RAPLICASOL studies. In order to be as close as possible to the experimental conditions, and to avoid artificial geometric transformations of the density profile from the tokamak toroidal geometry to the usual simulation flat geometry, a new curved model of the ASDEX Upgrade 2-strap antenna has been developed and used, in addition to the usual flat model for comparison. Both models are presented in **figure 3.13**. We computed with the new curved antenna model the PSD of the field-aligned RF magnetic field component, which has been already introduced in **figure 3.12**. The obtained $\max(k_{\parallel}) \sim 7.45\,\mathrm{m}^{-1}$ in the vacuum region is in good agreement with previous HFSS models of the ASDEX Upgrade 2-strap antennas [78], giving confidence in its robustness. Furthermore, we have constructed this RAPLICASOL model following a CAD design of the actual ASDEX Upgrade 2-strap antenna, and the geometrical features were further compared with the antenna used in the TOPICA code.

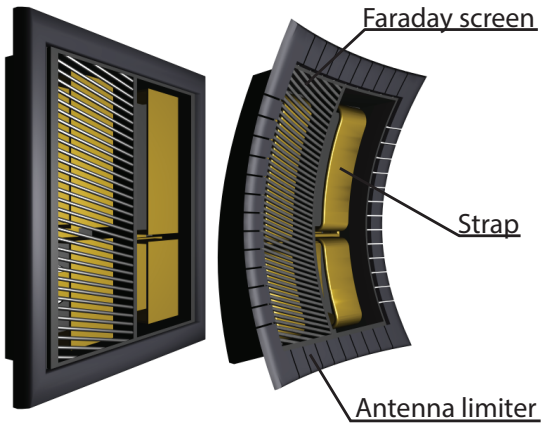

Figure 3.13: RAPLICASOL flat and curved models of the ASDEX Upgrade 2-strap antenna.

In order to provide representative density profiles for the given experimental conditions, we will use the lithium beam diagnostic, which most extensively covers the ICRF coupling region. We follow the same procedure previously introduced: first, an OLS fit was performed to the ELM-filtered lithium beam time traces for each $\Delta\varphi_{\mathrm{UL}}$, and the time points of local density maxima and minima were found, corresponding to the minimum and maximum antenna-R-cutoff gap distance. Second, all density profiles in a given time-window centered at the local extrema are averaged. Third, all the maxima, and, all the minima profiles are averaged together. The time window length is adjusted in order to ensure that the final profiles preserve, as close as possible, the same R-cutoffs and separatrix displacements as the ones obtained via OLS in **figure 3.6**. A time window of ~ 40 ms was found to yield the closest agreement between OLS and the profile reconstruction procedure. Since the angle between the lithium beam LOS and the normal vector to the axisymmetric separatrix is of the order of $\alpha^{\mathrm{libe}} \sim 20°$, $\cos(\alpha^{\mathrm{libe}}) \sim 0.94$, this is regarded as a second-order contribution and has not been corrected for in the reconstruction. The resulting density profiles are displayed in **figure 3.14**.

The coupling simulations were performed by considering a 1D induction field varying as $|B| \propto |B_0|R_0/R$, with $|B_0| = 2.5\,\mathrm{T}$ the on-axis induction field, and $R_0 = 1.65\,\mathrm{m}$ the torus major radius. A constant induction field angle of 11° is imposed over the simulation domain, in the tilt direction of the Faraday screen bars. In the future, this simplification can be removed by adding a

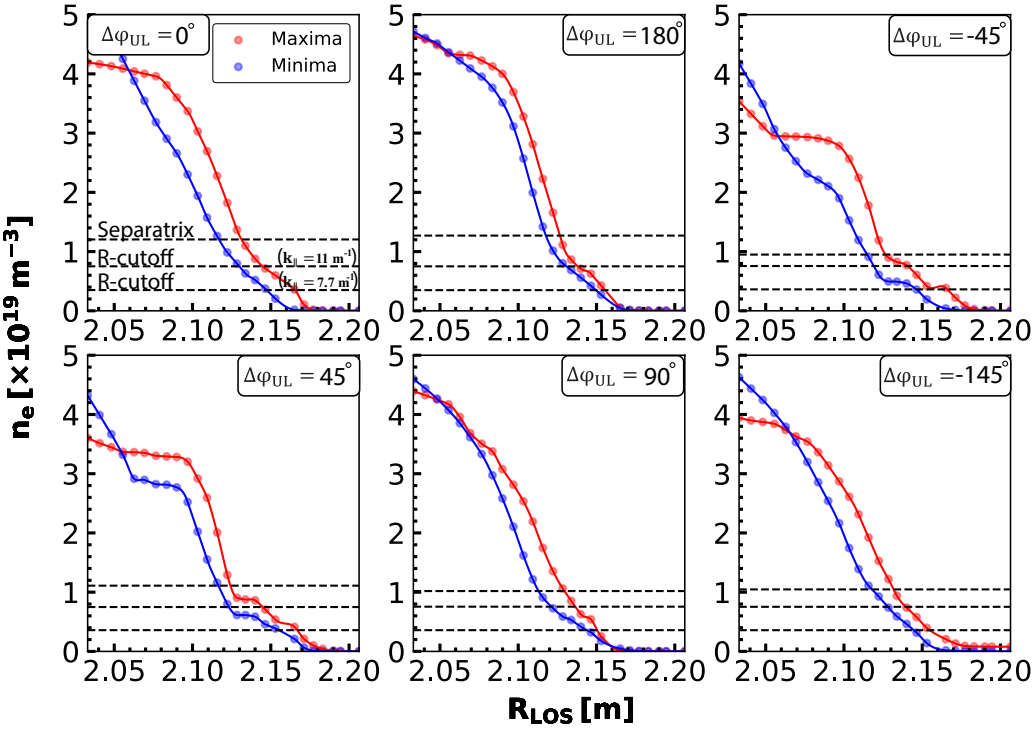

Figure 3.14: $n_e = f(\Delta\varphi_{\mathrm{UL}})$ profiles computed from the lithium beam diagnostic. (Red) Maximum, i.e. closest approach of the plasma to the ICRF antenna, (blue) minimum, i.e. largest separation between the plasma and the ICRF antenna. Separatrix and R-cutoff densities are computed for each case and marked as dashed lines.

realistic field from a non-axisymmetric MHD equilibrium calculation. Vacuum conditions are imposed in the domain bounded by the outer wall and $n_e = 1 \times 10^{17}\,\mathrm{m}^{-3}$ in order to avoid the lower hybrid resonance, which cannot be handled with the used cold plasma dielectric tensor within the COMSOL finite element formulation. A maximum density of $n_e^{\max} = 2.5 \times 10^{19}\,\mathrm{m}^{-3}$ is set in the plasma domain in order to ensure no density gradients exist in the plasma-PML interface. The curved model is run with the direct solver, whereas the flat model is converged with the iterative solver, setting 1% relative tolerance. The mesh was set with hexahedral elements of a characteristic radial length of $\sim$ 1 cm for the curved model, whereas the flat model uses tetrahedral elements with a radial length of $\sim$ 2 cm. Both resolutions should be enough to resolve the perpendicular wavelength of the fast wave in the coupling region, which for our conditions is of the order of $\min(|\lambda_\perp|) \sim 15$ cm. Two sets of simulations are performed: using the profiles in **figure 3.14** for comparison between the maximum and minimum approach to the ICRF antenna per MP phasing, and a radial scan using only the density profile for $\Delta\varphi_{\mathrm{UL}} = 0°$ "maxima". The radial scan was performed by outward shifting the density profile in steps of 4 mm and thickening the vacuum layer in each iteration by the same width. With these two sets, we are able to distinguish between loading resistance changes due to a pure radial shift of the density profile from coupling changes that include variation in the density gradients. The computed S-matrices are transformed into loading resistances by assuming a perfect coaxial line with $Z_0 = 25\,\Omega$ characteristic impedance, such that [20]:

$$\begin{pmatrix} V_r^1 \\ V_r^2 \end{pmatrix} = \begin{pmatrix} S_{11} & S_{12} \\ S_{21} & S_{22} \end{pmatrix} \begin{pmatrix} V_f^1 \\ V_f^2 \end{pmatrix} \tag{3.11}$$

with V_r^i the reflected voltage and V_f^i the forward voltage on port i, and S_{ij} the S-matrix elements introduced in **equation 1.40**. We impose $V_f^1 = V_f^2$ in our simulations, such that:

$$|\Gamma_i| = \sum_{j \neq i} |S_{ii} + S_{ij}|, \quad \text{VSWR}_i = \frac{1 + |\Gamma_i|}{1 - |\Gamma_i|}$$
$$R_L^i = \frac{Z_0}{\text{VSWR}_i} \tag{3.12}$$

We present the simulation results, alongside with the scaling laws introduced in the previous section in **figure 3.15**. Since the utilized antenna model intends to represent either of the real

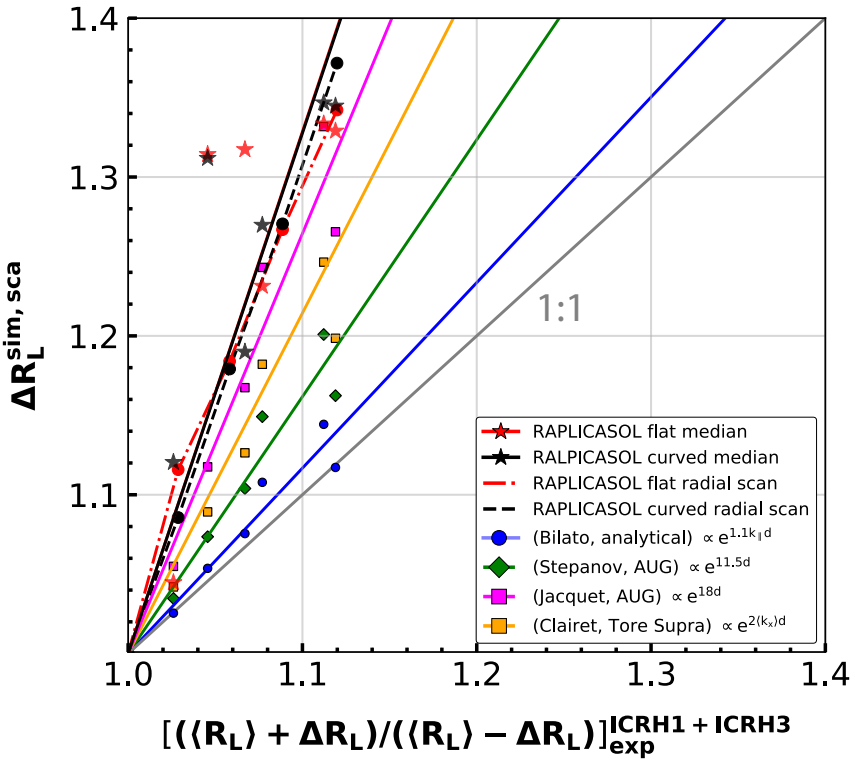

Figure 3.15: Change in loading resistance from RAPLICASOL (sim) and scaling laws (sca), $\Delta R_L^{\text{sim, sca}}$, vs. experimental median values of the ICRH1 and ICRH3 combined data set.

Approach	Linear estimator
Bilato's formula, $k_\parallel = 7.7\,\text{m}^{-1}$	1.168 ± 0.183
Stepanov's scaling (lower limit)	1.617 ± 0.255
Clairet's scaling, $\langle k_x \rangle \sim \lvert k_\parallel^{\text{FS}} \rvert = 7.45\,\text{m}^{-1}$	2.144 ± 0.343
Jacquet's scaling	2.644 ± 0.428
RAPLICASOL flat model simulations	3.286 ± 1.207
RAPLICASOL flat model radial scan	2.978 ± 0.282
RAPLICASOL curved model simulations	3.276 ± 1.021
RAPLICASOL curved model radial scan	3.080 ± 0.035

Table 3.3: Linear estimators for the different scalings and RAPLICASOL simulations. Results using OLS with a 99% confidence interval.

ASDEX Upgrade 2-strap antennas, the simulated loading resistance values for both feeders are averaged, and compared against the experimental median value corresponding to the combined data set of ICRH1 and ICRH3. The R-cutoff displacement as measured by Ref. X4 for a given experimental point is used to evaluate the scaling laws. Linear regressions are performed in order to better visualize differences between the multiple approaches, of which the linear estimators are listed in **table 3.3**. While the correct scaling behavior is reproduced with RAPLICASOL, i.e. the simulations of loading resistance change converge to 1, as $\Delta d_{\text{cutoff}} \rightarrow 0$, the predicted change exceeds that of experiments by a factor of ~ 3 for both the curved and flat models. The radial scans display a similar scaling to that obtained when using the full density profiles. We also find that the experimental scaling proposed by Jacquet for the ASDEX Upgrade 2-strap antennas in axisymmetric plasma radial scans is in excellent agreement with the 1D simulations. This observation further validates the RAPLICASOL results, and supports the conclusion obtained in the previous section.

3.2.7 Validity of R_L as an approximation to $Re(Z_{rad})$

In this section, we offer a description of the expected deviations incurred in approximating $R_L \sim \text{Re}(Z_{\text{rad}})$, as well as a discussion of the experimental absolute error of R_L also resulting from this assumption.

In assuming $R_L \propto e^{-\alpha d_{\text{cutoff}}}$, we are approximating R_L to have the same asymptotic behavior as $\text{Re}(Z_{\text{rad}})$. In principle, this would be true if $\text{Im}(Z_{\text{rad}})$ remains constant for all plasma conditions, but we will see this is in fact not the case. We first look at the radial scan in RAPLICASOL with the curved antenna model, and evaluate R_L, $\text{Re}(Z_{\text{rad}})$ and $\text{Im}(Z_{\text{rad}})$ for every plasma position. The result is presented in **figure 3.16**. As it would be expected from the evanescent nature of the fast wave at the edge, the further the plasma moves away from the antenna, the more $\text{Re}(Z_{\text{rad}})$ decreases and the more $\text{Im}(Z_{\text{rad}})$ increases. This behavior is associated with larger near fields and worse coupling conditions.

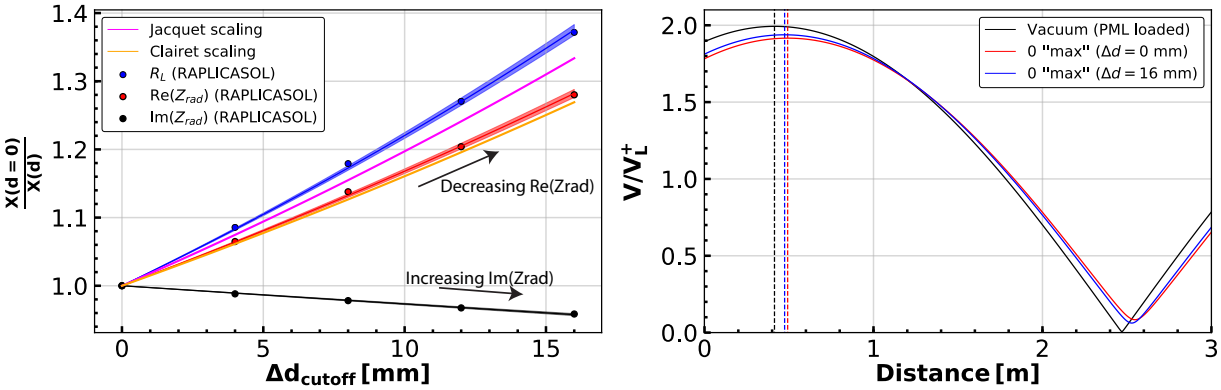

Figure 3.16: Left: RAPLICASOL radial scan simulations with the curved 2-strap antenna model. Evaluated are R_L, $\text{Re}(Z_{\text{rad}})$ and $\text{Im}(Z_{\text{rad}})$. The values at $\Delta d_{\text{cutoff}} = 0$ are divided by those at different shift positions. Right: Steady-state voltage distribution in the transmission line for various Γ_{input}.

Interestingly, the scaling of R_L and $\text{Re}(Z_{\text{rad}})$ remains exponential, but with different factors. We obtain from an OLS fit $\alpha(R_L) \sim 19.92 \pm 0.35\,\text{m}^{-1}$ and $\alpha(\text{Re}(Z_{\text{rad}})) \sim 15.53 \pm 0.29\,\text{m}^{-1}$. This validates the assumption previously made of $R_L \propto e^{-\alpha d_{\text{cutoff}}}$, but an important distinction arises. It was assumed up to now, that $\Delta R_L \sim \Delta\text{Re}(Z_{\text{rad}})$ and compared in this manner to different scalings. While experimental predictions such as the Jacquet scaling were made explicitly for

the loading resistance, analytical scalings such as the ones from Clairet or Bilato are made for $\mathrm{Re}(Z_{\mathrm{rad}})$ instead. When one now compares the RAPLICASOL results against these scalings, the agreement becomes even more satisfactory. R_L is well matched by Jacquet scaling, while $\mathrm{Re}(Z_{\mathrm{rad}})$ agrees very well with Clairet scaling[3]. This is of especial importance, since both experimental and theoretical literature tends to ignore this distinction.

This difference has implications for experimental measurements. In deriving the expression for the loading resistance in **equation 1.46** the imaginary part of Γ_L was ignored. When measuring the VSWR and R_L in experiments, changes in Z_{rad} translate to different distributions of the voltage in the transmission line according to **equation 1.43**, and thus, different positions at which V_{max} is found. In ASDEX Upgrade, the position of V_{max} is estimated in vacuum conditions and assumed static during a plasma discharge. If we set $V_L^+ = \text{const.}$, and use Γ_{L} from RAPLICASOL, we can plot $V(l)/V_L^+ = f(\Delta d_{\mathrm{cutoff}})$, as seen in **figure 3.16**. It is seen that during the radial scan the voltage distribution does not change significantly, but it does change non-negligibly with respect to the vacuum case. If we take the position of V_{max} in vacuum as the absolute position of the voltage probe, we can compute the percent error, δV_{max}, for each $\Delta d_{\mathrm{cutoff}}$, which turned to be: $\delta V^0_{\mathrm{max}} \sim 0.182\%$ and $\delta V^{16}_{\mathrm{max}} \sim 0.105\%$. Naturally, the farther the plasma is from the strap, the more the RF fields behave like in vacuum and the smaller the error becomes. This error can be translated to the loading resistance change, which behaves as $\Delta R_L = |V^{(1)}_{\mathrm{max}}|^2/|V^{(2)}_{\mathrm{max}}|^2$, and we find $\delta(\Delta R_L) \sim 0.15\%$. The small error arises from the wide voltage maximum at $\nu_{\mathrm{ICRF}} = 36.5\,\mathrm{MHz}$ and further validates the usage of such diagnostic.

3.2.8 1D empirical extrapolation to the ITER ICRF system

It has been shown in **table 3.2** that the experimentally-derived ODR exponents for the combined data sets of 2-strap and 3-strap antennas are very similar. This is despite the fact that the two types of ICRF antennas have different geometry, $k_{||}$ wavenumber spectra when operated in dipole phasing, and thus R-cutoff positions. We can take advantage of this fact to forecast the average coupling change of an ASDEX Upgrade-like ICRF antenna in an ITER-like plasma. This exercise is meant to provide an overview of the similarities and differences between both machines, and will highlight the main knowledge gaps that need to be bridged in the future.

We will use the same scaling function, f_{fit}, with the experimentally-derived radial decay parameter α. If each of the derived α from the combined 2-strap and 3-strap data sets is taken to be an independent realization, and assume α normally distributed, we can construct a 99% confidence interval based on the standard deviation of these realizations, which yields:

$$\begin{cases} \left\langle \Delta R_L^{\mathrm{MP}} \right\rangle \sim e^{-\left\langle \alpha^{\mathrm{MP}} \right\rangle \Delta d_{\mathrm{cutoff}}} \\ \left\langle \alpha^{\mathrm{MP}} \right\rangle = 7.31 \pm 1.01\ \mathrm{m}^{-1} \end{cases} \tag{3.13}$$

with $\left\langle \alpha^{\mathrm{MP}} \right\rangle$ the average of the ODR exponents for the combined data sets of 2-strap and 3-strap antennas. There are no, as of currently, predictions for the R-cutoff displacement in ITER, but they do exist for the separatrix. We will take these as a reference, but bearing in mind that the actual R-cutoff displacements may be smaller/bigger depending on SOL conditions. Different

[3] In [81], no distinction was made between R_L and $\mathrm{Re}(Z_{\mathrm{rad}})$, both being treated as the same quantity. We see from our results that the antenna near fields should not be ignored, and that theoretical predictions for $\mathrm{Re}(Z_{\mathrm{rad}})$ are not directly comparable to R_L.

models have been used to predict such midplane displacements. In [85] displacements ranging from ±2 cm to ±3.5 cm are discussed in base of the modeling approach taken (vacuum field-line tracing, ideal MHD modeling and resistive linear and non-linear modeling) and the kinetic profiles used, such as the electron pedestal temperature. This translates to our particular case in displacements ranging from $\Delta d_{\text{separatrix}} = 4-7$ cm from the minimum to the maximum separatrix radial position clearance at full coil-current (90 kAt). We will take these as our upper-estimation, since it is clear that reducing the coil currents, should ELM mitigation/suppression be achieved in such conditions, would produce the displacements to consequently decrease. The resulting coupling variation in % is shown in **figure 3.17**.

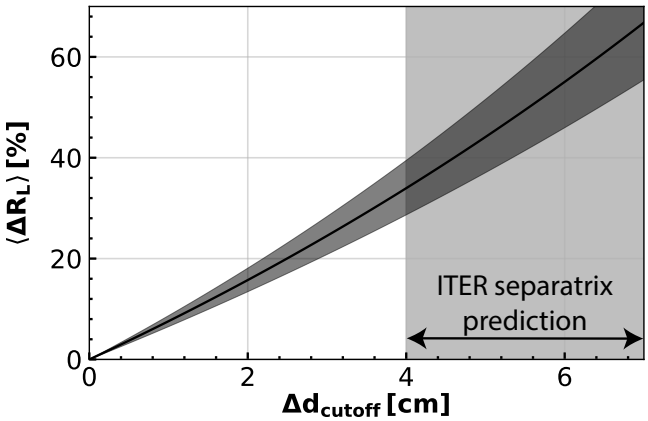

Figure 3.17: Average loading resistance change (%) as a function of the R-cutoff displacement. A prediction for the separatrix displacement from the minimum to the maximum plasma clearance is marked with a light-gray highlight.

The dependence on the excited $k_{\parallel}$ spectrum by the antenna enters this equation implicitly via Δd_{cutoff}. In ITER, we expect RF fields' spectra peaking at $k_{\parallel} \sim 2-6\,\text{m}^{-1}$, the minimum corresponding to $\{0,0,\pi,\pi\}$ phasing, the maximum to $\{0,\pi,0,\pi\}$ for $\{0,\pi\}$ poloidal phasing [86]. The latter is closer to the 2-strap antenna case in ASDEX Upgrade, and it is expected to have the largest coupling variation assuming a monotonically decreasing displacement profile from the separatrix to the wall. It is likely, however, that the most used configuration will lie in between $k_{\parallel} \sim 3-4\,\text{m}^{-1}$, as the $\{0,\pi,\pi,0\}$ phasing might help reduce ICRF-specific impurity production when the toroidal straps are properly balanced power-wise [87].

When extrapolating this scaling to the ITER ICRF antenna, there exist two main factors that can affect the prediction. First, it is expected from theory that the lower $k_{\parallel}$ becomes, the smaller α should be. In the discussed range of $k_{\parallel} \sim 2-6\,\text{m}^{-1} < 7.7-11\,\text{m}^{-1}$, the value for $\langle \alpha^{\text{MP}} \rangle$ here used will likely represent an overestimation. This lower $k_{\parallel}$ also has the benefit of producing smaller Δd_{cutoff}. On the other hand, in ASDEX Upgrade the vertical size relation between the plasma confined region and ICRF antenna is $\lambda_r^{\text{AUG}} \sim 1.6:1$, assuming an elongated radius ~ 0.8 m. In ITER this size relation becomes $\lambda_r^{\text{ITER}} \sim 7:2 \sim 2.2 \times \lambda_r^{\text{AUG}}$ [88]. Non-axisymmetric features that might be "integrated" by the ASDEX Upgrade antennas will appear as a more homogeneous perturbation in front of the ITER antenna, raising the expected value of $\langle \alpha^{\text{MP}} \rangle$ closer to the axisymmetric one. Seen from another perspective, we should expect that in ITER $\langle \Delta d_{\text{cutoff}} \rangle^{\text{eff}} \rightarrow \Delta d_{\text{cutoff}}$. Thus, the expectation of smaller loading changes than those predicted by **equations 3.13** due to the smaller $k_{\parallel}$ in ITER can be overturned by a larger effective displacement than that in ASDEX Upgrade.

Other uncertainty factors include the fact that this scaling has been constructed uniquely with $n = 2$ MP symmetry, and a plasma edge safety factor $q_{95} \sim 5.3$. Predictions for the ITER boundary displacement include $n = 3$ and $n = 4$ symmetric configurations, which will display a different perturbation poloidal mode number at the edge as a function of the ITER q-profile. Additionally, a finite k_{θ} due to poloidal strap phasing, antenna up-down asymmetry and cross-coupling will also play a role beyond what we can predict with the here employed model.

3.3 Conclusions

In this chapter, we have systematically explored for the first time the effect of rotating MPs on the ICRF fast wave coupling performance. In this manner, we have addressed two physics goals: the controlled study of the effect of 3D plasma geometry on the ICRF system (mimicking external MHD modes, and giving insight for stellarator configurations), and the actual effect of MPs on the ICRF system. The plasma confined region response to the MPs creates a field-aligned kink displacement which depends on the plasma conditions and the applied toroidal (here $n = 2$) and poloidal spectra, $\Delta\varphi_{\mathrm{UL}}$, in the MP current waveforms. The plasma displacements decay monotonically in the SOL, registered by the lithium beam and reflectometry diagnostics. However, the SOL can be noticeably affected by local sources and sinks, meaning that the SOL displacement dependence on $\Delta\varphi_{\mathrm{UL}}$ might not exactly correspond to that of the separatrix.
The loading resistance measured in each ICRF antenna feeder reacts accordingly to the SOL density modification, well diagnosed by embedded X-mode reflectometry in three different poloidal positions. Two overlapping effects participate in the loading resistance changes: the plasma pump-out effect, seen as an average increase of the loading resistance with respect to a reference discharge with no MPs, and the rotating kink displacement, seen as a coherent oscillation of the loading resistance locked to the MP rotation. For the studied cases in ASDEX Upgrade, the net effect is an increase of the overall loading resistance at the expense of time-variable coupling conditions. The maximum change in loading resistance is experienced approximately when the density profile is shifted closer/farther to the antenna center. For the first time, it is reported that the loading resistance changes do depend on the poloidal phasing of the MPs. A 1D scaling is derived that relates the change in the distance between the ICRF antenna and fast wave R-cutoff, as measured by several diagnostics, to the average change in loading resistance. This scaling is seen to predict smaller average loading resistance changes with $\Delta d_{\mathrm{cutoff}}$ than that of scalings previously reported in the literature. It is plausible that the underlying reason is the "integration" by the ICRF antenna over the whole 3D perturbed density profile, which would result in a milder loading resistance change than that produced by axisymmetric radial plasma movements.
ICRF simulations are performed with the 3D full-wave solver RAPLICASOL code. The input 1D density profiles have been reconstructed from the lithium beam diagnostic. The magnetic induction field is treated in 1D approximation, decaying with $1/R$. The predicted loading resistance changes exceed that of experiments by a factor of ~ 3 when using either the curved or flat ASDEX Upgrade 2-strap antenna models. In spite of this, the numerical simulations are in very good agreement with previous coupling studies evaluated in axisymmetric plasma conditions. Therefore, these results highlight the need to treat the problem in full 3D fashion, as reduction to 1D prevents predictive capabilities.
The experimentally-derived scaling exponent is utilized for a prediction of the change in loading resistance for the ITER ICRF antenna in MP active plasmas. This scaling predicts changes up to $\langle \Delta R_L \rangle \sim 65\%$ when the R-cutoff displacement can be identified with the maximum predicted separatrix displacement by different MHD simulations. However, this scaling allows only to give an estimation on the average array behavior, and not on the individual straps, for which the S-matrices need to be known. Furthermore, it is expected that the lower $k_{\parallel}$ value used in ITER and the relative size increase between the ITER plasma and ICRF antenna of $\lambda_r^{\mathrm{ITER}} \sim 2.2 \times \lambda_r^{\mathrm{AUG}}$ will affect this prediction. In order to diagnose the full effect of MPs on the ITER ICRF system, where a complex interplay exists among the 8 strap triplets, and the ratio between ICRF antenna size to the plasma perturbation characteristic wavelength in the midplane is different from AS-

DEX Upgrade, the problem needs to be addressed by considering a 3D magnetic field, density and antenna model altogether. Lastly, we would like to point out that coupling oscillations such as the ones presented in this study can have implications for antennas working close to their operational limits. If the plasma cutoff displacement becomes large enough to revert the benefit of the induced pump-out, the loading resistance can decrease below the level with no MPs for some rotation phases. This would lead to higher voltages in the antenna structure. This situation is, however, only sporadically seen for some feeders in ASDEX Upgrade.

Overall, the data here presented should help clarify the possible impact of plasma asymmetries on the total delivered RF power to the core plasma, help improve the matching and controller strategy, as well as shed some light on the implications on RF image current compensation on ICRF limiters.

Chapter 4

Numerical evaluation of 3D plasma response to MPs and ICRF Coupling

This chapter includes adapted material from:
G. Suárez López et al. *"Edge ICRF simulations in 3D geometry: From MHD equilibrium to coupling determination"* published in *AIP Conference Proceedings* **2254**, 050006 (2020) [89].
G. Suárez López et al. *"Validation of high-fidelity ICRF antenna coupling simulations in full 3D geometry against experiments in the ASDEX Upgrade tokamak"* published in *Plasma Phys. Control. Fusion* **62**, 125021 (2020) [90].

In this chapter, the numerical scheme used for the evaluation of the impact of MPs on ICRF coupling is presented. The problem has been addressed for the first time from first principles, including: the computation of the 3D plasma equilibrium by a non-linear MHD code, the 3D density profile reconstruction, and the 3D modeling of ICRF near fields with a realistic curved antenna geometry. An overview diagram of the used codes and their relevant output can be seen in **figure 4.1**. The 3D magnetic induction field inside the LCFS is obtained with the PARVMEC code (see **section 2.2.3**) using as input the CLISTE converged 2D solution, and then applying a 3D perturbation field. The magnetic induction field domain is extended to the SOL with the BMW code (**section 2.2.4**), which computes a linear superposition of the external conductors' vacuum field with the volume integral of the plasma currents. This induction field is then used as input for the EMC3-EIRENE code (**section 2.2.7**) to reconstruct the 3D density profile. Finally, both induction field and plasma density are inputs for the RAPLICASOL code (**section 2.2.8**), which computes the ICRF antenna S-matrices from a realistic CAD model of it in the cold plasma approximation.

4.1 Plasma response to MPs studied with the PARVMEC code

The PARVMEC code was utilized with two objectives: first, as a way of numerically studying the plasma response to the applied magnetic perturbation field, and second, to provide the calculation of the magnetic induction field for further simulations with the EMC3-EIRENE and RAPLICASOL codes. Since PARVMEC computes the resulting plasma equilibrium in the ideal MHD limit, the code input is composed of the following elements:

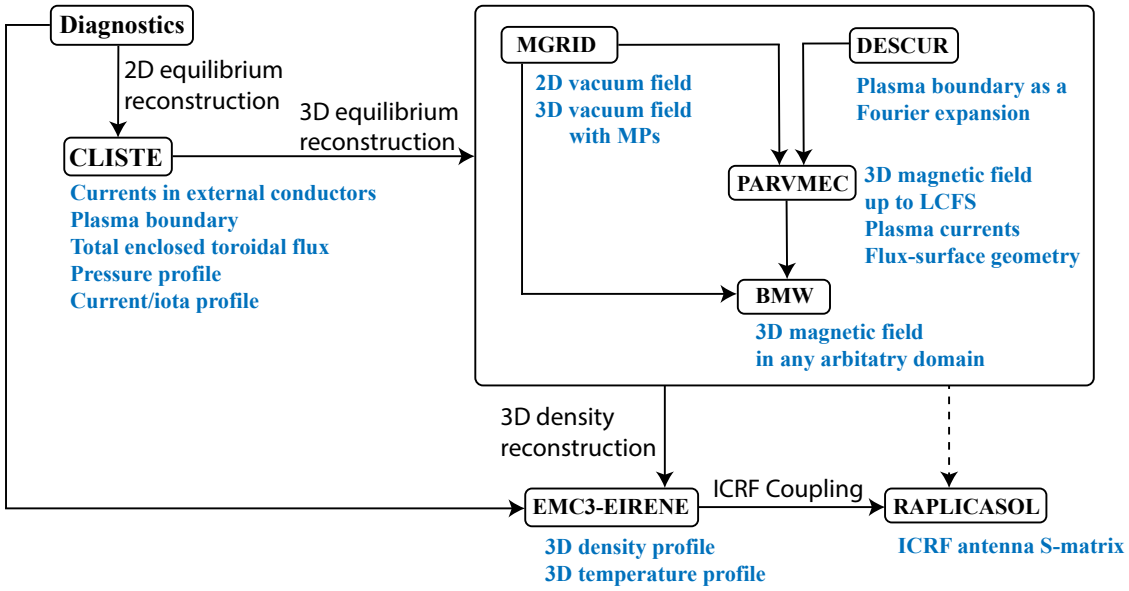

Figure 4.1: Numerical scheme used for the computation of ICRF coupling with 3D magnetic and density profiles.

1. The total enclosed toroidal flux.
2. A pressure profile as a function of the normalized toroidal flux.
3. The plasma toroidal current or iota profile as a function of the normalized toroidal flux.
4. A Fourier decomposition of the initial plasma boundary and magnetic axis.

These profiles can be nowadays self-consistently integrated into PARVMEC directly from diagnostic data via the V3FIT code, which has also been recently coupled to SIESTA for the reconstruction of 3D plasma equilibria with islands [91]. Nevertheless, it is also possible to extract these quantities from a converged 2D equilibrium by another code. We have chosen the latter, as the former would require major effort integrating the ASDEX Upgrade diagnostics into V3FIT.

4.1.1 Selection of modeled discharge

First, a representative discharge and time point are chosen, from which the experimental data can be used as input for the axisymmetric reconstruction of the CLISTE code. Then, CLISTE's output can be used as the input for PARVMEC, and 3D effects can be simulated by further imposing the field from the MP coils. The reference discharge #34632 at $t = 5$ s is chosen as the basis for equilibrium reconstruction. The motivation to use the reference discharge instead of one with MPs relies on the simplification of diagnostic handling to obtain a more accurate CLISTE result. On the other hand, we are explicitly neglecting the effects of MPs on the plasma pedestal, such as the increased transport during pump-out. These effects will not arise in PARVMEC, since no transport equations are solved, and would have to be included indirectly by using MP-affected profiles as input. As it will be discussed at the end of this section, neglecting these effects might have an impact on the resulting simulations as to how they compare to the experimental data. The output kinetic pressure and toroidal plasma current profiles from CLISTE for our chosen

time point have been plotted in **figure 4.2**. Notice, that the pressure profile contains no flattening close to rational flux surfaces. This choice of $p' \neq 0$ at rationals will result in divergent Pfirsch-Schlüter currents, as expected from ideal MHD theory, increasing the solution sensitivity on the used radial grid (see **section 4.1.2** for more details).

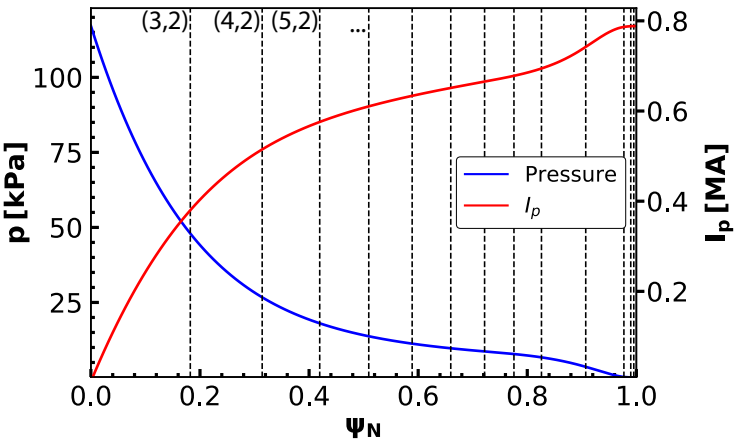

Figure 4.2: Input pressure and toroidal plasma current for the PARVMEC code as a function of the normalized toroidal flux. ASDEX Upgrade discharge #34632 at $t = 5.0\,\mathrm{s}$. Included as vertical dashed lines are the positions of rational flux surfaces with $m = 3, ..., 15$, $n = 2$ mode numbers.

We now sketch the general steps that have been followed in performing the PARVMEC simulations. First, the CLISTE plasma boundary is fed into the DESCUR code, which computes the Fourier harmonic representation of the LCFS. Since the separatrix contains a singular point (X-Point) that cannot be represented by a finite number of Fourier harmonics, the toroidal flux is truncated just inside it, close enough that the loss of plasma volume is as small as possible. We have utilized $\psi_{\mathrm{trunc}} \sim 0.999\,\psi^{\mathrm{sep}}_{\mathrm{CLISTE}} \sim -3.15\,\mathrm{Wb}$ for the truncation. Next, the vacuum induction field is computed with the MAKEGRID code, which uses a Biot-Savart representation of the external conductors (see **section 2.2.1**). Initially, we only compute the 2D induction field (no MPs), which will serve for the comparison between the CLISTE and PARVMEC free-boundary solutions in axisymmetry. Since CLISTE includes SOL currents, which are outside PARVMEC's computational domain, the first found solutions from the two codes will generally not coincide. In order to artificially include the effect of SOL currents in PARVMEC, and thus reduce the differences with respect to CLISTE, the following procedure is utilized: (i) The SOL currents are progressively decreased in the CLISTE solution, and the plasma boundary is newly evaluated each time. (ii) The small differences in plasma boundary arising between the full CLISTE solution and the *reduced SOL current* one are compensated by slightly changing the currents ($\sim 1.5\%$) in the LFS external conductors (i.e. V2, V3 in **figure 2.2**). The procedure is repeated until the currents in the SOL have been reduced to a value which generates very small differences between the axisymmetric CLISTE and PARVMEC solutions. In praxis, once the CLISTE solution has been fixed, further small adjustments are made to the PF coils taking the PARVMEC solution as a reference, as to improve the agreement even more. The final comparison of the plasma boundaries, inner flux surfaces and q-profiles for our discharge can be seen in **figure 4.3**. Here, we have used $m_\theta = 28$ poloidal harmonics, $n_s = 3001$ flux surfaces and a tolerance of the force residual of $f_{\mathrm{tol}} = 1 \times 10^{-15}$ for the PARVMEC simulation. The agreement between the two codes becomes excellent.

From this point on, an external 3D field from the MP coils is applied in the PARVMEC simulations, in order to evaluate the final 3D equilibrium. The MP coil currents from discharge #34622 are utilized as a reference. First, the PSL impact on the MP field poloidal spectrum and amplitude is evaluated for the applied sinusoidal waveform in experiments (with $\nu_0 = 3\,\mathrm{Hz}$ its main component) using the method previously introduced in **section 2.2.6**. This effectively reduces the MP coil currents from $I_{\mathrm{MP}} \sim 5\,\mathrm{kAt}$ to $I^{\mathrm{PSL}}_{\mathrm{MP}} \sim 3.2\,\mathrm{kAt}$. Next, we artificially shift the

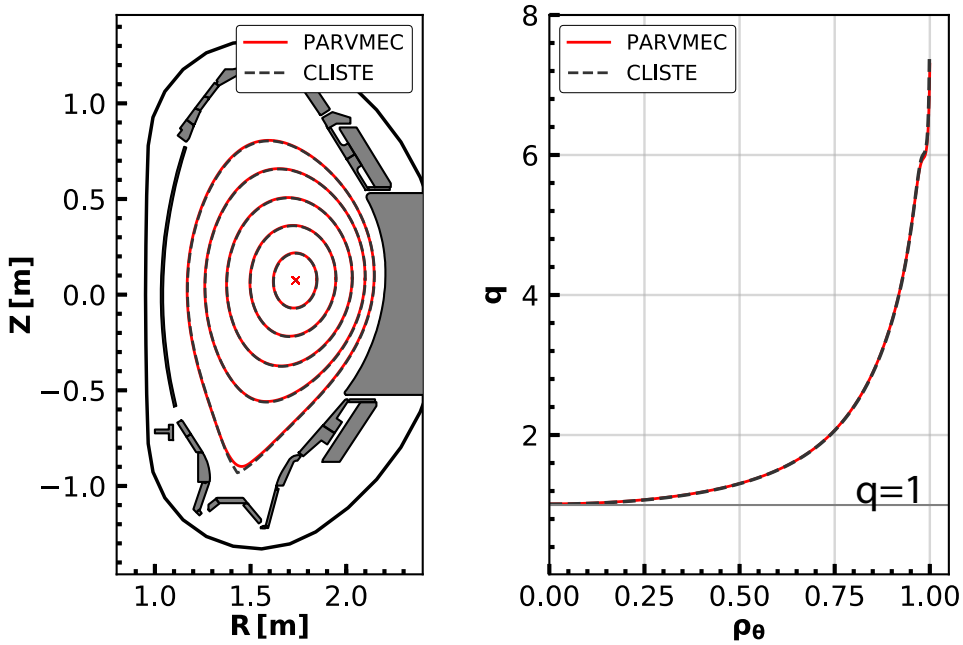

Figure 4.3: Comparison between the PARVMEC free-boundary and CLISTE axisymmetric solutions after modification of the SOL and PF coils currents. Left: Magnetic axis and some flux surfaces. Right: q-profile.

time base of the measured coil currents in the lower toroidal row, thus achieving 3D fields with different $\Delta\varphi_{\mathrm{UL}}$. In this manner, a scan over $\Delta\varphi_{\mathrm{UL}}$ can be numerically performed, and the plasma displacements evaluated. The plasma normal displacement, $\vec{\xi}_n$ is computed from the final 3D equilibrium. Since PARVMEC outputs the Fourier harmonics for the resulting flux surfaces (**equation 2.16**), we can define a normal displacement vector, $\vec{\xi}_n$:

$$\begin{cases} \vec{\xi}_n(n,\rho,\theta,\phi) = \|\vec{r}_{\mathrm{int}}(n,\rho,\theta,\phi) - \vec{r}_{n=0}(\rho,\theta)\|_{\mathcal{L}_2} \cdot \hat{\xi}_n(\rho,\theta) & (4.1) \\ \vec{r}_{n=0}(\rho,\theta) = (R_{n=0}(\rho,\theta), Z_{n=0}(\rho,\theta)) = \left(\sum_m R^m(\rho)e^{im\theta}, \sum_m Z^m(\rho)e^{im\theta}\right) & (4.2) \end{cases}$$

Where $\vec{r}_{\mathrm{int}}(n,\rho,\theta,\phi)$ is the intersection point between the 3D equilibrium reconstructed with a set of $\{0, \mathrm{n}\}$ toroidal harmonics, and the normal vector $\hat{\xi}_n(\rho,\theta)$ to the axisymmetric (n = 0) equilibrium; $\vec{r}_{n=0}(\rho,\theta)$ is the point on the axisymmetric equilibrium where the normal vector is started. In this way, $\vec{r}_{\mathrm{int}}(n=2,\rho,\theta,\phi)$ corresponds to the $n=2$ component of the plasma displacement $\vec{\xi}_n(n=2,\rho,\theta,\phi)$. The challenge arises in the correct determination of $\vec{r}_{\mathrm{int}}$. Since the normal vector to the axisymmetric equilibrium has no toroidal component, this allows reducing the problem to that of finding the intersection points between 2 two-dimensional curves in the $\{R,Z\}$ plane. The first curve is that defined by the cut of the 3D equilibrium in a given poloidal (ϕ = const.) plane. The second curve is constructed by a set of points on the normal to the axisymmetric plasma equilibrium at each angle θ. Since curve-2 is normal to the axisymmetric equilibrium, and intersects curve-1, it should yield $\vec{r}_{\mathrm{int}}$. Numerically, this is implemented in a simple manner. Each "differential" segment within a curve can be parametrized by an equation $\vec{l} = \vec{l}_0 + \vec{l}_t d$, where $\vec{l}_0$ is the starting point of the segment, $\vec{l}_t$ is a tangent vector lying along the segment, and d is the distance along the segment. The problem of finding the intersection point between a segment $\vec{p}$ in curve-1 and $\vec{q}$ in curve-2 is then formulated as:

$$\begin{cases} \vec{p} = \vec{p}_0 + (\vec{p}_1 - \vec{p}_0)d_p & (4.3) \\ \vec{q} = \vec{q}_0 + (\vec{q}_1 - \vec{q}_0)d_q & (4.4) \end{cases}$$

with $\vec{p} = \vec{q}$ at intersection. This system of linear equations is solvable in matrix notation:

$$\begin{pmatrix} r_{p_1} - r_{p_0} & r_{q_0} - r_{q_1} \\ z_{p_1} - z_{p_0} & z_{p_0} - z_{p_1} \end{pmatrix} \begin{pmatrix} d_p \\ d_q \end{pmatrix} = \begin{pmatrix} r_{q_0} - r_{p_0} \\ z_{q_0} - z_{p_0} \end{pmatrix} \quad (4.5)$$

Where $\{r_i, z_i\}$ represent cylindrical coordinates for the points p_0, p_1, q_0, q_1. A solution to this system can be obtained if the segments are linearly independent. If so, the intersection point always exists. However, we are only interested in those points which intersect within both segments simultaneously, therefore, $0 < d_p < 1$ and $0 < d_q < 1$. This simple method yields convergent accuracy provided enough points are taken in poloidal and toroidal directions, and has been used for all the displacements numerically evaluated in this chapter.

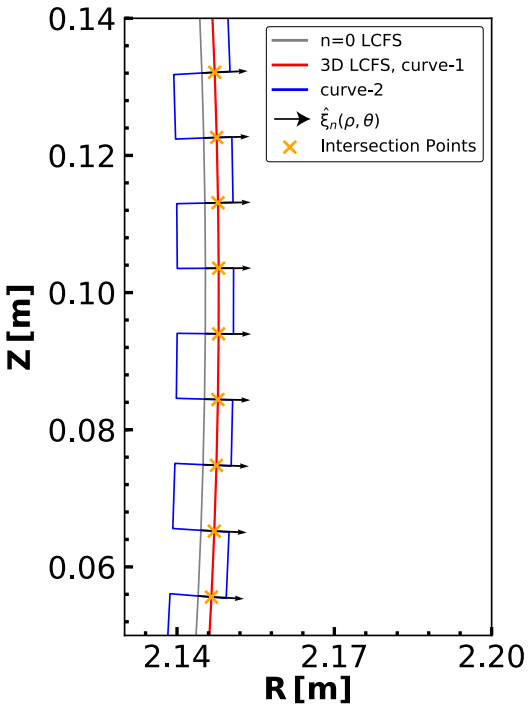

Figure 4.4: Method for the calculation of intersection points.

4.1.2 Scan over PARVMEC numerical parameters

A resolution scan was performed in PARVMEC to seek the optimum computational parameters. Especially, PARVMEC allows the user to set for a given run the maximum number of poloidal (m_θ) and toroidal (n_ϕ) mode numbers, the number of flux surfaces (n_s, i.e., the number of radial grid points) and the tolerance of the force residual (f_{tol}) to achieve. Furthermore, the vacuum field resolution (in a cylindrical grid, $\{n_r, n_z, n_\phi\}$, i.e., number of radial, vertical and toroidal points) can be investigated. It is also possible to optimize other computational parameters, such as the number of calls to the NESTOR solver (**equation 2.29**), but these mostly influence the numerical convergence and are of less physical relevance to the result. The 3D run with $\Delta\varphi_{\text{UL}} \sim 0°$ was chosen for the forthcoming scans, as it experimentally presents large enough LCFS displacements to more easily appreciate the effect of scanning a given parameter.

Spectral resolution: In order to resolve the basic helical geometry of the plasma boundary with $q_{\text{LCFS}} \sim 7.5$ and an $n = 2$ MP toroidal field symmetry, we need at least $m_\theta = 15$ poloidal mode numbers. Higher-order toroidal harmonics would consequentially require a larger number of poloidal harmonics in order to be represented at q_{LCFS}. Since the number of MP coils is finite, the perturbation field does indeed contain such harmonics. In first approximation, the coils can be modeled as a square function in toroidal direction, which discrete Fourier series contains odd harmonics, $n = 1, 3, 5..$ (the equivalent continuous transform is $\text{sinc}(\pi\phi)$). In praxis, however, the number of m_θ that can be used is limited due to the memory required to compute their Fourier coefficients. Two resolutions of $n_\phi = 4$ ($n = -8, -6, ..., 6, 8$ due to the used 2-fold toroidal symmetry) and $n_\phi = 8$ ($n = -16, -14, ..., 14, 16$) were utilized in PARVMEC to study the influence of these high-order toroidal harmonics on the resulting equilibrium. The number of m_θ was scanned, while n_s, f_{tol}, and the vacuum field resolution were kept constant.

We used two numerical diagnostics to evaluate the quality of the equilibrium convergence: the full plasma displacements and $n = 2$ component at the outboard midplane, the plasma top, the inner midplane and the "X-Point", as well as the q-profile at the LCFS. In ideal MHD, the q-profile is a topological invariant [36], and therefore, equilibria with an initial q-profile can only be converted through energy minimization into equilibria with the same q-profile. Would the q-profile not coincide, it would indicate that the used resolution is insufficient. The result of the comparison can be seen in **figure 4.5**.

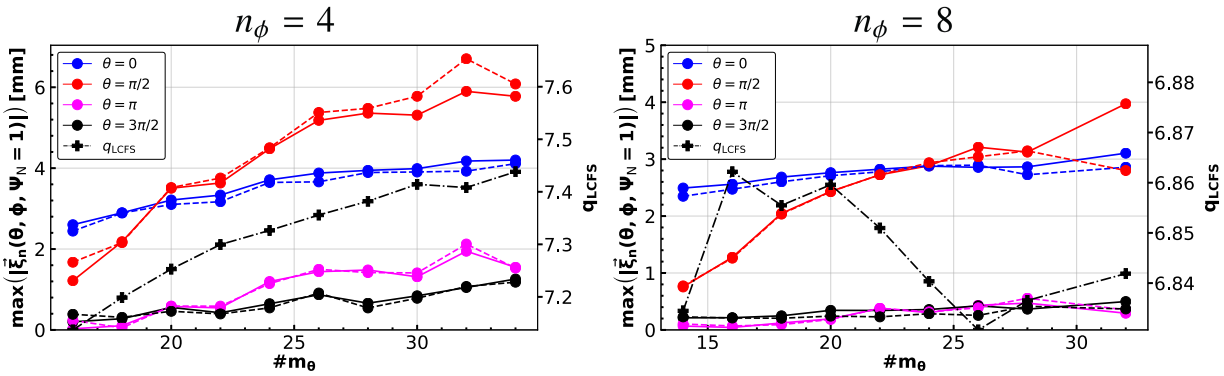

Figure 4.5: Plasma maximum displacements (full value in solid color and $n = 2$ component in dashed color) at the OMP (blue), top (red), inner midplane (magenta) and X-Point (black), and q_{LCFS} in black crosses, as a function of poloidal mode number m_θ. The number of radial grid point, n_s, the tolerance of the force residual, f_{tol} and the vacuum field resolution were kept constant. Left: $n_\phi = 4$. Right: $n_\phi = 8$.

Both cases were converged with $n_s = 1001$ flux surfaces; the equilibria with $n_\phi = 4$ was converged down to $f_{\mathrm{tol}} = 5 \times 10^{-14}$, while $n_\phi = 8$ down to $f_{\mathrm{tol}} = 5 \times 10^{-11}$ (smaller tolerance was often not possible to achieve for this case). Both cases display increasing (and convergent) displacements at all locations as the number of used m_θ increases. However, two different behaviors are observed for q_{LCFS}. In the $n_\phi = 8$ case, $q_{\mathrm{LCFS}} \sim 6.85 < q_{\mathrm{LCFS}}^{\mathrm{CLISTE}} \sim 7.5\,\forall m_\theta$, while for $n_\phi = 4$, $q_{\mathrm{LCFS}} \to q_{\mathrm{LCFS}}^{\mathrm{CLISTE}}$ as m_θ becomes larger. This indicates that the $n_\phi = 8$ resolution is not numerically stable, as the q-profile is not preserved in the energy minimization, and the increasing poloidal resolution does not solve the problem. We should keep in mind, that at this resolution the pitch-aligned higher toroidal mode numbers are only well represented at the most inner flux surfaces, i.e., $q = 2$, $n = 16$, $m = 32$, while the contribution to the outer ones is mostly non-resonant. More information can be obtained after inspection of the edge flux surfaces, which display a clear magnitude increase in the high-order toroidal harmonic amplitudes for this case, displayed in **figure 4.6**. In the $n_\phi = 4$ case, increasing m_θ leads to a better-resolved equilibrium, while the contribution of higher-order toroidal mode numbers remains small. In the $n_\phi = 8$ case, however, an oscillation of the plasma boundary becomes apparent at the LCFS. Increasing further $m_\theta > 32$ only increases the deviation from the expected $n = 2$ behavior. A similar observation has already been made in the literature. In [92], VMEC[1] was used to study $n = 3$ perturbed DIII-D equilibria. The EFIT axisymmetric code provided the necessary input in the same fashion as CLISTE is used in our studies. The pressure and the q-profile were held fixed, while the current density and LCFS were allowed to evolve. This method rules out the possibility of checking the q-profile as a diagnostic tool for convergence, since it is imposed fixed. It was found that when the EFIT equilibrium was truncated close to a rational flux surface, the 3D equilibria constructed from it would display poor convergence with respect to f_{tol}

[1]The serial version of the code. The parallel version was still under development.

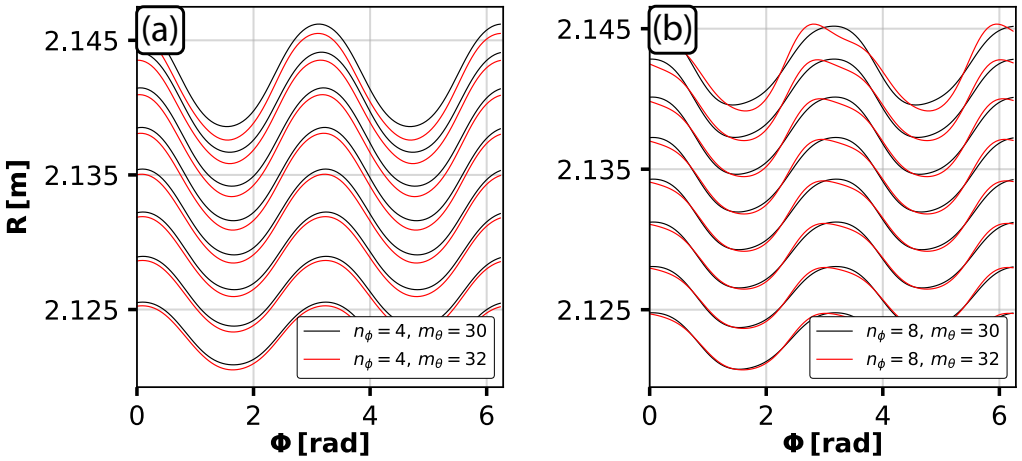

Figure 4.6: Comparison of some flux surfaces at the OMP between $\psi_N \in [0.9, 1.0]$ for (a): $n_\phi = 4$ and (b) $n_\phi = 8$.

and similar boundary oscillations of the flux-surface averaged toroidal current density at the LCFS. The suggested explanation is the ideal MHD instability of equilibria with near-separatrix rational flux surfaces. The proposed solution was to truncate the equilibria far enough inside the separatrix of EFIT, such that a large enough gap between main n-number rational flux surfaces and the boundary exists, but not deep enough that a significant fraction of the bootstrap current would be neglected. This method, however, presents several problems: (i) Rational numbers are dense in real space, thus deeming the term "gap between rationals" subjective. One can naturally find a gap between the set of rational numbers constructed on a limited number of toroidal harmonics, but the upper limit to this number remains then completely arbitrary. (ii) This truncation often requires removing a significant fraction of the q-profile, since close to the separatrix rational flux surfaces become densely packed. For instance, in the aforementioned publication $q_{\text{trunc}} \sim 5$ as opposed to the EFIT value close to the LCFS of $q^{\text{EFIT}}_{\text{LCFS}} \sim 7.5$. The resulting equilibria can therefore not represent correctly the poloidal structure of the edge displacements (i.e., with $q_{\text{trunc}} \sim 5$ and $n = 3$ implies $m_{\text{trunc}} \sim 15$), while the real poloidal mode number would be closer to the original EFIT edge value of $q^{\text{EFIT}}_{\text{LCFS}} \sim 7.5 \rightarrow m^{\text{EFIT}}_{\text{LCFS}} \sim 22$, if we assume the kink displacement to be pitch-aligned with the LCFS. Since our aim is to correctly reconstruct the poloidal and toroidal mode structure in order to accurately describe the density perturbation in the LFS, this method could make our calculations less experimentally relevant.
The chosen approach in our case was to keep as much as possible of the toroidal flux by avoiding truncation deep inside the separatrix of CLISTE. This means limiting the number of used toroidal harmonics to $n_\phi = 4$, which results in a numerically stable and convergent result. Furthermore, this resolution is enough to resolve the two main discrete harmonics of the MP coils in "square approximation", i.e. $n = 1, 3$ ($n = 2, 6$ for two field periods).

Number of flux surfaces (PARVMEC radial grid): In non-axisymmetric ideal MHD equilibria with smooth pressure and iota profiles, it is expected that divergent, helically-localized, Pfirsch-Schlüter and δ currents should develop at rational flux surfaces in order to preserve nestedness [46, 72, 93, 94]. Charge conservation imposes $\vec{\nabla} \cdot \vec{j} = 0 \rightarrow \vec{\nabla}\vec{j}_{||} + \vec{\nabla}\vec{j}_{\perp} = 0$. Since $\vec{\nabla}\vec{j}_{\perp} = 0$ is not always true, a parallel current density is required for this condition to be met. An expression for $|\vec{j}_{||}|$ can be derived by dotting the contravariant components of the current density from **equation 2.20** with the covariant ones of the induction field. In magnetic coordinates $\{\psi, \theta^*, \phi\}$:

$$\vec{B} = B_\psi \vec{R}^\psi + B_\theta \vec{R}^{\theta^*} + B_\phi \vec{R}^\phi \tag{4.6}$$

$$\vec{j}\cdot\vec{B} = |\vec{j}_\parallel||B| = \frac{1}{\mu_0}\left[(\vec{R}^\phi \times \vec{R}^\psi)\partial_\phi \tilde{B}_\psi - (\vec{R}^\psi \times \vec{R}^{\theta^*})\partial_{\theta^*}\tilde{B}_\psi\right]\cdot\left[B_\psi \vec{R}^\psi + B_\theta \vec{R}^{\theta^*} + B_\phi \vec{R}^\phi\right]$$
$$= \frac{1}{\mu_0\sqrt{g}}\left[B_\theta \partial_\phi \tilde{B}_\psi - B_\phi \partial_{\theta^*}\tilde{B}_\psi\right] = \frac{|B|^2}{\mu_0(B_\phi + \iota B_\theta)}\left[B_\theta \partial_\phi \tilde{B}_\psi - B_\phi \partial_{\theta^*}\tilde{B}_\psi\right] \tag{4.7}$$

with ι the rotational transform, the Jacobian obeys $1/\sqrt{g} = |B|^2/(B_\phi + \iota B_\theta)$ and $\tilde{B}_\psi = B_\psi - \phi\partial_\psi B_\phi - \theta^*\partial_\psi B_\theta$. A magnetic differential equation for $\tilde{B}_\psi$ can also be obtained from the ideal MHD force balance, **equation 2.24**, which reads:

$$\sqrt{g}(\vec{B}\cdot\vec{\nabla})\tilde{B}_\psi = \sqrt{g}\mu_0 p' \rightarrow \partial_\phi \tilde{B}_\psi + \iota\partial_{\theta^*}\tilde{B}_\psi = \mu_0 p' \frac{(B_\phi + \iota B_\theta)}{|B|^2} \tag{4.8}$$

This differential equation can be solved by Fourier expanding $1/|B|^2$, i.e.:

$$\frac{1}{|B|^2} = \frac{1}{B_0^2}\left(1 + \sum_{mn}{}' \delta_{mn} e^{i(n\phi - m\theta^*)}\right) \tag{4.9}$$

$$\tilde{B}_\psi = f(\psi)(\iota\phi - \theta^*) + \mu_0 p' \frac{(B_\phi + \iota B_\theta)}{B_0^2}\left[\phi + \sum_{mn}{}' \frac{1}{i(n - \iota m)}\delta_{mn} e^{i(n\phi - m\theta^*)}\right] \tag{4.10}$$

where the first term on the rhs. represents the homogeneous solution, with $f(\psi)$ an arbitrary radial function, and the second term the inhomogeneous one. By plugging **equation 4.10** into **4.7**, we obtain an expression for the parallel current density [95]:

$$\mu_0 j_\parallel = f(\psi)|B| + \mu_0 p' \frac{|B|}{B_0^2}\left(B_\theta + \sum_{mn}{}' \frac{nB_\theta + mB_\phi}{n - \iota m}\delta_{mn} e^{i(n\phi - m\theta^*)}\right) \tag{4.11}$$

The first term on the rhs. corresponds to the force-free δ current aforementioned. The second one, is the Pfirsch-Schlüter current. This last current is proportional to the pressure gradient, and can be seen to become singular at $\iota = n/m$ rational surfaces. In order to provide appropriate ideal MHD force balance, these currents need to be numerically resolved, otherwise the final equilibrium will fail to shield resonant external perturbations. The development of these currents in PARVMEC has been studied in detail in a simplified screw pinch geometry [96], and recently, in general toroidal geometry [97], leading to the conclusion that these are asymptotically resolved as resolution increases (in this case, the number of radial grid points). A scan over the number of radial grid points was performed with the case

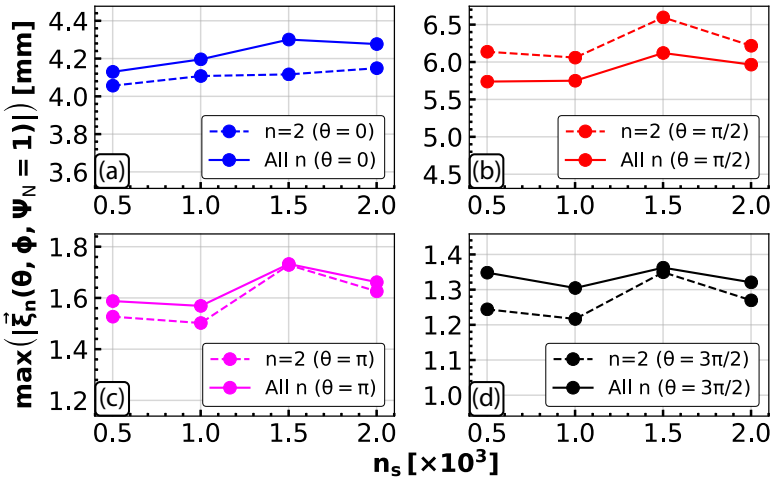

Figure 4.7: Plasma displacements at (a) OMP, (b) top, (c) HFS midplane and (d) near X-Point as a function of n_s.

$n_\phi = 4$, $m_\theta = 34$ for $n_s = 501, 1001, 1501, 2001$. All simulations were converged down to $f_{\text{tol}} = 5 \times 10^{-14}$. The displacements at the OMP, plasma top, HFS midplane and near the X-Point are shown in **figure 4.7**. We see that the change in plasma displacements is nearly independent of the number of flux surfaces, provided enough are used, i.e. $n_s \gtrapprox 501$. It will be shown in **section 4.2**, however, that even high radial grid densities of the order of $n_s = 1251$ are not enough to provide enough resolution as to completely shield resonant external perturbations.

Tolerance of the force residual: This scan intends to estimate a reasonable convergence criterion in terms of the force residual described in **equation 2.26**. The main limiting factor to minimize this residual is the wall-clock time of the cluster (i.e., the maximum time a simulation is allowed to run), and the gradient of the plasma thermal energy minimization, which generally, decreases considerably the smaller the force residual becomes. The case with $n_\phi = 4$, $m_\theta = 34$, $n_s = 1001$ was converged down to $f_{\text{tol}} = 1 \times 10^{-10}, 1 \times 10^{-12}, 5 \times 10^{-14}, 1 \times 10^{-16}$. The full and $n = 2$ component of the plasma displacement at the OMP, plasma top, inner midplane and X-Point were used as a diagnostic tool for convergence, and the result is displayed in **figure 4.8**.

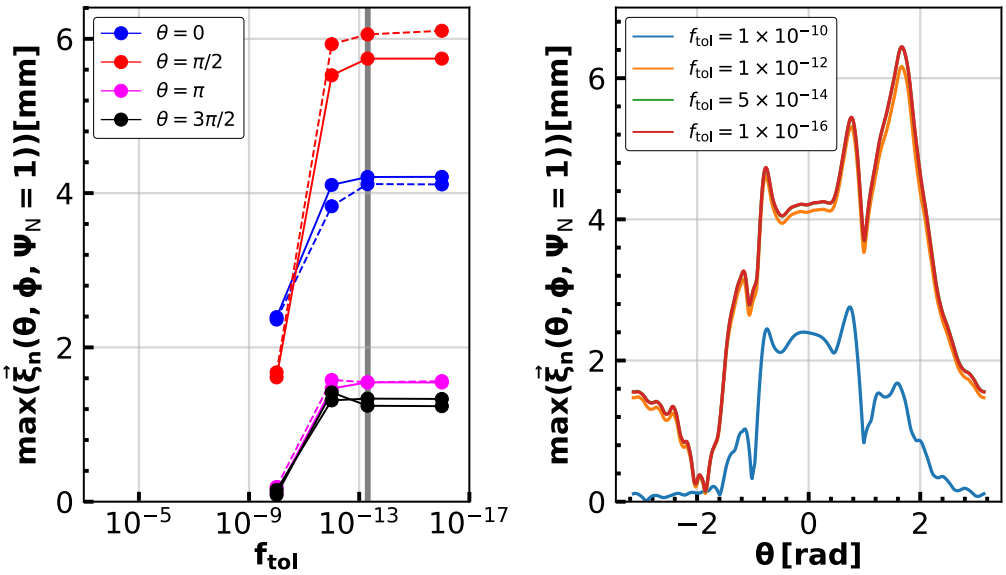

Figure 4.8: Left: Maximum full (solid) and $n = 2$ (dashed) component of the plasma displacement at the OMP, plasma top, inner midplane and X-Point as a function of f_{tol}. Right: Maximum full displacement at LCFS as a function of the geometric poloidal angle θ.

The case with $f_{\text{tol}} = 5 \times 10^{-14}$ is practically indistinguishable from the one with $f_{\text{tol}} = 1 \times 10^{-16}$. Therefore, the former limit has been used in the forthcoming simulations. Another interesting result is the spatial distribution of the force residual, which can be locally computed following **equation 2.24**. This is displayed in **figure 4.9**, where the local force residual has been normalized to the local pressure gradient. It is seen that, even though the innermost flux surfaces tend to relax asymptotically the smaller f_{tol} becomes ($f_{\text{tol}}^{\text{local}} \sim 10^{-8} \vec{\nabla} p$), the outermost ones do not ($f_{\text{tol}}^{\text{local}} \sim 10^{-3} - 10^{0} \times \vec{\nabla} p \ \forall f_{\text{tol}}$). This is clear from a numerical and physical perspective. It is in this region where most rational flux surfaces exist in the smallest volume, and therefore, where most numerical accuracy is required in the radial grid. In turn, this also means that for a given accuracy in the radial grid, number of Fourier harmonics and poloidal/toroidal points, further minimization of f_{tol} will not significantly improve the solution at the edge, where more

numerical accuracy may be required instead.

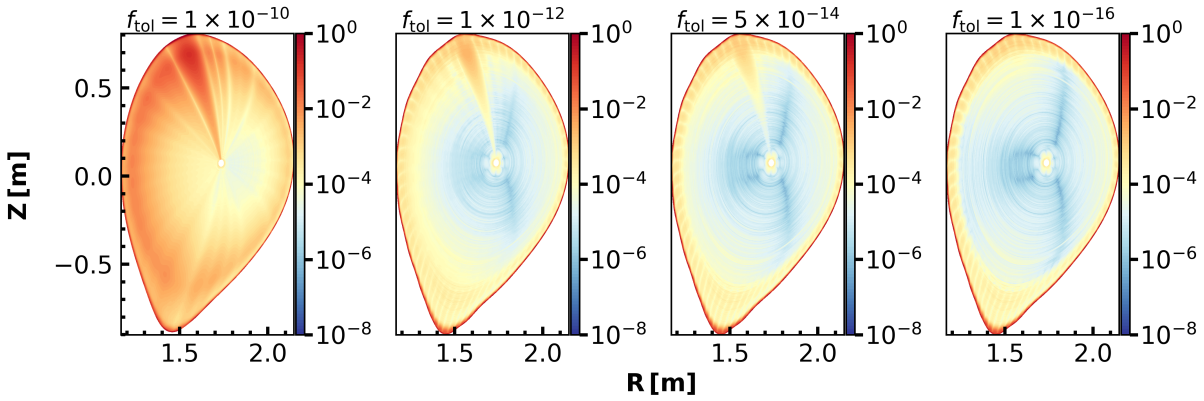

Figure 4.9: Locally computed $\left(\vec{j} \times \vec{B} - \vec{\nabla} p\right) / \vec{\nabla} p$ for different f_{tol} values.

4.1.3 Comparison to measured experimental displacements

The parameter scan detailed in the last section was used to decide what were the best numerical parameters we could use, given the limitations imposed both by physics and numerics. In general, good convergence was found when the number of flux surfaces was greater than $n_s \gtrsim 501$, the number of poloidal mode numbers was greater than $m_\theta \gtrsim 30$, the tolerance of the force residual was smaller than $f_{\text{tol}} \lesssim 5 \times 10^{-14}$, and the number of toroidal mode numbers was kept not larger than $n_\phi = 4$. In fact, further increasing n_s and m_θ does make the solution better converged (displacement and q-profile wise), but how much these parameters can be increased is limited by the available memory and wall-clock time in a given cluster.

Given these circumstances, a solution which involves a compromise in accuracy was chosen, i.e. $n_s = 1251$, $m_\theta = 32$, $n_\phi = 4$ and $f_{\text{tol}} = 5 \times 10^{-14}$. The cylindrical grid was kept at $\{n_r = 256, n_z = 512, n_\phi = 64\}$ with 2 field periods. A scan over the MP field poloidal spectrum, $\Delta\varphi_{\text{UL}}$, is made with this accuracy and the PSL-attenuated coil currents, $I_{\text{MP}}^{\text{PSL}} \sim 3.2\,\text{kAt}$. We compared the $\nu = 3\,\text{Hz}$ fundamental amplitude of the OLS fit to the separatrix displacement measurements presented in **figure 3.6** with the $n = 2$ OMP component of the PARVMEC simulations. The result of such comparison can be seen in **figure 4.10**. It is apparent that the numerically computed displacements (blue curve in panel **(a)**) fall quite short from the experimental ones. Several factors may contribute to this disagreement, mainly:

1. Uncertainties in the pressure and current profiles of the underlying CLISTE equilibrium, for instance, related to core ICRF fast ions.

2. Lack of pump-out in the pedestal profiles. The CLISTE solution belongs to discharge #34632, the one with no MPs. Therefore, no pump-out effect is present in the kinetic profiles. Since PARVMEC preserves flux-surface quantities, this effect is not reproducible within the simulation when the MP field is imposed, and needs to be included at the input profile level.

3. Insufficient numerical accuracy in the PARVMEC solution. As stated previously, increasing further m_θ does increase the $n = 2$ component of the OMP displacement non-negligibly.

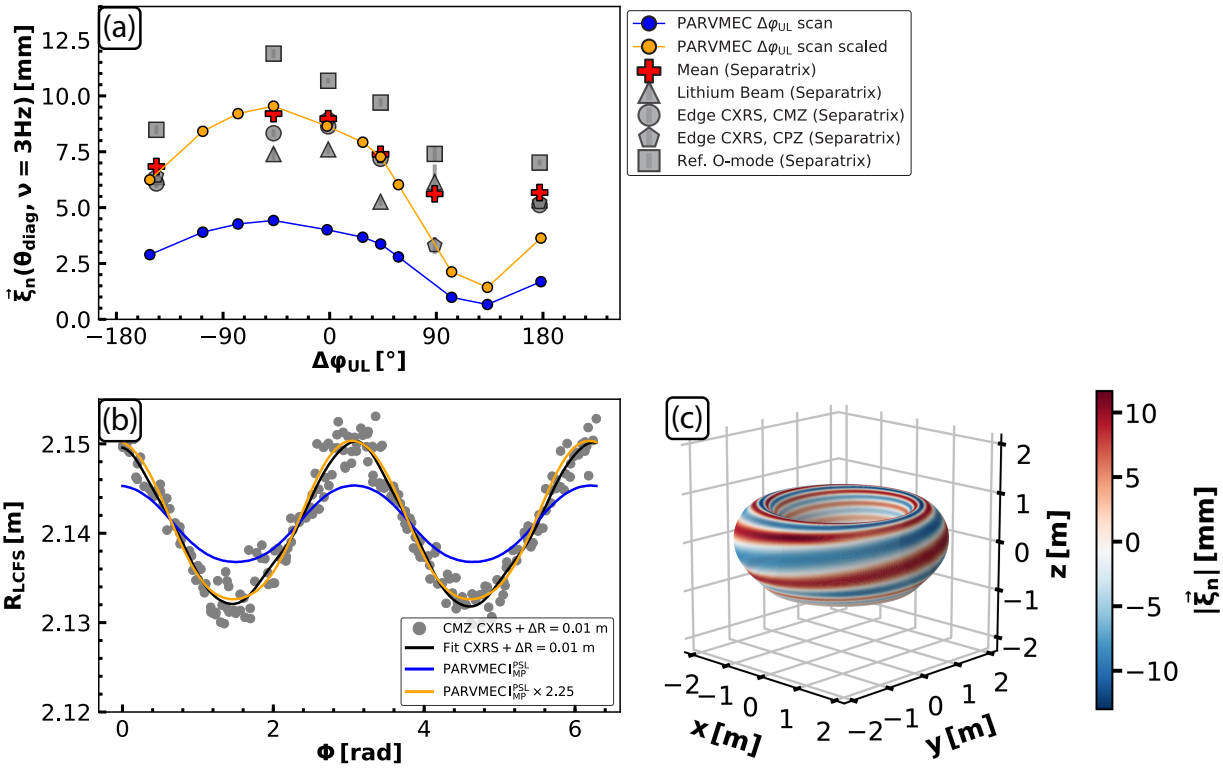

Figure 4.10: (a) Separatrix displacements registered by lithium beam, CXRS and O-mode reflectometer diagnostics, as a function of $\Delta\varphi_{\mathrm{UL}}$. The mean displacements are added as red crosses. The $n = 2$ OMP PARVMEC LCFS displacement is included as solid lines for the nominal (blue) and scaled (orange) currents in the MP coils. (b) CXRS separatrix position for several MP periods of discharge #34622 and PARVMEC LCFS for nominal and scaled MP coil currents. (c) PARVMEC distribution of plasma displacements at the LCFS for the scaled equilibrium currents, $\Delta\varphi_{\mathrm{UL}} = -2.2°$ case.

4. Uncertainties in the PSL model. The FE calculations in [55] are computed for a single coil-plasma distance, making them a first-order approximation.

5. Ideal MHD approximation. If the real magnetic equilibrium contains islands which width is determined by resistive MHD physics, this cannot be captured with the used model.

For these reasons, a scaling factor is used for the currents of the MP coils. The mean of the experimental displacements is computed for each $\Delta\varphi_{\mathrm{UL}}$. The $\Delta\varphi_{\mathrm{UL}} = -2.2°$ is used to derive the factor, such that:

$$f_{\mathrm{MP}} = \frac{\left\langle \xi_n^{\mathrm{exp}}(\nu = 3) \right\rangle}{\xi_n^{\mathrm{PARVMEC}}(n = 2)} \sim 2.25 \tag{4.12}$$

With $\left\langle \xi_n^{\mathrm{exp}}(\nu = 3) \right\rangle \sim 8.98\,\mathrm{mm}$, $\xi_n^{\mathrm{PARVMEC}}(n = 2) \sim 4\,\mathrm{mm}$. Each MP coil current is scaled by this factor yielding good agreement between PARVMEC and the experimental measurements for all the discharges. We also compare in **figure 4.10(b)** the CXRS separatrix position overlaid for several MP periods and the PARVMEC LCFS for the nominal and scaled currents. The latter is found to be in very close agreement with the measurements, aside from a relative radial shift of $\Delta R \sim 1\,\mathrm{cm}$. An OLS fit to the LCFS position reveals that the $n = 2$ component phase shift between the PARVMEC scaled equilibrium and the CXRS time traces is of the order of

$\Delta\phi \sim 0.6°$ (~ 0.01rad). In principle, this negligible phase shift would reinforce the validity of the used PSL model, discarding reason 4 as a main source of error.

4.2 Full-domain magnetic induction field computed with the BMW code

In this section, we detail the main topological characteristics of the magnetic induction field chosen for the forthcoming steps in our simulation workflow. The scaled-currents, $\Delta\varphi_{\mathrm{UL}} = -2.2°$ PARVMEC simulation previously described was extended with the BMW method to obtain the full-domain induction field including the SOL. The cylindrical grid where the magnetic vector potential is computed was kept at the same resolution used for PARVMEC, i.e. $\{n_r = 256, n_z = 512, n_\phi = 64\}$ with 2 field periods.

The connection length[2] at the OMP was compared against chosen PARVMEC flux surfaces as seen in **figure 4.11**. The agreement is impoverished at the very edge, where islands form densely due to the elevated shear. This is due to the expected divergent Pfirsch-Schlüter currents at rational flux surfaces with $p' \neq 0$ and the stringent numerical requirements that this situation poses to the PARVMEC solution. However, if we compare a non-rational flux surface, here chosen at $\rho_\theta = 0.87$, both this surface and the high-connection length region ($L_c = 1330\,\mathrm{m}$) overlap satisfactorily. This proves the reliability of the method to preserve the magnetic topology from PARVMEC where no rational flux surfaces exist, while in the domains where they do exist, it is generally not possible. As an example, we compare the contour line for $L_c = 100\,\mathrm{m}$ with the PARVMEC LCFS, which quickly exposes that these boundaries are topologically different. This effect can be further verified with a Poincaré plot of the BMW magnetic induction field mapped to the $\{\rho_\theta, \theta\}$ plane. Field lines were followed with the GOURDON code. The poloidal flux is computed in axisymmetric approximation from the BMW toroidal component of the magnetic vector potential:

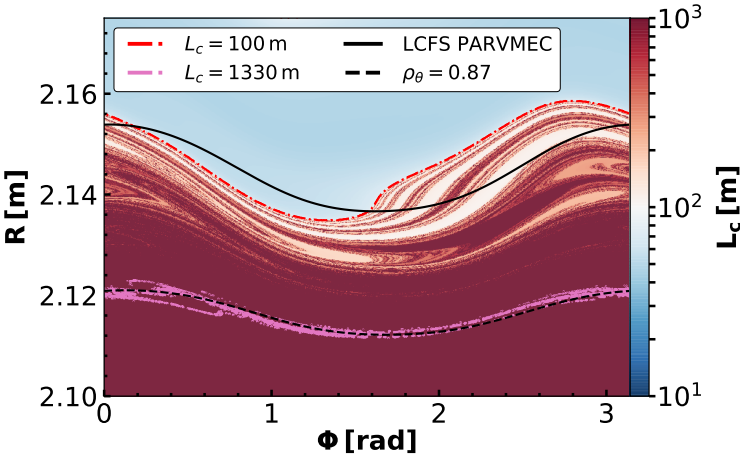

Figure 4.11: BMW connection length, L_c, at the OMP ($z \sim 0$) for one field period. Included are contour lines for $L_c = 100\,\mathrm{m}$, $L_c = 1330\,\mathrm{m}$, the PARVMEC LCFS and a flux surface at $\rho_\theta = 0.87$.

$$\begin{cases} \chi_{\mathrm{BMW}} = \oint_{\partial S} \vec{A} d\vec{l} \sim 2\pi R A_\phi & (4.13) \\ \rho_{\theta,\mathrm{BMW}} = \sqrt{\dfrac{\chi_{\mathrm{BMW}} - \chi_{\mathrm{axis}}}{\chi_{\mathrm{sep}} - \chi_{\mathrm{axis}}}} & (4.14) \end{cases}$$

[2]The length along a field line between the point it is started from and its intersection with a wall structure.

where χ_{sep} and χ_{axis} are taken to be the interpolated poloidal flux values evaluated at the separatrix and magnetic axis of the underlying PARVMEC solution. The presence of islands becomes apparent for all rational flux surfaces with $\{m, n = 2\}$ topology as can be seen in **figure 4.12**. Further islands can also be discerned, such as the $\{m = 7, n = 4\}$, $\{m = 9, n = 4\}$, etc. The position of the rational flux surfaces from PARVMEC has been included as red vertical lines, denoted by their rational number. The shift between the actual island and the PARVMEC rational flux surface position is expected, due to the implicit ι-jump that is produced for a given resolution in order to preserve nestedness [96] and the approximation in **equations 4.13** and **4.14**. Despite the appearance of numerical islands in the equilibrium core, we will see in the next sections that this does not influence our intended study, which happens mostly in the SOL.

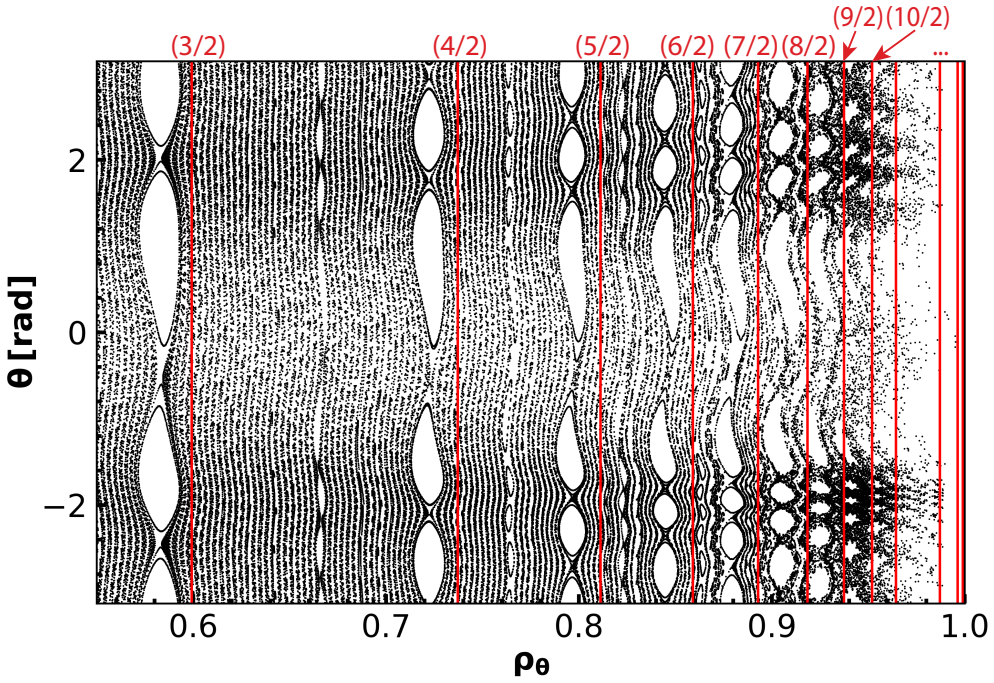

Figure 4.12: Poincaré plot of BMW induction field at the $\phi = 0$ poloidal cross-section mapped to the $\{\rho_\theta, \theta\}$ plane. In red, position of rational flux surfaces in the PARVMEC solution.

4.3 EMC3-EIRENE kinetic profile reconstruction

The EMC3-EIRENE transport calculations can be summarized in two steps. One of technical nature and the second of more physical relevance. The first one is the construction of a computational mesh given that the BMW solution contains closed flux surfaces, islands and stochastic regions. The second one is the appropriate choice of perpendicular transport coefficients for particle (D), electron heat (χ_e) and ion heat (χ_i) fluxes appearing in **equations 2.49**. We give a description of both steps in what follows.

4.3.1 Grid geometry

In this step, a 3D grid is constructed taking as a reference the PARVMEC&BMW magnetic induction field solution described in the previous section. First, a 2D grid is built in each toroidal

plane. This grid is usually meant to be aligned with the separatrix as best as possible, in order to provide sufficient radial resolution in the pedestal region. In our field solution, islands overlap at the very edge, making this step not trivial. The inner boundary of the simulation domain is made to align with a non-rational flux surface, which provides a closed surface avoiding particle losses. Afterwards, magnetic field lines are followed from the nodes of each 2D grid until the next one, thus building the final 3D grid. Flux tubes from which field lines can be bi-linearly interpolated at runtime are constructed in this step. This procedure saves significant computational resources, avoiding a *real-time* field line tracing for each Monte Carlo particle.

A simulation with no sources and no fluxes through the boundary surfaces is performed to check the quality of the grid, the so-called Monte Carlo test. If everything is performed correctly, a uniform particle probability density is expected. Furthermore, flux conservation within each grid generated flux tube is checked to further diagnose the quality of the grid. The 2D grid geometry with an overlaid Poincaré plot, as well as the result from the Monte Carlo test and flux conservation diagnostic can be seen in **figure 4.13**. The probability distribution function displays random fluctuations with an average value of $\langle f_{\text{density}} \rangle = 1.01 \pm 0.07$, where the error represents 3σ. The fact that no particular geometric feature can be associated with such fluctuations is another proof of the good divergence-free nature of the magnetic field. Likewise, deviations to flux conservation amount only to $\max(\delta_{\text{flux}}) \sim 0.3\%$, in good agreement with previous studies of EMC3-EIRENE grid formation from a PARVMEC&BMWC equilibrium in the W7-X stellarator [98][3]. Given the good quality of the grid diagnostics, we proceed to use it in the calculation of plasma kinetic profiles.

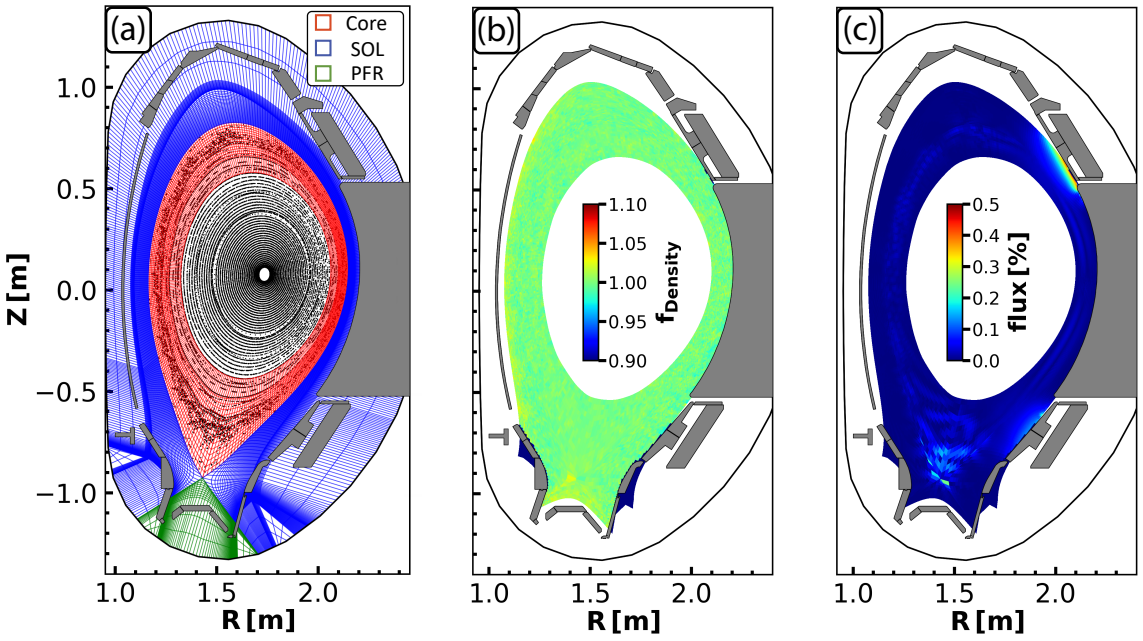

Figure 4.13: (a) EMC3EIRENE 2D grid and Poncaré plot of the PARVMEC&BMW field solution. (b) Monte Carlo test. Particle probability distribution function. (c) Percentage of magnetic flux deviation within flux tubes. All poloidal cross-sections are taken at $\phi \sim 0°$.

[3]Note that in [98] it was found that if EXTENDER was used, $\max(\delta_{\text{flux}}) \sim 3\%$, and MFBE resulted in $\max(\delta_{\text{flux}}) \sim 10\%$.

4.3.2 Selection of transport coefficients

An optimum set of transport coefficients is that which best reproduces the experimental results. To verify the agreement, a synthetic lithium beam diagnostic has been used in the EMC3-EIRENE solution domain. Scalar quantities, i.e. n_e, are mapped to the synthetic LOS and compared against those measured in experiments (see **figure 3.14**). Usually, it is desirable to use more than one synthetic diagnostic, for instance, thermionic divertor currents, ECE emission for T_e profile, etc. can be included. In this case, only the synthetic lithium beam was implemented, and additional ones will be left as future work. In order to quantify the degree of agreement between the synthetic diagnostic and the experimental data, we define the following metric:

$$\begin{cases} \delta_{\text{min/max}} = \left| \sqrt{\frac{1}{N} \sum_i \left(n_e^{\text{EMC3}}(x_i, \phi) - n_e^{\text{exp}}(x_i, \phi) \right)^2} \right| & (4.15) \\ \delta_{\text{tot}} = \frac{\delta_{\text{min}} + \delta_{\text{max}}}{2} & (4.16) \end{cases}$$

which shall be minimized. Here $\delta_{\text{min/max}}$ is the metric at $\phi = \phi_{\text{min/max}}$, i.e., where the kink displacement in the LOS is minimum / maximum and x_i are the lithium beam channel positions in the LOS, such that $10^{16}\,\text{m}^{-3} < n_e^{\text{exp}} < 2.5 \times 10^{19}\,\text{m}^{-3}$. This density range is chosen because it covers completely the density region used in the simulation domain of RAPLICASOL, as it will be further described in the next section.

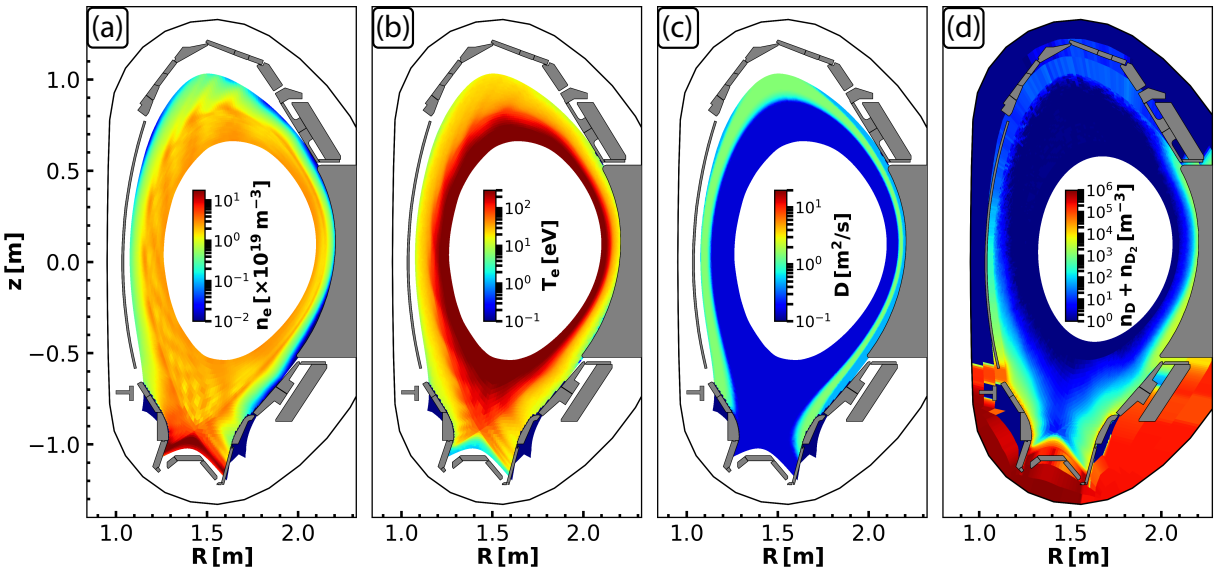

Figure 4.14: (a) n_e, (b) T_e, (c) $D_\perp$ and (d) Atomic, n_D, and molecular, n_{D_2}, neutral deuterium density poloidal cross-sections. The quantities are evaluated at $\phi \sim 0$.

The reconstruction of kinetic profiles was performed as follows: A 1D cross-field particle diffusion coefficient profile, $D_\perp$, was chosen as a function of ρ_θ. This profile includes a reduced transport region inside the LCFS, which is representative of the core high-confinement properties, a linear increase in the near SOL, where particles are no longer well confined, and a constant layer for the far SOL. This 1D $D_\perp$ profile is then mapped to the 3D grid by using the ρ_θ coordinate from BMW (**equation 4.14**). After testing different $D_\perp$ profiles, it turned out that a

step in the far SOL needed to be introduced. The lithium beam sits toroidally close to the limiter of ICRH3 (see **figure 2.1**), which likely affects the density profile in the far SOL. However, in EMC3-EIRENE, even though realistic limiters are included into the simulation, these are fixed with respect to the MP field rotation phase, i.e., we are simulating a single time point (and then we will just rotate the resulting electron density) instead of performing a new simulation for each MP rotation phase. Therefore, the modeled electron density is not affected at the maximum and minimum LOS kink displacements by the ICRH3 limiter, unlike the lithium beam diagnostic is in the experiment. This is, however, not of great importance since we set a vacuum layer in RAPLICASOL for densities lower than $2\times10^{17}\,\mathrm{m}^{-3} > n_e$ anyway. As a boundary condition, the electron density was set to $n_e = 2 \times 10^{19}\,\mathrm{m}^{-3}$ just inside the separatrix. The resulting n_e, T_e, $D_\perp$ and neutral particle deuterium density can be seen in **figure 4.14** for a poloidal cross-section at $\phi \sim 0$. It is readily noticeable that the density and temperature profiles are 3D perturbed. In particular, the characteristic lobes from the application of MPs can be more clearly seen in the X-Point region of the temperature profile. The comparison between the modeled and experimental electron density can be seen in **figure 4.15**. The resulting metric for this case is $\delta_{\mathrm{tot}} \sim 2.1 \times 10^{18}\,\mathrm{m}^{-3}$. The EMC3-EIRENE n_e profile is taken at the lithium beam LOS for ϕ_{min} and ϕ_{max} and compared against the experimental profiles for minimum and maximum approach reconstructed as described in the previous chapter. Very good agreement is attained for $10^{18}\,\mathrm{m}^{-3} < n_e < 1.5\times10^{19}\,\mathrm{m}^{-3}$. The profile in the far SOL ($n_e < 10^{18}\,\mathrm{m}^{-3}$) decays slower than the measurements, due to the lack of the limiter effect. The profile inside the LCFS $n_e \gtrapprox 1.5 \times 10^{19}\,\mathrm{m}^{-3}$ flattens out rapidly, which points to the influence of the edge stochastic region in the PARVMEC&BMW solution. Overall the result is very successful, since:

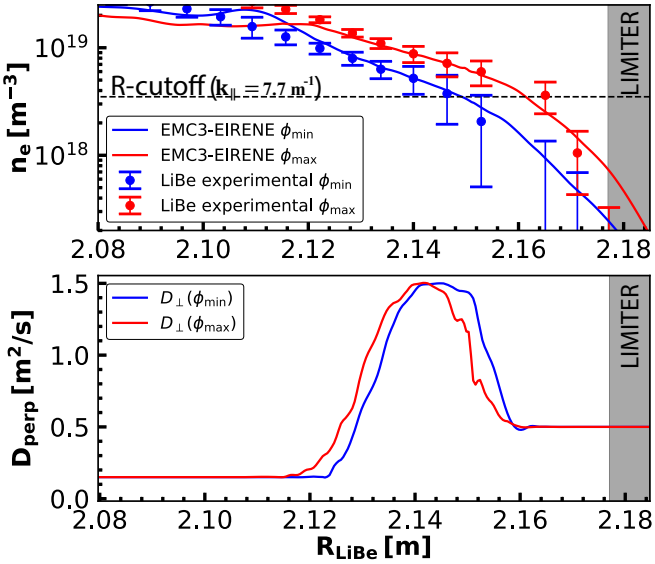

Figure 4.15: (Up) Synthetic lithium beam vs. experimental data. (Down) $D_\perp$ profile in lithium beam LOS.

1. An EMC3-EIRENE grid has been built from the PARVMEC&BMW induction field solution for a tokamak for the first time, that does not suffer from the violation of $\vec{\nabla}\cdot\vec{B} \neq 0$ across the LCFS.

2. The reconstructed kinetic profiles display the characteristic topology expected from the application of a 3D MP field. Furthermore, very good agreement is found when compared to the experimental lithium beam profiles for the discharge we intended to model.

3. The R-cutoff displacement of the fast wave matches very well that of the experiment, which validates the usage of this 3D profile for the forthcoming RAPLICASOL simulations.

4. The larger discrepancies beyond $n_e \gtrapprox 1.5 \times 10^{19}\,\mathrm{m}^{-3}$ play a small role in the ICRF coupling simulations, which are mainly sensitive to the cutoff region (for the 2-strap antenna dipole $k_\parallel$ spectrum, $n_e^{\mathrm{cutoff}} \sim 3.5 \times 10^{18}\,\mathrm{m}^{-3}$).

4.4 3D RAPLICASOL ICRF coupling simulations

In this section, we perform RAPLICASOL ICRF coupling simulations for the 2-strap antenna with the computed EMC3-EIRENE 3D density profile. The magnetic induction field is still treated in 1D approximation, due to performance limitations in the PMLs with 3D magnetic fields[4]. We perform a set of 7 simulations by toroidally rigidly rotating the density profile. The toroidal center of the ICRF antenna was thus placed at $\phi = \{10°, 25°, 45°, 70°, 105°, 135°, 165°\}$. The intention is to reproduce the same coupling variations found in experiments when the MP field is rotated. In **figure 4.16**, we show the antenna center positions along the 3D density R-cutoff at the OMP, and the 1D radial n_e profiles taken at those same locations. A least squares fit to the R-cutoff position is performed, like previously done for the experimental time traces.

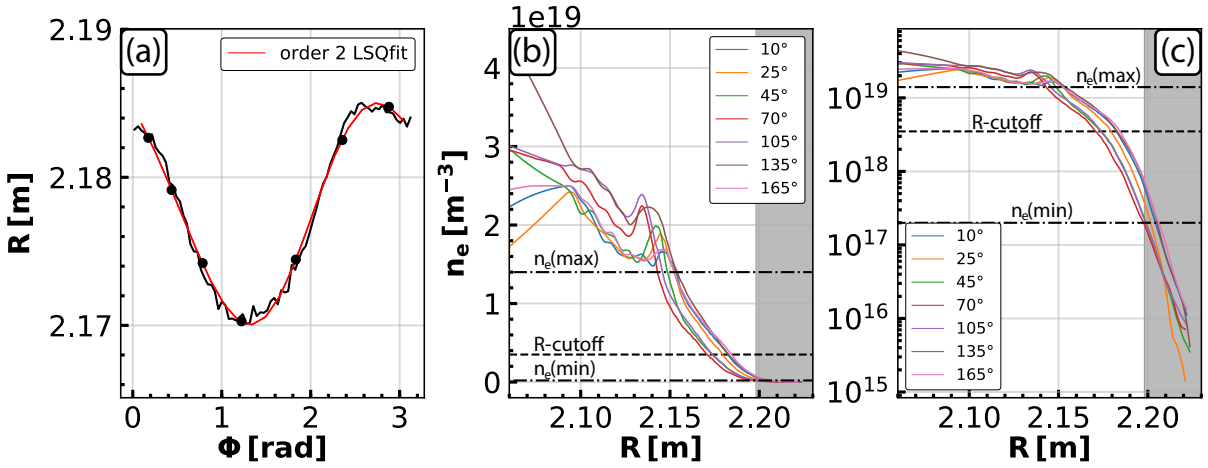

Figure 4.16: (a) Radial position of the R-cutoff as a function of the toroidal angle at the OMP for one field period. The antenna center for each simulation is denoted by a point. (b) 1D electron density profiles at the different toroidal slices indicated in (a) with $n_e^{\max}$ and $n_e^{\min}$. (c) Same as (b) in logarithmic y-axis.

The plasma domain in RAPLICASOL is comprised between $n_e^{\min} = 2 \times 10^{17}\,\mathrm{m}^{-3} \leq n_e \leq n_e^{\max} = 1.4 \times 10^{19}\,\mathrm{m}^{-3}$. Here, $n_e^{\min}$ is the minimum density value allowed, which prevents the appearance of the lower hybrid resonance. Any density below this value is assumed $n_e = n_e^{\min}$ up to the vacuum layer where the antenna is embedded. $n_e^{\max}$ is the maximum density allowed, which prevents gradients in the plasma-PML interface. Any density above this value is assumed $n_e = n_e^{\max}$. This value is somewhat smaller than that used in the 1D simulations of **section 3.2.6**, in order to avoid the artificial density-well inside the LCFS, which arises at the edge stochastic region. For these simulations, we use uniquely the curved antenna model. The RAPLICASOL antenna loading resistance is evaluated by applying the same least squares fit to the obtained per-port loading resistances, and then taking the average between both ports, as seen in **figure 4.17(a), (b)**. Its change is evaluated by the average of the per-port loading change, calculated as in experiments:

$$\left\langle \Delta R_L^{\mathrm{RAPLICASOL}} \right\rangle = \left\langle \frac{\langle R_L \rangle^{\mathrm{port_1}} + \Delta R_L^{\mathrm{port_1}}}{\langle R_L \rangle^{\mathrm{port_1}} - \Delta R_L^{\mathrm{port_1}}}, \frac{\langle R_L \rangle^{\mathrm{port_2}} + \Delta R_L^{\mathrm{port_2}}}{\langle R_L \rangle^{\mathrm{port_2}} - \Delta R_L^{\mathrm{port_2}}} \right\rangle \tag{4.17}$$

[4]When a 3D induction field was used, spots where EM energy was generated were observed within the PMLs. This is contrary to their expected behavior, as they should act as pure energy sinks.

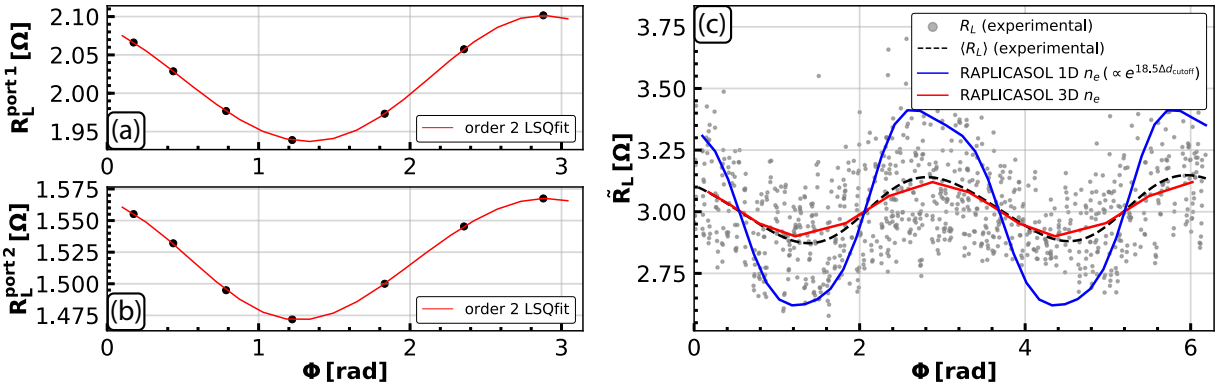

Figure 4.17: (a), (b) RAPLICASOL provided with the EMC3-EIRENE 3D n_e per-port loading resistance and least squares fit. (c) Experimental (ASDEX Upgrade #34622, $t = 2.15 - 4.45$ s) ICRH3 average loading resistance vs. that computed with RAPLICASOL using 1D and 3D density profiles.

where $\langle R_L \rangle$ is the average loading resistance of the 7 simulations, and ΔR_L is the $n = 2$ amplitude of the least squares fit. Their average is compared to the RAPLICASOL simulations using the lithium beam 1D density profiles (here assumed to behave as $\alpha \sim 18.5\,\mathrm{m}^{-1}$) and the experimental loading resistance time traces for the modeled discharge, #34622 at $t = 2.15 - 4.45$ s in **figure 4.17(c)**. Since the EMC3-EIRENE 3D density reconstruction is validated against the lithium beam diagnostic, only the 2-strap antenna toroidally closest to it (ICRH3, $\sim 16°$ apart, see **figure 2.1(a)**) is displayed. The second 2-strap antenna, ICRH1, is $\sim 164°$ apart from the lithium beam, making the reconstructed density less accurate in that region, because of toroidally localized plasma asymmetries. The time coordinate in experiments is mapped to the toroidal angle in the simulations via the formula:

$$\phi = \phi_{\mathrm{ICRH3}} - \frac{2\pi \nu_{\mathrm{MP}}}{n_{\mathrm{MP}}}(t - t_0) \tag{4.18}$$

where $\nu_{\mathrm{MP}} = 3\,\mathrm{Hz}$, $n_{\mathrm{MP}} = 2$ and $t_0 = 3.5\,\mathrm{s}$ is the time point used to read in the MP coil currents from the experiment, which defines the toroidal phase of the MP field and that of the density locked to it. Due to uncertainties in the absolute radial positions of the plasma and ICRF antenna, the loading resistance from RAPLICASOL has been multiplied by a factor:

$$\tilde{R}_L = \frac{\left\langle R_L^{\mathrm{experiment}} \right\rangle}{\left\langle R_L^{\mathrm{RAPLICASOL}} \right\rangle} R_L^{\mathrm{RAPLICASOL}} \tag{4.19}$$

to equalize the baselines. The experimental average is taken over the two feeders of ICRH3 and all the MP cycles. We observe that the average loading resistance is very well reproduced by the baseline-corrected RAPLICASOL simulations employing the EMC3-EIRENE 3D density profile, which was the objective of the study. RAPLICASOL simulations employing a 1D density profile, on the other hand, greatly overestimate this average.

Having obtained the $n = 2$ change of both the cutoff displacement and the loading resistance, we can now compare their relation to the experimental results of **section 3.2.5** and the simulations using a 1D density profile of **section 3.2.6**. A diagram is presented in **figure 4.18**. Scaling laws have been removed for clarity with the intent to only compare RAPLICASOL simulations with a 1D density profile, to the ones with the EMC3-EIRENE 3D density pro-

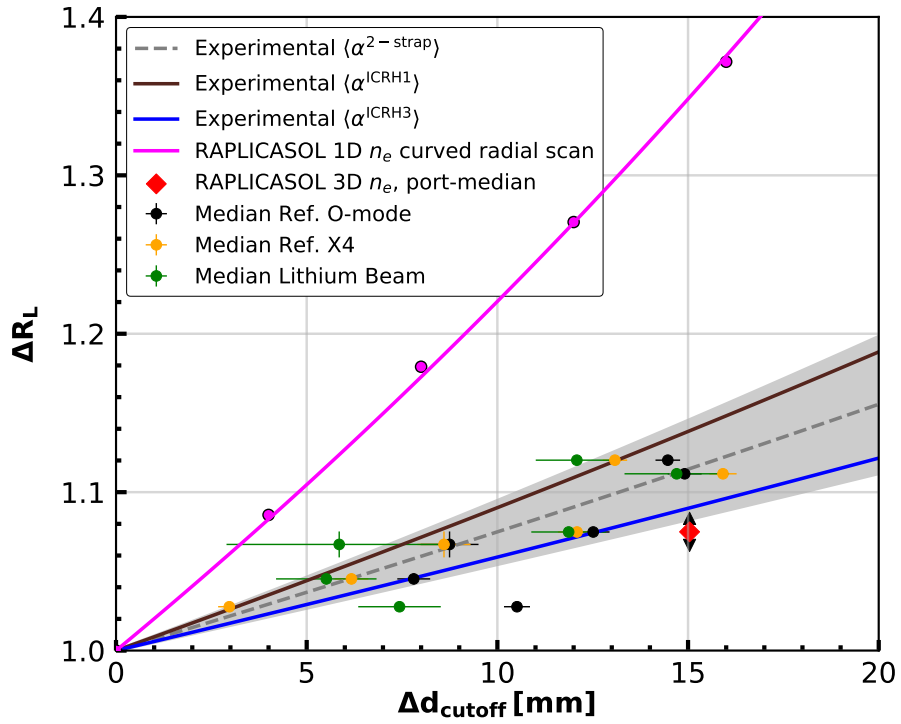

Figure 4.18: RAPLICASOL simulations using 1D (magenta line) and 3D (red diamond) density profiles. Included are the experimental scaling using ICRH1&ICRH3 data sets (dashed gray line), ICRH1 alone (brown line), ICRH3 alone (blue line) and the experimental median over all ICRH1 and ICRH3 feeders for every diagnostic (black, orange and green scatter).

Approach	$\alpha \pm 2.58\sqrt{\mathrm{Var}(\alpha)}$	Error w.r.t ICRH3
RAPLICASOL flat model radial scan 1D n_e	19.28 ± 2.02	236 %
RAPLICASOL flat model simulations 1D n_e	17.01 ± 6.89	197 %
RAPLICASOL curved model radial scan 1D n_e	19.92 ± 0.35	248 %
RAPLICASOL curved model simulations 1D n_e	17.47 ± 4.31	205 %
RAPLICASOL curved model EMC3-EIRENE 3D n_e	**4.81 ± n/a**	**16 %**
Experimental ICRH3 data set	**5.73 ± 0.8**	n/a
Experimental ICRH1 data set	8.64 ± 1.33	n/a
Experimental ICRH1&ICRH3 combined data sets	7.22 ± 1.10	n/a

Table 4.1: Second column: α estimators in $[\mathrm{m}^{-1}]$ for experiments and RAPLICASOL simulations with 1D and 3D density profiles. Results using OLS with a 99% confidence interval. Third column: Relative error in α estimators between simulations and the ICRH3 experimental data set.

file. The experimental scaling is derived by using the average of the ODR α values for the combined ICRH1&ICRH3 data sets, resulting in $\langle\alpha^{2-\mathrm{strap}}\rangle = 7.22\,\mathrm{m}^{-1}$. We also include the resulting scaling when using the data from ICRH1 alone $\langle\alpha^{\mathrm{ICRH1}}\rangle = 8.64\,\mathrm{m}^{-1}$ and that of ICRH3 alone, $\langle\alpha^{\mathrm{ICRH3}}\rangle = 5.73\,\mathrm{m}^{-1}$. The difference, albeit small, between the ICRH1 and ICRH3 scalings highlights the importance of locally resolving the electron density in the antenna vicinity. We have also included an uncertainty region comprised between the smallest measured scaling $\alpha^{\mathrm{ODR}}(\mathrm{ICRH3}) = 5.30\,\mathrm{m}^{-1}$ using the R-cutoff obtained from O-mode reflectometry and the

largest $\alpha^{\mathrm{ODR}}(\mathrm{ICRH1}) = 9.04\,\mathrm{m}^{-1}$ obtained from the lithium beam, which covers both individual 2-strap antenna data sets together. The experimental median over all ICRH1 and ICRH3 feeders is included as a scatter, as a function of the R-cutoff displacement measured by lithium beam, O-mode and Ref. X4 reflectometry. It is readily verified that the RAPLICASOL prediction with a 3D density profile is more accurate than that previously obtained with 1D density profiles. This corroborates the impact of non-axisymmetric density on the loading resistance, which cannot be well predicted by the 1D simulations. The upper feeder of the computed RAPLICASOL loading resistance change with the 3D density profile falls within the uncertainty region, but the average value is just short. We list the OLS α regression coefficients for an exponential fit in **table 4.1**, which serve as a comparison metric between experiments and simulations. These also include the RAPLICASOL simulations using the flat antenna model with 1D density profiles. For the flat and curved model simulations $\Delta d_{\mathrm{cutoff}}$ corresponds to the R-cutoff displacements of the used 1D lithium beam density profiles (**figure 3.14**), while the radial scans use the 4 mm shift increments of the "0 max" profile. We also list the α exponent relative error between simulations and experiments, where the scaling of ICRH3 has been taken as the comparison point since the density reconstruction is most relevant for this antenna. When comparing the RAPLICASOL simulations using the EMC3-EIRENE 3D density profile against the ICRH3 data set, the relative error is reduced to a $\sim$ 16%. Comparing them with the combined data set of ICRH1&ICRH3 only raises the relative error slightly, up to $\sim$ 33%. On the other hand, RAPLICASOL simulations employing the measured 1D density profiles result in $\sim$ 197% – 248%.

4.5 Conclusions

We have performed 3D ICRF antenna coupling simulations based on the computational workflow presented in **figure 4.1**. This addresses (i) the calculation of an ideal, non-linear, free-boundary MHD equilibrium for the core region of ASDEX Upgrade under applied MPs with the PARVMEC code; (ii) the extension of the magnetic induction field domain to the SOL via a volume integral of the core plasma currents with the BMW code; (iii) the preparation of a computational grid for the EMC3-EIRENE code, which served to verify the optimum quality of the magnetic field calculation; (iv) the reconstruction of plasma kinetic profiles via comparison to experimental data and (v) the calculation of the loading resistance change as the EMC3-EIRENE 3D density profile is rigidly rotated with full-wave simulations using the RAPLICASOL code.

An initial converged 2D equilibrium from the CLISTE code was used as a starting point to prepare the 3D PARVMEC simulations. A sensitivity scan was performed, which allowed identifying the main numerical parameters to optimize. We obtained that the number of poloidal mode numbers, m_θ, and radial grid points, n_s, should be increased as much as possible to properly resolve the edge q-profile and the shielding Pfirsch-Schlüter currents at rational flux surfaces. Meanwhile, the number of toroidal mode numbers, n_ϕ, should not be abused, especially when they cannot be well represented at the plasma edge in simulations with elevated q-profile, like tokamak ones. The tolerance of the force residual, f_{tol}, was found to play a role only above a certain threshold, i.e. $f_{\mathrm{tol}} \sim 5 \times 10^{-14}$ for this case. With a solution based on a compromise between numerical resources and physics fidelity, the computed plasma displacements fell a factor $\sim$ 2.25 short with respect to those measured in experiments. The main reasons are: (i) uncertainties in the input profiles, (ii) lack of a pump-out effect in the 3D simulation, (iii) limited numerical resolution and (iv) limitations of the ideal MHD approximation. In order to overcome

this, the currents in the MP coils were multiplied by a factor $f_{\mathrm{MP}} = 2.25$ to match numerical and experimental displacements. Through the extension of the magnetic field domain to the SOL with the BMW code, we verify that the flux surfaces' displacements from the PARVMEC solution are preserved for domains with no rational flux surfaces. This allows to reproduce experimentally-relevant particle transport and reconstruct kinetic profiles. Plasma domains with rational flux surfaces, however, lead to magnetic islands due to the imperfect shielding arising from the limited numerical resolution in PARVMEC. This is especially critical at the plasma edge, where a high magnetic shear exists.
An EMC3-EIRENE grid could be constructed, which verified the good quality of the induction field solution in terms of $\vec{\nabla} \cdot \vec{B} = 0$. This grid is used to compute plasma kinetic profiles by adjusting the cross-field transport coefficients, $D_{\perp}$ in particular. The EMC3-EIRENE modeled electron density is compared against the measurements of the lithium beam diagnostic introduced in **Chapter 3**. Their agreement is evaluated through a metric, δ_{tot} used to determine the optimal choice of transport coefficients. A satisfactory 3D n_e profile could be reconstructed within the most relevant portion of the ICRF coupling region. The agreement impoverished close to the limiter region, where the lithium beam is affected by toroidally localized vessel structures that are not taken into account when one toroidally rotates a single EMC3-EIRENE simulation. Beyond $n_e \gtrapprox 1.5 \times 10^{19}\,\mathrm{m}^{-3}$, the results also depart from experiments, due to the stochastic edge in the magnetic field solution.
Full-wave simulations with the RAPLICASOL code have been performed using as input the EMC3-EIRENE 3D n_e profile. The curved 2-strap ICRF antenna model was exclusively used. The density profile was toroidally rotated in several increments, and the loading resistance change was related to the R-cutoff movement. The resulting scaling is in better agreement with experiments within the considered experimental uncertainty. Unlike simulations employing a 1D n_e profile, where an overestimation in the α factor of the order $\sim 197 - 248\%$ is present, simulations employing the 3D n_e reconstruction approximate the experimental results within a factor $\sim 16\%$.

Overall, given the challenging experimental conditions, (i.e., characterization of plasma displacements and ICRF coupling changes in 3D geometry, which prevents the usage of common tools that assume axisymmetry), and large numerical challenges, i.e., development of a state-of-the-art 3D workflow, the found agreement between experiments and simulations is remarkable. These results settle the necessity to treat 3D problems in a 3D art, as reduction to 1D results too crude to give predictive capabilities. The developed tools are benchmarked, modular and flexible. These can be adapted to different tokamaks and stellarators for the better optimization of future ICRF antennas.

Chapter 5

Conclusions and outlook

As a conclusion, we would like to offer precise answers to the questions formulated in the motivation, based on the obtained experimental and numerical results.

- *How are the radiation impedance and loading resistance of an ICRH antenna modified by non-axisymmetric plasma configurations?*

It has been experimentally verified, that the change in both quantities is linked to the 3D SOL electron density distribution. In the case of an applied external MP field, this is generated by the plasma response to it, which consists of a kink displacement and the pump-out effect. Furthermore, both RF quantities are modified with an expected exponential behavior. However, it has been first experimentally, and then numerically proved, that the factor needed in the exponential is smaller than that for radial movements of an axisymmetric plasma. This behavior is likely linked to the size ratio between the poloidal plasma perturbation and ICRF antenna extension in the ASDEX Upgrade tokamak.

- *Do 1D scaling laws and 1D analytically-derived formulas still hold under these conditions?*

No. It has been experimentally confirmed, that while these laws and analytically-derived formulas hold very well for axisymmetric plasma configurations, they fail to reproduce the loading resistance change measured in rigidly rotated 3D MP plasmas.

- *What is the expected impact on the RF properties of an antenna arising from the conjoint operation of ICRH and MPs in current and future machines?*

The impact on the RF properties of the antenna will be dictated by the SOL electron density change arising from the application of the given MP field. Two main physical phenomena are identified to be the relevant ones: (i) the pump-out effect, which increases the SOL electron density through enhanced radial core transport, and (ii) the kink displacement, arising from the plasma response to the applied MP field. In current machines, such as ASDEX Upgrade, the observed loading resistance changes range up to $\sim 25\%$, given its particular antenna to plasma perturbation size ratio, used $k_{\|}$ RF spectrum and induced magnitude of the kink displacement. In future machines, such as ITER, the first factor is expected to increase the loading resistance

changes, while the second will probably decrease them. A scaling-law is elaborated which predicts such loading changes as a function of the R-cutoff displacement for an ASDEX Upgrade-like situation.

- *Are 1D antenna codes able to capture the 3D physics, or are 3D simulation tools required in order to reproduce the experimental behavior?*

RF coupling simulations using 1D electron density profiles representative of the tokamak OMP, are not capable of describing the measured experimental loading resistance changes in rigidly rotated MP plasmas. A relative error in the α factor of the order of $\sim 197 - 248\%$ is observed based on RAPLICASOL full-wave simulations. These, on the other hand, accurately describe the loading resistance changes measured in axisymmetric plasma scenarios. Contrarily, describing the electron density in full 3D geometry, which has been accomplished through the usage of PARVMEC&BMW and EMC3-EIRENE, and using it in RAPLICASOL, results in a predicted loading resistance change and α factor that hold better against experiments. We find a relative error in the α factor of $\sim 16\%$ when compared against the measurements of ICRH3 and of $\sim 33\%$ when using the combined ICRH1&ICRH3 data set. These 3D simulations also offer an appropriate description of the impact of anisotropies on antenna performance. We can, therefore, conclude that the 3D numerical workflow, developed and presented in this thesis, is an essential tool in order to correctly describe the observed experimental behavior.

As an outlook, we would like to point out a few possible developments based on the work here presented:

1. It is desirable to use a different MHD code than PARVMEC in the future. While in this thesis it was chosen for its simplicity, fastness and reliability, the fact that numerical magnetic islands are present in the final induction field solution is not desired. Preferably, a resistive MHD code could be employed in order to obtain proper plasma relaxation at rational flux surfaces. This would also improve the EMC3-EIRENE kinetic profile reconstruction.

2. The small relative error of $\sim 16 - 33\%$ between 3D full-wave simulations and experiments demonstrates the high reliability of RAPLICASOL to describe RF coupling even in complex geometries. Future improvements to RAPLICASOL may include: (i) A further experimental verification of the geometric features of the used antenna model, (ii) the inclusion of realistic plasma species and neutrals collisions to describe the lower-hybrid resonance, instead of avoiding it by artificially setting a vacuum layer and a minimum density, (iii) the extension of the simulation domain to include a larger portion of the core region and (iv) the ability to use 3D induction fields.

3. It would be of interest to compare already existing ICRF coupling results based on 1D simulations for stellarators with those predicted by the here presented 3D workflow. This could aid in the better optimization of planned ICRF systems, such as the one for W7-X.

4. With the presented experimental results and numerical workflow, it is possible to study the effect of MPs on edge + core physics. A possibility could be to couple AORSA [99] or SCENIC [100] to use the 3D magnetic field and density solutions. This can be used to study the effect of MPs on ICRF generated fast ion populations and transport, in a much more self-consistent way than presently possible.

Bibliography

[1] H. Bethe and R. F. Bacher. “Stationary States of Nuclei”. In: *Reviews of Modern Physics* (1936), pp. 1–148.

[2] G. Audi, A. H. Wapstra, and C. Thibault. “The Ame2003 atomic mass evaluation - (II). Tables, graphs and references”. In: *Nuclear Physics A* **729**.1 (2003), pp. 337–676.

[3] N. Bohr. “Mechanism of Nuclear Fission”. In: *Phys. Rev.* **56** (1939).

[4] H.-S. Bosch and G. M. Hale. “Improved formulas for fusion cross-sections and thermal reactivities”. In: *Nuclear Fusion* **32**.4 (1992).

[5] K. Miyamoto. *Plasma Physics and Controlled Nuclear Fusion*. Heidelberg: Springer-Verlag Berlin, 2005.

[6] J. R. Johnson, T. D. Swindle, and P. G. Lucey. “Estimated solar wind-implanted helium-3 distribution on the Moon”. In: *Geophysical Research Letters* **26**.3 (1999), pp. 385–388.

[7] J. D. Lawson. “Some criteria for a power producing thermonuclear reactor”. In: *Proceedings of the Physical Society. Section B* **70**.1 (1957), pp. 6–10.

[8] J. Wesson. *Tokamaks*. 3rd. Oxford, UK: Clarendon Press, 2010.

[9] G. H. Miller, E. I. Moses, and C. R. Wuest. “The National Ignition Facility: Enabling fusion ignition for the 21st century”. In: *Nuclear Fusion* **44**.12 (2004).

[10] H. Zohm. *Magnetohydrodynamic Stability of Tokamaks*. 1st ed. Weinheim, Germany: WILEY-VCH Verlag GmbH & Co., 2015.

[11] P. Alexandroff and H. Hopf. *Topologie*. Springer-Verlag, 1974.

[12] L. Spitzer. *The stellarator concept*. Tech. rep. Princeton University, 1951, pp. 253–264.

[13] G. H. (H. Neilson. *Magnetic fusion energy : from experiments to power plants*. 2014.

[14] R. S. Cohen, L. Spitzer, and P. M. Routly. “The Electrical Conductivity of an Ionized Gas”. In: *Physical Review* **80**.2 (1950), pp. 230–238.

[15] R. S. Hemsworth et al. “Overview of the design of the ITER heating neutral beam injectors”. In: *New Journal of Physics* **19**.2 (2017), p. 025005.

[16] T. H. Stix. *Waves in Plasmas*. AIP, New York, 1992.

[17] M. Brambilla. *Kinetic theory of plasma waves*. Oxford, UK: Clarendon Press, 1998.

[18] A. Ram and A. Bers. “Coupling theory for ICRF heating of large tokamaks”. In: *Nuclear Fusion* **24**.6 (1984), pp. 679–695.

[19] O. Heaviside. *Electromagnetic theory, Vol. III*. The electrician, 1912.

[20] S. J. Orfanidis. *Electromagnetic Waves and Antennas*. Piscataway, NJ: Rutgers University, 2016.

[21] H. A. Haus and J. R. Melcher. *Electromagnetic fields and energy*. Prentice-Hall, 1989.

[22] I. Stepanov. "Ion Cyclotron Range of Frequencies (ICRF) Power Coupling and Plasma Density Profile". PhD thesis. Ghent University, 2015.

[23] E. Viezzer et al. "High-resolution charge exchange measurements at ASDEX Upgrade". In: *Review of Scientific Instruments* **83**.10 (2012), p. 103501.

[24] M. Willensdorfer et al. "Characterization of the Li-BES at ASDEX Upgrade". In: *Plasma Physics and Controlled Fusion* **56**.2 (2014), p. 025008.

[25] E. Mazzucato. "Microwave reflectometry for magnetically confined plasmas". In: *Review of Scientific Instruments* **69**.6 (1998), pp. 2201–2217.

[26] A. Silva et al. "Ultrafast broadband frequency modulation of a continuous wave reflectometry system to measure density profiles on ASDEX upgrade". In: *Review of Scientific Instruments* **67**.12 (1996), pp. 4138–4145.

[27] D. E. Aguiam et al. "Implementation of the new multichannel X-mode edge density profile reflectometer for the ICRF antenna on ASDEX Upgrade". In: *Review of Scientific Instruments* **87**.11 (2016), 11E722.

[28] D. E. Aguiam. "Implementation of a X-mode multichannel edge density profile reflectometer for the new ICRH antenna on ASDEX Upgrade". PhD thesis. Universidade de Lisboa, Ghent University, 2018.

[29] B. Kurzan and H. D. Murmann. "Edge and core Thomson scattering systems and their calibration on the ASDEX Upgrade tokamak". In: *Review of Scientific Instruments* **82**.10 (2011), pp. 1–7.

[30] R. Fischer et al. "Integrated Data Analysis of Profile Diagnostics at ASDEX Upgrade". In: *Fusion Science and Technology* **58**.2 (2010), pp. 675–684.

[31] E. Strumberger and E. Schwarz. *VACFIELD code: Computation of the Vacuum Magnetic Field and its First Derivatives for Various Coil Types*. Tech. rep. Max-Planck-Institut für Plasmaphysik, 2005.

[32] W. Köppendörfer, M. Blaumoser, and K. Ennen. "The ASDEX Upgrade toroidal field magnet and poloidal divertor field coil system adapted to reactor requirements". In: *Nuclear Engineering and Design* **3** (1986), pp. 265–272.

[33] S. P. Hirshman and H. K. Meier. "Optimized fourier representations for three-dimensional magnetic surfaces". In: *Physics of Fluids* **28**.5 (1985), pp. 1387–1391.

[34] S. K. Seal et al. "PARVMEC: An Efficient, Scalable Implementation of the Variational Moments Equilibrium Code". In: *Proceedings of the International Conference on Parallel Processing* **2016-Septe** (2016), pp. 618–627.

[35] S. P. Hirshman and J. C. Whitson. "Steepest-descent moment method for three-dimensional magnetohydrodynamic equilibria". In: *Physics of Fluids* **26**.12 (1983), p. 3553.

[36] M. D. Kruskal and R. M. Kulsrud. "Equilibrium of a Magnetically Confined Plasma in a Toroid". In: *Physics of Fluids* **1**.4 (1958), p. 265.

[37] A. Clebsch. "Über die Integration der hydrodynamischen Gleichungen." In: *Journal für die reine und angewandte Mathematik* **56** (1859), pp. 1–10.

[38] D. P. Stern. "Euler potentials of current-free fields expressed in spherical harmonics". In: **99** (1994), pp. 2443–2445.

[39] W. D. D'haeseleer et al. *Flux Coordinates and Magnetic Field Structure*. Springer-Verlag, 1991.

[40] S. P. Hirshman, W. I. van RIJ, and P. Merkel. "Three-dimensional free boundary calculations using a spectral Green's function method". In: *Computer Physics Communications* **43**.1 (1986), pp. 143–155.

[41] P. Merkel. “An Integral Equation Technique for the Exterior and Interior Neumann Problem in Toroidal Regions”. In: *Proc.5th Int. Workshop on Stellarators* **1** (1984), p. 387.

[42] E. Strumberger et al. “Numerical computation of magnetic fields of two- and three-dimensional equilibria with net toroidal current”. In: *Nuclear Fusion* **42**.7 (2002), pp. 827–832.

[43] M. Drevlak, D. Monticello, and A. Reiman. “PIES free boundary stellarator equilibria with improved initial conditions”. In: *Nuclear Fusion* **45**.7 (2005), pp. 731–740.

[44] V. D. Shafranov and L. E. Zakharov. “Use of the virtual-casing principle in calculating the containing magnetic field in toroidal plasma systems”. In: *Nuclear Fusion* **12**.5 (1972), pp. 599–601.

[45] S. A. Lazerson. “The virtual-casing principle for 3D toroidal systems”. In: *Plasma Physics and Controlled Fusion* **54**.12 (2012).

[46] J. Loizu et al. “Magnetic islands and singular currents at rational surfaces in three-dimensional magnetohydrodynamic equilibria”. In: *Physics of Plasmas* **22**.2 (2015), p. 022501.

[47] T. Lunt et al. “First EMC3-Eirene simulations of the impact of the edge magnetic perturbations at ASDEX Upgrade compared with the experiment”. In: *Nuclear Fusion* **52**.5 (2012), pp. 0–7.

[48] M. Willensdorfer et al. “Three dimensional boundary displacement due to stable ideal kink modes excited by external n = 2 magnetic perturbations”. In: *Nuclear Fusion* **57**.11 (2017), p. 116047.

[49] W. Suttrop et al. “Experimental conditions to suppress edge localised modes by magnetic perturbations in the ASDEX Upgrade tokamak”. In: *Nuclear Fusion* **58**.9 (2018), p. 096031.

[50] D. Brida et al. “Heat flux pattern in detached L-modes and ELM mitigated H-modes with rotating magnetic perturbations in ASDEX Upgrade”. In: *Nuclear Fusion* **57**.11 (2017), aa78b9.

[51] D. Brida et al. “Determination of the stochastic layer properties induced by magnetic perturbations via heat pulse experiments at ASDEX upgrade”. In: *Nuclear Materials and Energy* **12** (2017), pp. 831–837.

[52] K. H. Burrell et al. “ELM suppression in low edge collisionality H-mode discharges using n = 3 magnetic perturbations”. In: *Plasma Physics and Controlled Fusion* **47**.12B (2005), B37–B52.

[53] A. Kirk et al. “Magnetic perturbation experiments on MAST L- and H-mode plasmas using internal coils”. In: *Plasma Physics and Controlled Fusion* **53**.6 (2011), p. 065011.

[54] W. Suttrop et al. “In-vessel saddle coils for MHD control in ASDEX Upgrade”. In: *Fusion Engineering and Design* **84**.2-6 (2009), pp. 290–294.

[55] M. Rott et al. “Electro-magnetic modeling of the planned active in-vessel coils at ASDEX Upgrade”. In: *Fusion Engineering and Design* **84**.7-11 (2009), pp. 1653–1657.

[56] W. Suttrop et al. “Experimental studies of high-confinement mode plasma response to non- axisymmetric magnetic perturbations in ASDEX Upgrade”. In: *Plasma Physics and Controlled Fusion* **59**.1 (2017).

[57] Y. Feng et al. “3D edge modeling and island divertor physics”. In: *Contributions to Plasma Physics* **44**.1-3 (2004), pp. 57–69.

[58] H. G. Frerichs. “Three-dimensional plasma transport in open chaotic magnetic fields: a computational assessment for tokamak edge layers”. PhD thesis. Aachen University, 2010.

[59] D. Reiter, M. Baelmans, and P. Börner. “The eirene and B2-eirene codes”. In: *Fusion Science and Technology* **47**.2 (2005), pp. 172–186.

[60] François Orain. “Edge Localized Mode control by Resonant Magnetic Perturbations in tokamak plasmas”. PhD thesis. Université d’Aix-Marseille, 2014.

[61] J. Jacquot et al. “Sequential modelling of ICRF wave near RF fields and asymptotic RF sheaths description for AUG ICRF antennas”. In: *EPJ Web of Conferences* **157** (2017), p. 03020.

[62] L. Colas et al. “SOL RF physics modelling in Europe, in support of ICRF experiments”. In: *EPJ Web of Conferences* **157** (2017), p. 01001.

[63] W. Tierens et al. “Validation of the ICRF antenna coupling code RAPLICASOL against TOPICA and experiments”. In: *Nuclear Fusion* **59**.4 (2019), p. 046001.

[64] L. Colas et al. “Perfectly Matched Layers for time-harmonic transverse electric wave propagation in cylindrical and toroidal gyrotropic media”. In: *Journal of Computational Physics* **389** (2010), pp. 94–110.

[65] G. Suárez López et al. “Investigation of the coupling properties of the ion cyclotron fast wave under applied magnetic perturbations and MHD phenomena in ASDEX Upgrade”. In: *EPJ Web of Conferences* **157** (2017), p. 03051.

[66] G. Suárez López et al. “ICRF coupling in ASDEX upgrade magnetically perturbed 3D plasmas”. In: *Plasma Physics and Controlled Fusion* **61** (2019), p. 125019.

[67] F. Wagner et al. “Regime of Improved Confinement and High Beta in Neutral-Beam-Heated Divertor Discharges of the ASDEX Tokamak”. In: *Physical Review Letters* **49**.19 (1982), pp. 1408–1412.

[68] V. Igochine. *Active Control of Magneto-hydrodynamic Instabilities in Hot Plasmas*. Berlin Heidelberg: Springer-Verlag, 2015.

[69] V. Bobkov et al. “Influence of gas injection location and magnetic perturbations on ICRF antenna performance in ASDEX Upgrade”. In: *AIP Conference Proceedings* **1580**.2014 (2014), pp. 271–274.

[70] M. Willensdorfer et al. “Plasma response measurements of external magnetic perturbations using electron cyclotron emission and comparisons to 3D ideal MHD equilibrium”. In: *Plasma Physics and Controlled Fusion* **58**.11 (2016), p. 114004. arXiv: 1603.09150.

[71] M. W. Shafer et al. “Plasma response measurements of non-axisymmetric magnetic perturbations on DIII-D via soft x-ray imaging”. In: *Physics of Plasmas* **21**.12 (2014), p. 122518.

[72] C. J. Ham et al. “Modelling of three dimensional equilibrium and stability of MAST plasmas with magnetic perturbations using VMEC and COBRA”. In: *Physics of Plasmas* **21**.10 (2014), p. 102501.

[73] O. Sauter, C. Angioni, and Y. R. Lin-Liu. “Neoclassical conductivity and bootstrap current formulas for general axisymmetric equilibria and arbitrary collisionality regime”. In: *Physics of Plasmas* **6**.7 (1999), pp. 2834–2839.

[74] R. Hager and C. S. Chang. “Gyrokinetic neoclassical study of the bootstrap current in the tokamak edge pedestal with fully non-linear Coulomb collisions”. In: *Physics of Plasmas* **23**.4 (2016), p. 042503.

[75] R. M. McDermott et al. “Evaluation of impurity densities from charge exchange recombination spectroscopy measurements at ASDEX Upgrade”. In: *Plasma Physics and Controlled Fusion* **60**.9 (2018), p. 095007.

[76] D. Carralero et al. “A study on the density shoulder formation in the SOL of H-mode plasmas”. In: *Nuclear Materials and Energy* **12** (2017), pp. 1189–1193.

[77] P. J. McCarthy, P. Martin, and W. Schneider. *The CLISTE interpretive equilibrium code*. Tech. rep. Max-Planck-Institut für Plasmaphysik, Garching, 1999.

[78] V. Bobkov et al. “First results with 3-strap ICRF antennas in ASDEX Upgrade”. In: *Nuclear Fusion* **56**.8 (2016), p. 084001.

[79] V. Bobkov et al. “ICRF operation with improved antennas in ASDEX Upgrade with W wall”. In: *Nuclear Fusion* **53**.9 (2013), p. 93018.

[80] R. Bilato et al. “Influence of an evanescence layer in front of the antenna on the coupling efficiency of ion cyclotron waves”. In: *Nuclear Fusion* **45**.2 (2005), p. L5.

[81] F. Clairet et al. “ICRF coupling and edge density profile on Tore Supra”. In: *Plasma Physics and Controlled Fusion* **46**.10 (2004), pp. 1567–1580.

[82] P. Jacquet et al. “Maximization of ICRF power by SOL density tailoring with local gas injection”. In: *Nuclear Fusion* **56** (2016), p. 46001.

[83] D. Milanesio et al. “A multi-cavity approach for enhanced efficiency in TOPICA RF antenna code”. In: *Nuclear Fusion* **49**.11 (2009), p. 115019.

[84] V. V. Bobkov et al. “ICRF antenna coupling dependence on edge plasma conditions in ASDEX Upgrade”. In: *Nuclear Fusion* **46**.7 (2006), S469–S475.

[85] I. T. Chapman et al. “Three-dimensional distortions of the tokamak plasma boundary: boundary displacements in the presence of resonant magnetic perturbations”. In: *Nuclear Fusion* **54**.8 (2014), p. 083006.

[86] D. Milanesio and R. Maggiora. “ITER ICRF antenna analysis and optimization using the TOPICA code”. In: *Nuclear Fusion* **50** (2010), p. 025007.

[87] V. Bobkov et al. “Impact of ICRF on the scrape-off layer and on plasma wall interactions: From present experiments to fusion reactor”. In: *Nuclear Materials and Energy* **18** (2019), pp. 131–140.

[88] R. Budny et al. “Benchmarking ICRF full-wave solvers for ITER”. In: *Nuclear Fusion* **52**.2 (2012), p. 023023.

[89] G. Suárez López et al. “Edge ICRF simulations in 3D geometry: From MHD equilibrium to coupling determination”. In: *AIP Conference Proceedings*. Vol. 2254. September. 2020, p. 050006.

[90] G. Suárez López et al. “Validation of high-fidelity ion cyclotron range of frequencies antenna coupling simulations in full 3D geometry against experiments in the ASDEX Upgrade tokamak”. In: *Plasma Physics and Controlled Fusion* **62**.12 (2020), p. 125021.

[91] M. Cianciosa et al. “3D Equilibrium Reconstruction with Islands”. In: *Plasma Phys. Control. Fusion* **60** (2018), pp. 1528–1531.

[92] A. Wingen et al. “Connection between plasma response and resonant magnetic perturbation (RMP) edge localized mode (ELM) suppression in DIII-D”. In: *Plasma Physics and Controlled Fusion* **57**.10 (2015), p. 104006.

[93] A. H. Boozer. “Physics of magnetically confined plasmas”. In: *Reviews of Modern Physics* **76**.4 (2004), pp. 1071–1141.

[94] P. Helander. “Theory of plasma confinement in non-axisymmetric magnetic fields”. In: *Reports on Progress in Physics* **77**.8 (2014), p. 087001.

[95] A. H. Boozer. “Plasma equilibrium with rational magnetic surfaces”. In: *Physics of Fluids* **24**.11 (1981), pp. 1999–2003.

[96] S. A. Lazerson et al. “Verification of the ideal magnetohydrodynamic response at rational surfaces in the VMEC code”. In: *Physics of Plasmas* **23**.1 (2016), p. 012507.

[97] M. Mikhailov, J. Nührenberg, and R. Zille. "Elimination of current sheets at resonances in three-dimensional toroidal ideal-magnetohydrodynamic equilibria". In: *Nuclear Fusion* **59**.6 (2019), p. 066002.

[98] J. D. Lore et al. "Modeling and Preparation for Experimental Testing of Heat Fluxes on W7-X Divertor Scraper Elements". In: *IEEE Transactions on Plasma Science* **46**.5 (2017), pp. 1387–1392.

[99] N. Bertelli et al. "Full wave simulations of fast wave efficiency and power losses in the scrape-off layer of tokamak plasmas in mid/high harmonic and minority heating regimes". In: *Nuclear Fusion* **56**.1 (2016).

[100] W. A. Cooper, M. Jucker, and J. P. Graves. "Self-consistent simulations of ICRH with the background equilibrium in tokamaks and stellarators". In: *Fusion Science and Technology* **65**.1 (2014), pp. 154–157.

Danksagung

Primero, y sobre todo, quiero darles las gracias a mis padres, Cristina y Guillermo, por su amor incondicional y apoyo inquebrantable.

I would also like to thank my Ph.D. thesis advisor, Prof. Dr. Hartmut Zohm, for his guidance, know-how, patience and support. Not only have I enjoyed fruitful physics discussions with him. He has also known how to wisely mold my ideas in the right direction at each stage of this work.

I would like to thank my IPP Garching colleagues who contributed most to this work. Especially, Dr. Matthias Willensdorfer and Dr. Erika Strumberger, who have inadvertently exercised the role of Ph.D. supervisors, and from whom I have learned the most. They offered their extensive expertise in experimental plasma physics, MHD theory and modeling, as well as their time and willingness. Among many other supporting actions, I was able to adapt the PARVMEC code to ASDEX Upgrade equilibria by leaning on their previous work. Dr. Tilmann Lunt, who spent a worth-while amount of time setting up the EMC3-EIRENE transport simulations. He built from my PARVMEC&BMW results a suitable computational grid, which I used to reconstruct the density profiles reported in Chapter 4. Dr. Wouter Tierens, with whom I have worked in close collaboration in several matters during the past years. He devised the ICRF 2-strap curved antenna model, which received many experimentally-based corrections from my obtained results. Furthermore, he also set up the RAPLICASOL simulations that have been reported in this thesis. In addition, I want to emphasize the received support from the ICRF department, in particular, Dr. Volodymyr Bobkov and Dr. Roman Ochoukov, who looked after the correct setup of the ICRF antennas. Likewise, the ICRF engineering team, who daily performed an excellent work in maintaining and improving the ICRF installations. Finally, I would like to thank the whole ASDEX Upgrade team, whether permanently located in Garching or otherwise, experimental session leaders, and diagnosticians, for configuring and assisting with the plasma scenario and data acquisition/interpretation.

I would also like to acknowledge the contribution from many other scientists, among many institutions, who to some degree devoted effort to this work. Dr. Joachim Geiger and Dr. Michael Drevlak from IPP Greifswald, who put me in contact with the PARVMEC team and performed the EXTENDER simulations shown in Chapter 2. Dr. Mark Cianciosa and Dr. Sudip K. Seal, from Oak Ridge National Laboratory, current developers of BMW and PARVMEC, who assisted me in running these two codes. Prof. Dr. Stéphane Heuraux, from Lorraine University, with whom I had many interesting conversations about ICRF coupling and near fields. Prof. Dr. Jean-Marie Noterdaeme, from Ghent University-IPP Garching, now enjoying a well-deserved retirement, who first offered me the Ph.D. position in the ICRF department, and with whom I had many interesting discussions. Dr. Valentin Igochine, from IPP Garching, with whom I had

many enriching conversations regarding ideal and resistive MHD physics. Dr. Severin Denk, formerly IPP Garching, now MIT, for sometimes fun, other times fundamental discussions over uncountable lunch breaks, and assistance with the German version of the abstract. And, Ana Kostic, for wise life advice every time I needed it.

Finally, I would like to thank both, the HEPP graduate school particularly, and the whole Max Planck Institute for Plasmaphysics in general, for greatly contributing to my scientific and personal growth.